



disdrodb: an open-source Python package for standardized processing, sharing, and analysis of disdrometer data

Gionata Ghiggi¹, Kim Candolfi¹, Anne-Claire Billaux-Roux², Régis Longchamps³, Son Pham-Ba³, Charlotte Weil³, and Alexis Berne¹

¹Environmental Remote Sensing Laboratory, École Polytechnique Fédérale de Lausanne, Lausanne, Switzerland

²Federal Office of Meteorology and Climatology MeteoSwiss, Payerne, Switzerland

³ENAC-IT4R, École Polytechnique Fédérale de Lausanne, Lausanne, Switzerland

Correspondence: Alexis Berne (alexis.berne@epfl.ch)

Abstract.

Disdrometers are specialized sensors designed to measure key properties of falling hydrometeors. Their observations are essential for characterizing precipitation particle size distributions (PSDs) and support a wide range of applications, including precipitation microphysics research, the development and evaluation of remote-sensing precipitation retrievals, and the modelling of microwave signal propagation through the atmosphere for telecommunication systems. However, the broader use of disdrometer data is hindered by limited access to existing datasets, heterogeneous raw data formats, and the lack of standardized, reproducible processing workflows.

This article presents the DISDRODB infrastructure and the associated open-source Python package `disdrodb`, a community framework for standardized sharing, processing, and analysis of disdrometer data. DISDRODB combines a centralized metadata archive with a decentralized data-sharing model, allowing institutions to retain control of raw data while making their datasets globally discoverable and straightforward for users to access and download through a common interface. The `disdrodb` software converts heterogeneous raw measurements into analysis-ready products through a modular three-level pipeline: L0 for standardized ingestion and formatting into `netCDF4`, L1 for temporal resampling, quality control, and hydrometeor/precipitation-type classification, and L2 for derivation of PSD integral parameters, parametric PSD model fitting, and simulation of polarimetric radar variables at multiple frequencies.

The framework provides a transparent, configurable, and reproducible open-source workflow for disdrometer data processing, with scalable execution from local environments to distributed computing systems. It also supports automatic generation of summary diagnostics for scientific analysis and is built on a modular, flexible architecture designed for community-driven extensions.

DISDRODB lowers barriers to both data access and analysis by enabling straightforward discovery and download of disdrometer datasets alongside reproducible processing workflows, thereby supporting large-sample studies of PSD variability, improved disdrometer intercomparison, and broader use of disdrometer observations in atmospheric science and remote sensing.



1 Introduction

25 Precipitation is intermittent and highly variable in space and time. It occurs in many forms, with different amounts, phases, and hydrometeor types. The phase of precipitation – whether it falls as rain, hail, snow, or mixed – has far-reaching natural and societal implications: it governs seasonal water availability through its influence on snowpack accumulation and melt (Mankin et al., 2015; Berghuijs et al., 2014; Harpold et al., 2017; Han et al., 2024), affects soil moisture and ecosystem dynamics (Trujillo et al., 2012; Harpold and Molotch, 2015; Rixen et al., 2022; Choler et al., 2025), and modulates natural hazards such as flooding (McCabe et al., 2007; Berghuijs et al., 2016, 2019; Blöschl, 2022), icing, and avalanches (Schweizer et al., 2003, 2021). It also critically impacts human activities, including road, rail, and air transportation (Norrman et al., 2000; Gultepe et al., 2019). While the phase and type of precipitation can be monitored using ground networks of present weather sensors, catching-type precipitation gauges, commonly known as pluviometers or rain gauges, have historically been used to monitor precipitation amounts (Lanza and Vuerich, 2009; Strangeways, 2010; Kidd et al., 2017).

35 Commercial catching-type gauges are, however, not sensitive to light precipitation and must be equipped with heating devices to measure solid precipitation. Tipping bucket gauges report a measurement only after the bucket collects a given amount (typically 0.1 or 0.2 mm of water), depending on the sensor type. This means that a minute with precipitation rates below typically 6 or 12 mm h⁻¹ goes undetected or is reported with a delay only when the bucket gets filled. Evaporation within the bucket can further reduce the measured amount, especially during light or intermittent precipitation (Sevruk, 1974; Dunn et al., 2025). In some cases, the collected water may completely evaporate before the bucket tips, and the event may never be recorded. As a result, a 10-minute precipitation (drizzle) event with an average intensity below typically 0.6 or 1.2 mm h⁻¹ may remain unrecorded. Additionally, tipping bucket gauges exhibit mechanical limitations at high rainfall intensities and dynamic calibration of the instrument is therefore recommended (Marsalek, 1981; Humphrey et al., 1997; Lanza and Stagi, 2009; Shedekar et al., 2016; Segovia-Cardozo et al., 2021).

45 Weighing precipitation gauges are generally more sensitive than tipping-bucket gauges, have a larger collection area, require less maintenance, but are typically configured to report accumulated precipitation amounts every 5, 10 minutes, or at longer time intervals (Leeper et al., 2015; Saha et al., 2021). High-frequency measurements, such as 1-minute accumulations, require additional processing to filter out signal noise (Ross et al., 2020; Filipovic, 2025). Like other catching-type gauges, they do not provide information about the phase or hydrometeor type and are known to underestimate precipitation in the presence of strong wind (Pollock et al., 2018; Kochendorfer et al., 2017; Cauteruccio et al., 2024).

50 Disdrometers are non-catching instruments designed to measure the size and number of hydrometeors as they impact or pass through a sensing area (Joss and Waldvogel, 1967; Löffler-Mang and Joss, 2000). Some also measure particles' fall speeds, providing additional information useful to infer hydrometeor types and precipitation phase (Kathiravelu et al., 2016; Lanza et al., 2021). Disdrometers are capable of detecting very light precipitation, with a sensitivity threshold below 0.001 mm h⁻¹, and unlike catching-type gauges, they provide the complete precipitation particle size distribution (PSD).

The PSD describes the number concentration and size distributions of hydrometeors in a volume of air. The characterization of PSDs is crucial for improving and evaluating microphysical and radiative transfer parameterization schemes in numerical



weather prediction models (Seifert and Beheng, 2006; Morrison and Grabowski, 2007; Abel and Boutle, 2012; Yang et al., 2019; Dolan et al., 2023; Niquet et al., 2024), as well as for advancing understanding of microphysical precipitation processes (Morrison et al., 2020). PSD data also help constrain precipitation-driven land surface interactions, such as canopy interception (Levia et al., 2017) and soil erosion (Serio et al., 2019), and impacts on human-built infrastructure, e.g. the erosion of wind turbines (Bech et al., 2022).

PSD measurements are also essential for realistically modelling optical, infrared and microwave signals' propagation through the atmosphere, a critical requirement for both ground-based and spaceborne telecommunication systems and for atmospheric remote sensing applications (Hogg, 1968; Ulbrich and Atlas, 1985; Bradley et al., 2000; Uijlenhoet et al., 2011; ITU-R, 2025). PSD information enables accurate simulations of precipitation-induced signal attenuation, which can be exploited opportunistically for rainfall estimation using commercial microwave links and satellite downlink signals (Messer et al., 2006; Leijnse et al., 2007; Overeem et al., 2013; Giannetti et al., 2017; Uijlenhoet et al., 2018; Chwala and Kunstmann, 2019; Zhang et al., 2023; Nebuloni et al., 2025; Graf et al., 2025). Knowledge of the PSD also supports modelling hydrometeors' microwave emission and scattering, which shape the radiometric signatures measured by passive microwave radiometers (Bennartz and Petty, 2001; Kneifel et al., 2010; Eriksson et al., 2018). In addition, simulations of the reflectivity and polarimetric variables that weather and cloud radars would observe for a given PSD provide the foundations for developing and evaluating precipitation-retrieval algorithms, radar forward operators and data assimilation systems for both ground-based and spaceborne radar systems (Ryzhkov et al., 2011; Zeng et al., 2016; Wolfensberger and Berne, 2018; Fielding and Janisková, 2020; Kotsuki et al., 2023). Disdrometer measurements also contribute to radar calibration and validation activities (Frech et al., 2017; Chen et al., 2021; Steinert et al., 2021; Deng et al., 2025).

The spatial and temporal structure of the PSD, from local to global scales, is key to understanding precipitation variability. Although this remains an active area of research (Uijlenhoet et al., 2003; Tokay and Bashor, 2010; Jaffrain et al., 2011; Tapiador et al., 2010; Raupach and Berne, 2016b, a; Tokay et al., 2016, 2017; Dolan et al., 2018; King et al., 2025), progress is constrained by the limited spatial and temporal coverage of existing datasets, which hampers a comprehensive characterization of PSD behavior and its links to microphysical, dynamical, and thermodynamic processes (Kumjian and Ryzhkov, 2012; Dawson et al., 2015).

Historically, disdrometers were mainly deployed during short-term field campaigns to improve the understanding of precipitation processes and small-scale variability. With the advent of commercial instruments, their use has expanded to operational observation networks, where they serve as present weather sensors (Blahak et al., 2025) or as backup rain gauges (Petan et al., 2025). In recent years, national and international initiatives have fostered the creation of national disdrometer networks (Adirosi et al., 2023; Petan et al., 2025; Pickering et al., 2019; Blahak et al., 2025) and the installation of sensors at long-term atmospheric observatory sites (Mather and Voyles, 2013; Stevens et al., 2016; Tokay et al., 2016; Laj et al., 2024; Flynn et al., 2026). Several of these sites now provide multi-year datasets, in some cases extending up to a decade of continuous measurements with only minor interruptions.

However, the study and modelling of PSDs continue to encounter multifaceted challenges. The scarcity of easily-accessible public disdrometer datasets has limited research aimed at unraveling the complex nature of precipitation PSD (Gatlin et al.,



2015; Dolan et al., 2018; Duncan et al., 2019; Ignaccolo and Michele, 2022; King et al., 2025) and has caused remote sensing precipitation algorithms to rely on a priori assumptions about the functional form of the PSD. These assumptions limit the ability to represent the full range of plausible solutions and introduce bias in the precipitation retrievals (Liao and Meneghini, 2013; Duncan et al., 2019; Ladino-Rincon et al., 2025).

Equally daunting is the diversity of instruments, data formats and practices adopted by institutions during the deployment of sensors: each institution records a unique set of variables and stores data in disparate text or binary formats that bear little resemblance to each other. This diversity of instruments, data formats and data processing methods is a barrier to the sharing and management of PSD observations.

Large-scale sample studies therefore require substantial time and effort to locate, access, review, and harmonize heterogeneous datasets into a consistent format before starting the analysis. Moreover, although some open-source efforts exist (Hardin and Guy, 2014; Leinonen, 2014), the lack of widely adopted and consistently maintained software for standardized disdrometer data processing continues to limit research reproducibility and productivity, thereby constraining the number of large-scale studies. The capabilities and limitations of these instruments are not yet fully characterized either, partly due to the proprietary nature of manufacturers' internal processing algorithms and as a result of the continued scarcity of publicly available data.

With the DISDRODB infrastructure and the software described in this manuscript, we aim to address some of these challenges. The platform provides a unified framework for the systematic sharing, standardization, and processing of disdrometer data. It includes a metadata archive listing all available stations and supports a decentralized data infrastructure, allowing each institution to share their datasets through their preferred dissemination platform. The accompanying Python software enables users to easily access data from selected stations, automatically convert raw measurements into a common standardized format, apply consistent quality control and filtering procedures, compute PSD integral parameters, simulate radar observables and specific attenuation from PSDs, and create summary figures and tables for each station. This automated and customizable processing chain ensures unified and reproducible data handling from collection to public release.

DISDRODB promotes open, transparent, and community-based research practices. It allows scientists to focus on scientific analysis rather than on time-consuming tasks such as data discovery, wrangling, and processing. The resulting global database opens new opportunities for PSD research, advances in (ground-based and spaceborne) remote sensing retrievals, and improved characterization of disdrometer uncertainty and accuracy. The modular architecture of the `disdrodb` software presented in this manuscript enables users to extend the software with new quality-control procedures, filters, processing chains, products, use individual modules independently, and contribute improvements back directly to the community through the open-source framework.

The manuscript is organized as follows. Section 2 introduces the disdrometer measurement procedures, their characteristics, main limitations and sources of uncertainty. Its purpose is to provide readers with the essential background needed to correctly interpret and analyze disdrometer data. Section 3 presents the DISDRODB infrastructure, including the metadata archive, the decentralized data archive, the data contribution mechanism and the `disdrodb` software workflow used to generate the DISDRODB products. Sections 4, 5 and 6 describe in detail the Level 0 (L0), Level 1 (L1), and Level 2 (L2) software processing chains, respectively. The L0 chain converts raw data into a standardized `netCDF4` format (Unidata, 2025). The



L1 chain resamples data at the desired temporal resolution, performs quality control and identifies precipitation phase and hydrometeor types using the raw particle spectra. The L2 chain computes integral PSD parameters (Sect. 6.1), fits custom models to the observed PSDs (Sect. 6.2) and simulates radar variables at selected frequencies (Sect. 6.3). All mathematical definitions are provided in the Appendices A, B, C, D and E.

2 Disdrometer Measurements: Principles, Characteristics, and Uncertainties

Disdrometers are point instruments that measure the size and fall velocity of individual falling hydrometeors. They count particles impacting or traversing their sensing volume during a given measurement interval. The sensing volume must be large enough to detect a sufficient number of sparsely distributed large drops, yet small enough to minimize cases where multiple particles cross (or impact) the sensing volume simultaneously. Disdrometers can be classified according to their measurement principle as impact, optical, video, or radar (Lanza et al., 2021), with optical disdrometers accounting for the majority of deployments worldwide. The accuracy of their measurements depends on the instrument's physical design, sensing characteristics and underlying assumptions, as well as its installation setup, environmental conditions and external interferences, the magnitude of these effects varying by sensor type. Although advanced camera-based disdrometers can track several particles at once (Barthazy et al., 2004; Newman et al., 2009; Garrett et al., 2012; Testik and Rahman, 2016; Maahn et al., 2024; Shi et al., 2025), the instruments considered in this manuscript (see Table 1) cannot reliably separate overlapping signals, which leads to biased estimates of particle size and fall velocity. Detected particles are categorized into discrete size and fall velocity classes, forming a two-dimensional matrix commonly referred to as the disdrometer raw spectrum, which represents the fundamental measurement from which all estimated PSD quantities are derived. The software presented in this work currently supports the processing of impact and optical disdrometers. Its modular design, however, allows for future integration of additional instrument types. Table 1 summarizes the main characteristics of the currently supported sensors.

In the following subsections, we describe the operating principles of impact and optical disdrometers, highlighting the characteristics, limitations, and processing uncertainties associated with each type. This overview provides the essential background needed to correctly interpret and analyze disdrometer measurements and the outputs of the processing chain presented in this manuscript.



Table 1. Characteristics of the disdrometers supported by DISDRODB. L, W, D, and H denote the nominal length, width, diameter, and height of the sensing area, respectively. The symbol “–” indicates parameters that are not applicable, while “n/a” denotes information not available or not disclosed by the manufacturer.

Instrument		Disdrometer	Sensing Area and Volume			Sampling and Measurement						
Sensor name	Manufacturer	Technology	Dimensions [mm]	Area [cm ²]	Volume [cm ³]	Rate [kHz]	Period [μ s]	D _{min} [mm]	D _{max} [mm]	V _{min} [m s ⁻¹]	V _{max} [m s ⁻¹]	Spectrum shape (D,V)
LPM	Thies Clima	Optical extinction	L: 228, W: 20, H: 0.75	45.6	3.42	109	9.17	0.125	>8	0	>10	(22, 20)
PARSIVEL	OTT HydroMet	Optical extinction	L: 180, W: 30, H: 1	54	4.86	50	20	0.2495	>23	0	>19.2	(32, 32)
PARSIVEL2	OTT HydroMet	Optical extinction	L: 180, W: 30, H: 1	54	4.86	50	20	0.2495	>23	0	>19.2	(32, 32)
PWS100	Campbell	Optical scattering	L: 89, W: 45, H: 0.4	40	1.6	96	10.42	0	>25.6	0	>25.6	(34, 34)
SWS250	Biral	Optical scattering	L: –, W: –, H: –	65.04	400	n/a	n/a	0	>6.4	0	>20	(21, 16)
ODM470	Eigenbrodt	Optical extinction	L: 120, D: 22, H: 22	26.4	45.6	28	35	0	>21.72	–	–	(128, –)
RD80	Distromet Ltd.	Impact	D: 8	50	–	100	10	0.3	>5.145	–	–	(20, –)



2.1 Impact disdrometers

Impact disdrometers characterize the PSD by counting and measuring the force produced by the hydrometeors striking the sensor surface. Each particle impact causes a small displacement of the sensor cover, generating a mechanical vibration that is converted into an electrical signal. The signal is related to the particle's kinetic energy and used to estimate the particle size. The kinetic energy of a particle is directly related to its mass and fall velocity. Impact disdrometers, however, do not directly measure particle fall velocity.

For raindrops, assuming constant water density and a known mass-diameter relationship, the use of a terminal fall velocity model allows for a reliable estimate of particle size from the measured impact energy. In contrast, snow particles exhibit a wide range of shapes, densities, masses, and fall velocities, making their impact response highly variable and preventing a reliable estimation of particle size. Therefore, impact disdrometers such as the Joss-Waldvogel Disdrometer (hereafter referred to as RD80, Joss and Waldvogel (1967)) can only be reliably used to characterize the raindrop size distribution (DSD).

The RD-80 disdrometer detects raindrops within the 0.3–5.5 mm diameter range, with drops larger than 5.5 mm all counted in the largest size bin. This limitation arises because the variation in raindrop terminal fall velocity, and consequently in kinetic energy, becomes very small for drops larger than 5 mm (see Figure B1), reducing the instrument's ability to distinguish between large drop sizes.

At the lower end of the spectrum, undersampling of small drops has been reported particularly during heavy rainfall when multiple drops impact the sensor surface quasi-simultaneously (Tokay et al., 2003, 2005). This issue, known as the dead-time effect, occurs when the impact of a large drop causes the sensor cone to vibrate. During these vibrations, smaller raindrops arriving within the next few milliseconds cannot be recorded. As a result, only the largest drop is registered, leading to an undercount of smaller drops (Sauvageot and Lacaux, 1995; Uijlenhoet et al., 2002).

Over time, prolonged exposure to solar radiation and repeated contact with rain gradually reduce the elasticity of the sensor surface cover, further lowering sensitivity to small drops. Additionally, strong winds and acoustic noise can also alter or mask the impact signal of small raindrops.

Finally, the RD-80 relies on a fixed empirical relationship to convert the impact signal into drop size. Raindrops falling at sub-terminal or super-terminal velocities (Montero-Martínez et al., 2009) are therefore underestimated or overestimated in size, respectively. The resulting effects on inferred DSDs and associated power-law relationships are discussed in Leijnse and Uijlenhoet (2010). In addition, because terminal fall velocity increases with altitude as air density decreases, and this effect is not accounted for in the instrument's internal calibration, raindrop sizes tend to be increasingly overestimated at higher elevations.

2.2 Optical disdrometers

Optical disdrometers measure the light extinction or light scattering of hydrometeors falling through their sensing volume. The measurement principles vary depending on whether they are based on light scattering or extinction. Table 1 reports the characteristics of the optical disdrometers supported by disdrodb.



185 2.2.1 Extinction-Based Optical Disdrometers

Extinction-based optical disdrometers measure precipitation by detecting the reduction of light intensity caused by hydrometeors passing through a thin laser beam (Hauser et al., 1984; Salles et al., 1998; Löffler-Mang and Joss, 2000) or a homogeneously illuminated volume (Illingworth and Stevens, 1987; Grossklaus et al., 1998; Lempio et al., 2007). Examples of such instruments supported by `disdrodb` are the OTT PARSIVEL (1 and 2), Thies LPM, and Eigenbrodt ODM-470 sensors. In both configurations, a receiver, typically a photodiode, is located in front of the light source to measure the incoming light intensity.

When a particle falls through the beam, the receiver measures a temporary decrease in voltage. The amplitude of this signal reduction is proportional to the particle's horizontal cross-sectional area, while its duration, the particle's residence time ($t_{residence}$) within the sensing volume, is related to the particle fall velocity and vertical dimension.

The particle's horizontal size (p_{size}) is derived from the maximum signal reduction and corresponds to the particle's maximum horizontal dimension. For raindrops, assuming they fall with their axis of symmetry vertically aligned, p_{size} corresponds to the drop's major axis (A). Assuming a raindrop axis ratio a_r (see Appendix A), the drop minor axis (B) can be obtained as $B = Aa_r$. The fall velocity can then be estimated as $V = (H + B)/t_{residence}$, where H represents the thickness of the laser beam or illuminated volume (see Table 1).

For non-spherical particles such as snowflakes or ice crystals, the random orientation and irregular shape of the falling particles make it difficult to relate the measured horizontal size to their actual maximum and vertical dimensions (Battaglia et al., 2010). The complex structure of snowflakes, such as internal air pockets within crystals, and the different extinction properties of ice compared to liquid water, further increase the uncertainty of the particle size estimate.

2.2.2 Scattering-Based Optical Disdrometers

Scattering-based optical disdrometers measure precipitation by detecting the near-infrared light scattered by hydrometeors passing through one or multiple light beams. Light is scattered through a combination of reflection, refraction, and diffraction, with their relative contributions depending on the particle's shape, phase, and refractive index. These instruments record the amplitude and duration of the scattered light pulses generated by each hydrometeor as it crosses the sensing volume. Similar to extinction-based disdrometers, the signal duration provides an estimate of the particle's fall speed, while its size can be derived using two different approaches.

The Campbell PWS100 uses two forward-scatter receivers placed at 20° to the beam, one in a vertical plane and one in a horizontal plane. Since refraction is the dominant scattering mechanism for raindrops, the scattered light reaches the vertical receiver slightly before the horizontal one. This time delay represents the time it takes for a drop to fall a known fraction of its diameter and, when combined with the fall speed, allows the drop size to be determined (Ellis et al., 2006).

Other instruments, such as the Biral SWS-250, VPF-730, and VPF-750, employ two receivers mounted in the horizontal plane: a forward-scatter receiver at 45° and a backscatter receiver at 113° . In this case, the maximum amplitude peak in the signal recorded by the receivers is used to estimate the particle size, while the ratio between forward and backward scattered light provides information on the hydrometeor phase. While for raindrops refraction dominates scattering, for frozen precipi-



220 tation (e.g., ice pellets, hail, or snow), diffraction and reflection become more significant. Ice particles containing trapped air bubbles or opaque crystalline structures tend to produce stronger backscatter signals, enabling discrimination between liquid and solid precipitation.

2.2.3 Limitations of optical disdrometers

Disdrometer measurements are sensitive to both instrumental limitations and environmental factors. These issues directly affect the accuracy of the retrieved DSD and its integral parameters. Particles that do not fall completely within the sensing volume cause only partial extinction or scattering of the light beam. As a result, they appear smaller than their actual size but with an unrealistically high fall velocity. This phenomenon, known as edge effects in the scientific literature, primarily affects larger drops, which have a higher likelihood of crossing the sensing volume boundaries. The OTT PARSIVEL sensors remove marginal fallers from their measurements through the use of two additional photodiodes (Battaglia et al., 2010), whereas other optical disdrometers do not appear to filter out these particles.

230 Accurate measurement of large drops is also limited by their very low concentration, sparse spatial distribution and the small sensing area of the instrument, which lowers the probability of detecting them, a limitation commonly referred to as the sampling effect. In addition, disdrometers typically use wider size bins (about 1 mm) for particles larger than 5 mm, and this coarser binning reduces the precision of the reported particle size estimates, an issue known as the quantization effect.

235 Simultaneous passage of horizontally overlapping particles through the sensing volume can lead to the detection of a single hydrometeor with an overestimated diameter and an underestimated fall speed. Similarly, vertically overlapping particles increase the measured signal duration, resulting in an overestimation of residence time and an underestimated fall velocity. These coincidence effects become more likely as rainfall rate and the number of falling drops increase. Their magnitude depends on the sensor's sampling area, the vertical thickness of the beam, and the sampling frequency.

240 During intense rainfall, an overestimation of small particle counts may also occur when raindrops impact the instrument housing or sensor surface, fragment, and rebound into the sensing area. This artifact is known as the splashing effect (Pickering et al., 2019; Friedrich et al., 2013).

245 In the presence of strong horizontal wind, large raindrops can become canted and distorted (Testik and Pei, 2017; Bolek and Testik, 2022; Zheng et al., 2024), appearing narrower than their true size when passing through the sampling area of a disdrometer. This effect leads to a slight underestimation of the size and fall velocity of large drops (Friedrich et al., 2013; Lin et al., 2021). Strong horizontal winds can also modify particle trajectories. Small droplets, which are expected to deviate more than larger drops, may cross the sensing volume at an angle or even horizontally. This may increase their residence time, resulting in an underestimation of fall velocity, and a higher probability of edge effects.

250 Proper sensor exposure is essential to minimize the effects of turbulence and vertical wind on disdrometer measurements. The instrument should be installed in an open area, away from objects that disturb the normal airflow. As a general guideline, a structure affects the airflow upwind for a distance of about twice its height and downwind for a distance of about six times its height (WMO, 2024). Obstacles such as towers, walls, or nearby instruments can create complex aerodynamic interactions between the airflow, the instrument body, and the approaching hydrometeors. These effects may introduce vertical air motions



that modify particle trajectories and bias fall velocity measurements (Kim and Song, 2018; Capozzi et al., 2021). Turbulence also broadens the observed distribution of fall velocities (Testik and Bolek, 2023; Zheng et al., 2024).

Wind is widely recognized as the most significant source of measurement biases. When the wind blows parallel to the sensor, turbulence generated by the airflow around the instrument heads can create updrafts that alter drop trajectories and reduce their fall velocities (Chinchella et al., 2024, 2025). Particles that impact the sensor or are diverted away from the sampling area lead to a significant undercatch and an underestimation of rainfall rate. In contrast, when the wind flows perpendicular to the laser beam, the disturbances are limited, and the wind-induced bias is smaller, typically within 10 %. To mitigate these wind-related biases, future disdrometer designs should aim to include dynamic orientation mechanisms. The OCEANRAIN project has specifically addressed this challenge by equipping its ODM-470 sensors with a wind vane that automatically pivots the instrument, keeping the sampling area aligned perpendicular to the local wind direction (Klepp, 2015; Klepp et al., 2018). Similarly, Friedrich et al. (2013) modified Parsivel disdrometers by rotating and tilting the sampling area into the wind to avoid artifacts observed during heavy rainfall with strong winds.

Beyond aerodynamic and instrumental biases, disdrometer measurements are also affected by various environmental and operational noise sources. Occlusion of the lenses by spider webs, dew, raindrops, or snow can alter the measurements, as can direct sunlight entering the field of view of the receiver(s). Artificial signals generated during cleaning of the optics, as well as spurious detections from birds, insects, pollen, and other non-precipitation particles, may result in erroneous hydrometeor counts. In cold environments, snow or riming can block the transmitter or receiver lenses, leading to sensor downtime or poor data quality. Blowing snow represents an additional source of noise.

Accurate disdrometer measurements also depend on regular maintenance and periodic recalibration. However, the current lack of standardized calibration procedures contributes to measurement uncertainty both within and between different sensors. This challenge is being addressed through ongoing initiatives such as the INCIPIT project (Baire et al., 2022) as well as through European standardization efforts that define metrological requirements and calibration methods for non-catching precipitation sensors (CEN, 2025).

Another major source of inconsistency arises from the proprietary and often undocumented internal processing of the instruments. Although optical disdrometers use the same fundamental detection principles, differences in their physical design, geometry, and internal filtering algorithms lead to deviations in measured quantities. The absence of documentation for key internal processes – including the counting algorithm, the handling of marginal or coincident particles, and the filtering of unrealistic or non-precipitation signals – makes cross-sensor comparison delicate. Firmware changes over time introduce additional uncertainty, further limiting the consistency of long-term DSD monitoring.

The maximum rainfall rates a sensor can measure under extreme conditions are determined by its sampling rate (A/D conversion), its actual processing capacity (maximum number of particles per second), and the presence and size of any temporary buffer used to store particle signals. Unfortunately, manufacturers often do not fully disclose this information.

While the DISDRODB infrastructure and software presented in this study cannot eliminate the inherent instrumental limitations and measurement biases discussed above, it provides a foundation for advancing disdrometer development and DSD research. By offering direct access to previously unavailable data and standardizing all records into a unified, analysis-ready



format, the software enables consistent analysis and reproducible workflows. This, in turn, facilitates comparison across instruments, helps identify sensor-specific limitations, and supports large-sample studies of DSD variability.

3 DISDRODB infrastructure

290 The DISDRODB infrastructure includes a metadata archive, a decentralized data archive and the Python package `disdrodb`. The system deliberately decouples data discoverability and access, which are centrally managed through the metadata archive, from physical data storage, which remains decentralized and under the control of data providers. Figure 1 illustrates the core components, which are described in detail in the following subsections.

3.1 DISDRODB Metadata Data Archive

295 The metadata archive is hosted on GitHub and serves as a central platform for listing available stations. A station represents an individual disdrometer sensor deployed at a specific location. Each station is described by a metadata file containing standardized fields that specify the instrument details, geolocation, data reader, and the URL to the public data repository where the raw data are shared. Users can also report specific timestamps or periods when sensors malfunctioned – due to environmental interferences such as spider webs, birds, or icing – or produced erroneous records caused by, e.g., human intervention, using
300 dedicated issue files. The `disdrodb` software can automatically exclude these problematic time steps when generating DISDRODB products. GitHub enables community collaboration, allowing continuous improvement of metadata quality, reporting of data issues, and maintain a transparent, fully reproducible DISDRODB processing chain.

Institutions and contributors may upload station metadata even if the data are not yet publicly available due to policy constraints or embargoes. The DISDRODB metadata archive thus acts as a catalog of all past, present, and future disdrome-
305 ters, ensuring centralized long-term documentation and improved data findability. An interactive web map is available at <https://disdrodb.org> to explore the stations, with filtering options based on data availability, deployment status, time period, duration, sensor type, data source, campaign name, and station name.

3.2 DISDRODB Decentralized Data Archive

To encourage data sharing, we recognized the need for a contribution system that is both user-friendly and that preserves
310 contributor control and authorship. Therefore, DISDRODB follows a decentralized archive model, in which contributors store their data in their preferred online platform and reference these storage locations in the DISDRODB Metadata Archive. All raw data from a disdrometer station can be uploaded as a ZIP archive to data repositories such as Zenodo or Figshare. Alternatively, the use of institutional web or File Transfer Protocol (FTP) servers allows near-real-time data dissemination and user-side incremental updates of the DISDRODB data archive. In both cases, the URL of the ZIP archive or the server
315 directory, specified in each station metadata file within the DISDRODB Metadata Archive, enables the `disdrodb` software to automatically access and retrieve the requested data.

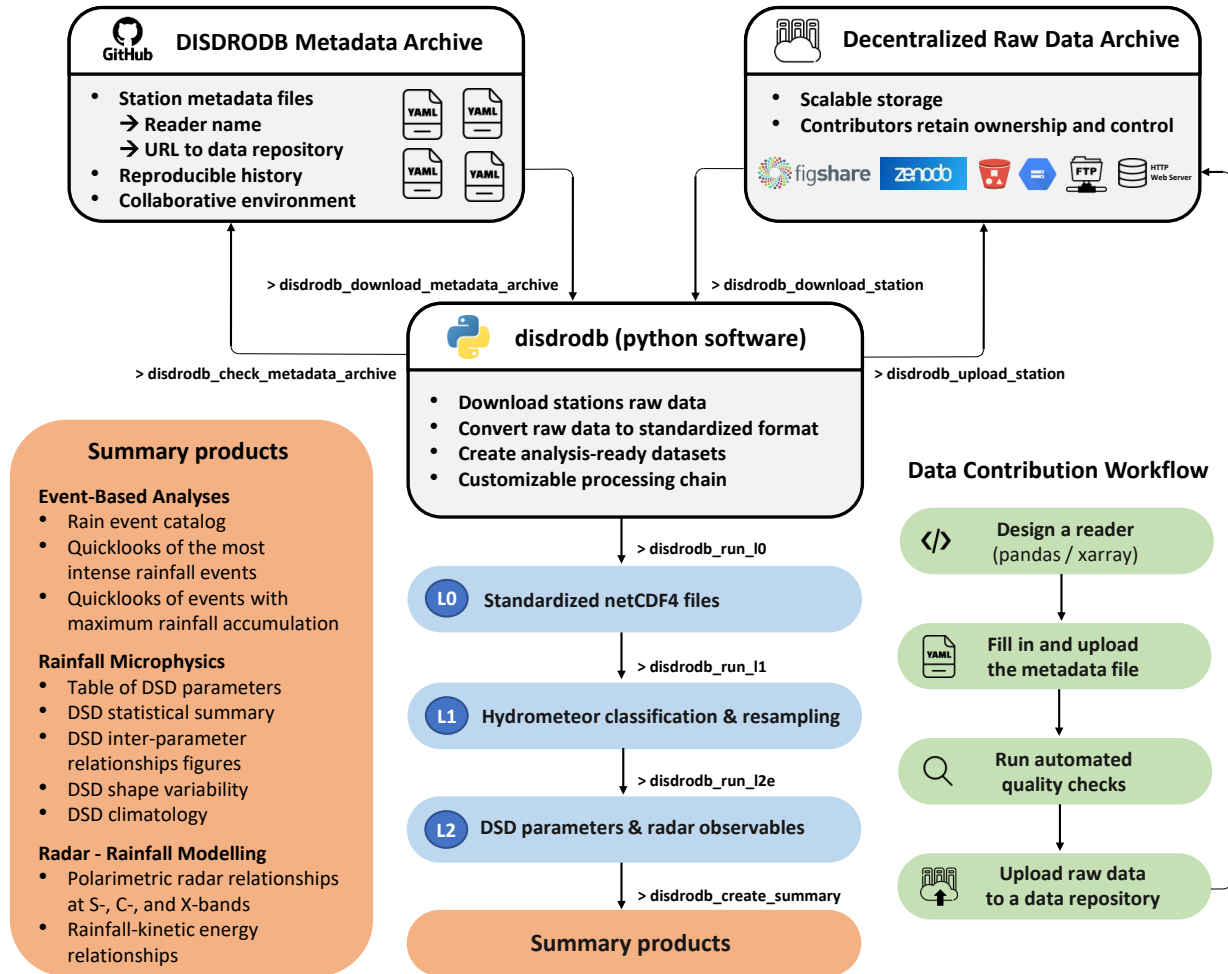


Figure 1. Schematic overview of the DISDRODB infrastructure and processing workflow. The `disdrodb` Python software interfaces with a centralized metadata archive and decentralized raw data repositories, enabling standardized data ingestion, automated quality control, and the generation of hierarchical, analysis-ready products (L0-L2). The data contribution workflow is illustrated on the right. The left (orange) panel summarizes the figures and tables automatically produced by the software to support scientific analysis. These represent the initial set of products provided by the current version of the `disdrodb` package and can be extended or complemented with additional products, as users can modify the open-source software.

By requesting contributors to share only the raw data, DISDRODB removes the time-consuming requirement to convert data into a standardized format and thus simplifies data contributions. This approach contrasts with other continental or global community datasets that require harmonized data submission (Holben et al., 1998; Baldocchi et al., 2001; Illingworth et al., 2007; Pappalardo et al., 2014; Huuskonen et al., 2014; Saltikoff et al., 2019; Kratzert et al., 2023).



The decentralized archive model respects institutional data governance policies, reduces dependence on a central authority, and lowers the barrier to participation. Institutions retain control and authorship over their data and can autonomously modify, update or withdraw their datasets as needed. This aspect is especially important for organizations such as meteorological agencies, which often operate under strict data governance mandates or legal obligations related to data ownership and sharing.

325 Unlike centralized data archives, DISDRODB does not rely on a single group to accept, collect, maintain, and distribute all data. Instead, the decentralized model fosters collaboration and inclusivity within the research community and promotes open data exchange among users and contributors. Lastly, the decentralized nature of the archive is inherently scalable, allowing it to accommodate increasing volumes of data without structural limitations. It also avoids the costs typically associated with centralized storage solutions, such as expenses for disk capacity and dedicated technical staff, making it a cost-effective and

330 sustainable data management approach.

3.3 DISDRODB Data Contribution Process

The data contribution process to DISDRODB has been designed to be simple and time-efficient for contributors and is supported by comprehensive documentation, including tutorials and examples. The four main steps are outlined below:

1. **Design a reader:** Data contributors start by crafting a reader tailored to their raw disdrometer data, leveraging the existing reader templates and tutorials. The software already includes hundreds of readers for various instruments and data formats; therefore, in many cases, adding a new dataset requires only minor adaptations of an existing reader. The reader must be added to the dedicated reader directory within the `disdrodb` software. If the raw data are in text format, the goal of the reader function is to return a `pandas.DataFrame` (McKinney, 2010), where each row corresponds to a measurement interval. If the raw data are in `netCDF4` format, the reader must return an `xarray.Dataset`
- 335 (Hoyer and Hamman, 2017). These formats and libraries are widely adopted and well established within the scientific Python ecosystem, ensuring interoperability and long-term usability of the processed data. Variable names must follow the DISDRODB convention, and time must be expressed in UTC and refer to the end of the measurement interval.
2. **Fill the metadata:** Contributors then fill in a station metadata file and upload it to the DISDRODB Metadata Archive. The metadata file follows a defined structure with mandatory and optional fields. Mandatory fields include the station name, reader name, sensor type, geolocation, and raw data file naming pattern. Optional fields, such as description, authorship, and acknowledgements, can be added at the contributor's discretion.
- 345
3. **Run the automatic quality screening:** At this stage, the DISDRODB automatic screening system rigorously checks the new data, reader, and metadata for compliance with the DISDRODB standards. When producing the DISDRODB L0 products for a station, the system generates a detailed log that lists raw files that are corrupted, empty, or unreadable.
- 350 Contributors can then remove these files or adjust the reader if needed.



4. **Data upload:** Contributors upload the station's raw data to their chosen online repository and incorporate the data URL into the station metadata file. To simplify this step, the `disdrodb` software provides a command-line tool that can automatically upload data to Zenodo, if the user wishes, and update the DISDRODB metadata archive accordingly.

3.4 `disdrodb` software

355 The `disdrodb` software (Ghiggi et al., 2026) is designed to facilitate fast access to and download of disdrometer raw data and to streamline their subsequent scientific processing. As introduced earlier, Sections 4, 5 and 6 describe in detail the Level 0 (L0), Level 1 (L1), and Level 2 (L2) processing chains, respectively. In brief, the L0 chain standardizes raw data into `netCDF4` format; the L1 chain performs resampling and quality control and identifies precipitation phase and hydrometeor types; and the L2 chain derives PSD parameters, fits statistical models, and simulates radar variables. After completion of the L2 processing,
360 the software can automatically produce summary figures and tables to support data analysis.

`disdrodb` enables users to download and generate products from each processing chain with only a few terminal commands (see Figure 1) or Python function calls (see Figure 2). The software offers three computation modes. In single-process mode, files are processed sequentially, which is useful for debugging and testing. In parallel mode, multiple files are processed simultaneously across processor cores. The third mode uses `Dask` (Rocklin, 2015) to build computation graphs representing
365 the processing chain operations, enabling lazy, memory-efficient, distributed execution. The progress of parallel and distributed computation can be monitored in real time through the `Dask` dashboard. Together, these modes provide flexibility from local debugging and analysis to large-scale automated production workflows.

The components of the processing chain can also be used independently outside the main pipeline. This allows users to create customized workflows: for example for internal near-real-time product generation or for producing files that comply
370 with institutional data policies and naming conventions. Examples are provided in the online software documentation.

To accommodate the large variety of data formats, disdrometer models, and user requirements, the `disdrodb` codebase follows a modular design, where each processing chain or software functionality is implemented as an independent module or directory. The software includes two types of editable, human-readable configuration files: sensor configuration files, which define the specific characteristics of each disdrometer model, and product options configuration files, which control the generation of DISDRODB products. This modular design facilitates the integration of new sensor types, algorithms, and models,
375 and supports the development of additional specialized L2 products.

Product configuration files can be easily edited to adjust parameters or add new options. Reasonable defaults are provided, but users can modify settings per sensor type and/or per product temporal resolution. Product archiving is equally customizable. Users can specify the time period for output files (e.g., daily, monthly, yearly, or event-based) and define how data are grouped
380 and stored within subdirectories. Figure 3 provides an example of a product-options configuration file describing the L2E processing chain.

To ensure long-term robustness and maintainability, the `disdrodb` codebase is supported by an extensive automated test suite with high coverage, providing a robust foundation for stable operation and future maintenance. A Continuous Integration (CI) workflow is implemented to regularly run tests and validation checks across multiple operating systems (Windows and



```
import disdrodb

# Define a station
data_source = "EPFL"
campaign_name = "EPFL_2009"
station_name = "10"

# Download the data
disdrodb.download_station(
    data_source=data_source,
    campaign_name=campaign_name,
    station_name=station_name,
)
# Create DISDRODB L0, L1 and L2 products
disdrodb.run_station(
    data_source=data_source,
    campaign_name=campaign_name,
    station_name=station_name,
)
# Create summary figures and tables
disdrodb.create_summary_station(
    data_source=data_source,
    campaign_name=campaign_name,
    station_name=station_name,
)
```

Figure 2. disdrodb Python function calls required to download and generate all DISDRODB products, as well as summary figures and tables, for a given station. Equivalent command-line tools are also available (disdrodb_download_station, disdrodb_run_station, disdrodb_create_summary_station) and are supported on Windows, Linux, and macOS.

385 Linux), with scheduled executions at least once per month to provide early warnings of potential issues arising from changes in dependencies, operating systems, or the broader Python ecosystem. This approach helps to ensure that the software remains functional, up to date, and compatible with evolving scientific computing environments. In summary, disdrodb provides an automated yet highly configurable processing framework that ensures full flexibility while maintaining traceability and reproducibility from data collection to public product release.



```
temporal_resolutions: ["1MIN", "10MIN", "ROLL10MIN"]
archive_options:
  strategy: "time_block"
  strategy_options:
    freq: "day"
    folder_partitioning: "year/month"
product_options:
  compute_spectra: False
  compute_percentage_contribution: False
  minimum_ndrops: 1
  minimum_nbins: 1
  minimum_rain_rate: 0.01
  fall_velocity_model: "Beard1976"
  minimum_diameter: 0
  maximum_diameter: 10
  minimum_velocity: 0
  maximum_velocity: 12
  keep_mixed_precipitation: False
  above_velocity_fraction: null
  above_velocity_tolerance: 2
  below_velocity_fraction: null
  below_velocity_tolerance: 3
  maintain_drops_smaller_than: 1
  maintain_drops_slower_than: 2.5
  maintain_smallest_drops: True
  remove_splashing_drops: True
radar_enabled: True
radar_options:
  frequency: ["S", "C", "X", "Ku", "K", "Ka", "W"]
  num_points: 1024
  diameter_min: 0
  diameter_max: 10
  canting_angle_std: 7
  axis_ratio_model: "Thurai2007"
  permittivity_model: "Turner2016"
  water_temperature: 10
  elevation_angle: [0, 90]
```

Figure 3. Example of an L2E product global configuration file. The archive options control how output files are stored on disk. The production options allow users to customize the processing chain steps; for the DISDRODB L2E product, this includes filtering of the raw spectrum and selection of timesteps to retain or discard (Sect. 6.1). The radar options control the simulation of radar variables (see Sect 6.3 and Table 6 for more information). Radar frequencies can be specified either in GHz or using IEEE (Institute of Electrical and Electronics Engineers) radar band designations.



390 4 DISDRODB L0 products

The DISDRODB Level 0 (L0) processing chain consists of three sub-products – L0A, L0B, and L0C (explained in the following subsections) – which are generated sequentially, starting from the files containing the raw data logged by the disdrometer. All time-varying variables logged by the sensor can be included in the L0A, L0B, and L0C products. Each disdrometer model computes and outputs a specific set of variables and diagnostics; consequently, the content of the raw files and resulting L0 products varies between sensor models and depends on the logging configuration used. `disdrodb` accepts any subset of logged variables, provided that the raw particle spectrum (i.e., the number of particles per diameter bin, and per velocity bin, if available) and the measurement end time (in UTC) are available. Additional meteorological variables from nearby sensors, if available, can also be included in the L0 products. The main objective of the L0 processing chain is to convert raw data into standardized `netCDF4` files with unique time steps and measurement intervals. The uniform L0C data format simplifies scientific analysis and provides a consistent foundation for generating all subsequent DISDRODB products.

4.1 DISDRODB L0A product

The DISDRODB L0A product is generated from the raw text files logged by disdrometers. Raw text files are converted into binary Apache Parquet (Foundation, 2026) files using a reader function, typically defined by the data contributor (see Sect. 3.3). This function reads the raw files and returns a dataframe that conforms to DISDRODB standards. Each row corresponds to a measurement time step, and each column to a variable recorded by the sensor, with column names following the DISDRODB naming convention. Variables that represent arrays – such as the raw particle spectrum, mean particle velocity per diameter bin, or particle number concentration – are stored as single-column string entries containing comma- or semicolon-separated values. These arrays are later extracted and reshaped to their correct dimensions in the L0B processing chain. The dataframe produced by the reader is passed to a sanity-check routine that performs a series of cleaning and standardization steps to produce a DISDRODB-compliant L0A dataset. The procedure removes rows where the measurement time is not available, removes duplicated timestamps, filters out time periods flagged as problematic in the issue file, trims spaces from string fields, strips trailing delimiters from array strings, and converts corrupted numeric entries to *NaN* (Not a Number; the standard floating-point representation for undefined or missing numerical values). Column data types are cast according to DISDRODB definitions, and missing-value flags or out-of-range entries are replaced with *NaN*. All issues encountered during this process are recorded in the corresponding L0A log file, allowing users to diagnose problems, refine the reader where necessary, or manually correct corrupted raw files if needed. Finally, the dataframe is sorted by time and validated to ensure full compliance with DISDRODB L0A standards.

4.2 DISDRODB L0B product

The DISDRODB L0B product is typically generated from the DISDRODB L0A product. A special case occurs when institutions share raw data only as `netCDF4` files; in such cases, the reader function produces the L0B product directly from the raw files, applying the same sanity checks described for the L0A processing chain. In the standard workflow, the L0B chain



ingests the LOA dataframe, parses string arrays (e.g., the raw particle spectrum) into multidimensional arrays, and creates an `xarray.Dataset` with time, diameter, and, if available, velocity dimensions. Coordinate variables defining the bin centers and bounds for diameter and velocity are added, along with station geolocation information (longitude, latitude, and altitude).
425 Each dataset variable is supplemented with Climate and Forecast (CF) convention attributes (Eaton et al., 2024), and variable-specific encodings are applied to minimize disk space usage when the product is written to a `netCDF4` file. The metadata fields defined in the station's metadata file are attached as global attributes, complemented by additional Attribute Convention for Data Discovery (ACDD) fields (ESIP, 2015).

4.3 DISDRODB L0C product

430 The DISDRODB L0C product aims to produce files with fixed time periods (e.g., daily or monthly), unique measurement intervals, and no duplicated time steps. If a disdrometer sensor logs a variable representing the actual measurement interval and this value differs from the expected one(s) specified in the station metadata file, the L0C chain removes the affected time steps. In some logging configurations, raw files may include data from previous days (for instance, due to transmission buffers, temporary storage delays, or manual file handling). When multiple LOB files reflecting these raw data are concatenated, the
435 L0C chain identifies and removes any resulting duplicated time steps. When duplicated time steps contain inconsistent values, a warning is recorded in the product log file, and the conflicting entries are removed. Because some sensors can or have operated with measurement intervals that varied over time, although this is relatively uncommon, the L0C chain separates the data into distinct `xarray` datasets, each corresponding to a single measurement time interval. This separation ensures accurate temporal resampling during the subsequent DISDRODB L1 processing stage and prevents the introduction of downstream estimation
440 errors, for example in the computation of the particle number concentration or precipitation rate. Each dataset is then processed independently in the remaining L0C steps.

Once a homogeneous measurement interval has been confirmed, its duration in seconds is stored as a coordinate in the `xarray.Dataset`. The time axis is corrected, if necessary, to account for drifting seconds. This adjustment aligns small timing offsets – such as time stamps recorded at 00:01, 01:02, or 02:03 when the expected measurement interval is 60 s – to
445 exact multiples of the interval (e.g., 00:00, 01:00, 02:00). The correction typically also enforces that time steps end with 00 seconds, unless this is incompatible with the defined measurement interval. To assess temporal continuity, a quality-control variable (`qc_time`) is computed to indicate whether each time step is isolated, has at least one neighboring measurement, or belongs to a continuous sequence. This check also considers continuity across adjacent files or time periods. Finally, a time-step regularity check is logged in the L0C log file. This diagnostic warns for the presence of highly intermittent measurements
450 or recurring irregular time differences between observations, which may suggest that the sensor operated with a measurement interval different from the one expected. This information can be used to correct the expected measurement interval(s) in the station metadata file.



5 DISDRODB L1 products

The DISDRODB L1 processing chain performs temporal resampling of the raw particle size distributions, applies spectrum-
455 level quality control, and classifies the precipitation phase and hydrometeor types. These steps ensure that all disdrometer observations, despite differences in sensor design, sampling frequency, and logging configuration, are homogenized in both temporal resolution and physical interpretation. The following subsections describe the main components of the L1 chain: temporal resampling (Sect. 5.1) and hydrometeor classification (Sect. 5.2), along with their associated quality-control procedures and output variables.

460 5.1 Temporal resampling

Disdrometer sensors operate at heterogeneous native temporal resolutions, typically between 10 and 60 seconds, with some networks adopting longer intervals up to 5 or even 10 minutes. To handle this variability, the DISDRODB L1 processing chain aggregates the raw particle spectra and auxiliary meteorological variables to the temporal resolution specified by the user, constrained to multiples of the native measurement interval. Depending on the research objective, data can be aggregated at 1-,
465 5-, or 10-minute intervals to represent different spatio-temporal scales of the PSD. To avoid data loss when aggregating over fixed blocks (e.g., 2-minute intervals), `disdrodb` offers a rolling-window resampling option, which increases the number of aggregated samples by performing overlapping integrations (e.g., producing 5-minute integrated data every 1 minute). A quality-control variable, `qc_resampling`, reports the fraction of missing time steps within each temporal aggregation window, with values ranging from 0 (no missing data) to 1 (all time steps missing). This information enables users to apply a
470 posteriori filtering and identify potentially biased aggregated estimates.

5.2 Hydrometeor classification

The hydrometeor classification (HC) module analyses the raw particle size-velocity spectrum recorded by disdrometers to identify the dominant hydrometeor type and precipitation phase at each time step. It operates on the raw two-dimensional particle number spectrum (diameter-velocity) and, when available, incorporates auxiliary environmental variables such as air
475 or sensor temperature. Before classification, sensor-specific filters remove noisy bins, typically the first diameter or velocity classes affected by environmental noise and the low sensitivity of the instruments. For disdrometers that do not measure fall velocity (e.g., RD80, ODM470), the HC module is not applied.

Figure 4 illustrates the partitioning of the raw particle size-velocity spectrum, based on Friedrich et al. (2013). The algorithm defines masks for different hydrometeor categories – including drizzle, rain, graupel, hail, snow, and snow grains – using
480 theoretical and empirical fall-velocity-diameter relationships. Each mask isolates the region of the spectrum consistent with the expected velocity-size range of a given hydrometeor type. Because fall velocity depends on air density, these masks are dynamically adjusted based on the instrument's altitude. Appendix B provides details on the fall-velocity models implemented in `disdrodb`.



485 Graupel is assumed to have diameters between 1 and 5 mm, while hail particles exceed 5 mm. Snow is identified as particles with estimated fall velocities up to 6.5 m s^{-1} . Artefacts such as drop splashing and margin fallers are also explicitly recognized: splashing generates small particles with unrealistically low fall velocities, whereas margin fallers show abnormally high fall velocities relative to their underestimated diameters. Additionally, strong winds ($> 20 \text{ m s}^{-1}$) combined with intense rainfall can produce large but slow-falling particles ($D > 5 \text{ mm}$, $v < 1 \text{ m s}^{-1}$), as reported by Friedrich et al. (2013).

490 From these raw particle size-velocity spectrum masks, the HC algorithm computes particle counts, relative fractions and occupied bins for each hydrometeor type, then applies a set of physically based decision rules to assign a preliminary hydrometeor label. This logic distinguishes drizzle, rain, snow, and other frozen hydrometeors such as graupel, hail, and ice pellets, while also identifying non-hydrometeor particles and artefacts related to drop splashing, margin fallers and strong winds (Friedrich et al., 2013). When temperature data are available, the classification is refined: thresholds near $\pm 5^\circ\text{C}$ adjust the liquid-solid boundary, improving the separation between drizzle and snow grains (ice crystals and prisms) and between graupel ($T > 0$ 495 $^\circ\text{C}$) and ice pellets or sleet ($T < 0 \text{ }^\circ\text{C}$). In addition to hydrometeor and precipitation-type classification, the HC module also outputs several quality-control flags, along with the total particle count and class-specific counts. All variables produced by the HC module are listed in Table 2.

Figure 5 illustrates the time-accumulated raw diameter-velocity particle number spectra $n(D, V)$ for three selected events, each characterized predominantly by a different precipitation type: liquid, mixed, and solid. The temporal evolution of the raw particle number concentration $N(D)$ during these events, together with the precipitation type inferred by the HC module, 500 is presented through quicklook visualizations. The disdrometer station shown in the figure was not used during algorithm development, illustrating the ability of the HC algorithm to generalize to unseen data.

To the best of our knowledge, `disdrodb` provides the first open-source disdrometer-based hydrometeor classification algorithm capable of detailed partitioning of hydrometeor classes and precipitation phases. In contrast to sensor firmware-specific, undisclosed, proprietary algorithms, it accounts for altitude-dependent air density affecting particle fall velocity, and 505 applies a transparent, consistent classification scheme across all DISDRODB stations.

Comparisons with weather codes reported by the instrument's internal software show very good agreement. Although the current results are promising, ongoing work aims to further refine the HC module and evaluate its performance against independent ground-based instruments, with particular focus on the identification of frozen particles. Planned developments include 510 extending the classification to generate standard World Meteorological Organization (WMO) SYNOP, METAR/SPECI, and NWS weather codes (WMO2019).



Table 2. Hydrometeor classification, precipitation phase, flags, and particle count variables produced by the `disdrodb` classification module.

Variable	Meaning	Notes
<code>hydrometeor_type</code>	Dominant hydrometeor class	–2 = no hydrometeor, –1 = undefined, 0 = no precipitation, 1 = drizzle, 2 = drizzle + rain, 3 = rain, 4 = mixed, 5 = snow, 6 = snow grains / ice crystals, 7 = ice pellets, 8 = graupel, 9 = hail.
<code>precipitation_type</code>	Precipitation phase classification	–2 = undefined, –1 = no precipitation, 0 = rainfall, 1 = snowfall, 2 = mixed phase.
<code>flag_graupel</code>	Graupel occurrence flag	0 = none, 1 = low-density graupel ($\rho < 500 \text{ kg m}^{-3}$), 2 = high-density graupel ($\rho \geq 500 \text{ kg m}^{-3}$).
<code>flag_hail</code>	Hail occurrence flag	0 = none, 1 = small hail ($\leq 8 \text{ mm}$), 2 = large hail ($> 8 \text{ mm}$).
<code>flag_splashing</code>	Splash artefact flag	1 in presence of low-velocity particles ($< 0.6 \text{ m s}^{-1}$) caused by rain drop splashing.
<code>flag_wind_artefacts</code>	Wind artefact flag	1 in presence of artefacts consistent with strong-wind effects in high rainfall rates (Friedrich et al., 2013).
<code>flag_spikes</code>	Isolated spike flag	1 in presence of no particle detections in neighbouring timesteps.
<code>flag_noise</code>	Non-hydrometeor flag	1 in presence of only environmental noise.
<code>n_particles</code>	Total particle count	Sum across all diameter–velocity bins.
<code>n_low_density_graupel</code>	Low-density graupel count	Graupel particles with bulk density $\rho < 400 \text{ kg m}^{-3}$.
<code>n_high_density_graupel</code>	High-density graupel count	Graupel particles with bulk density $\rho \geq 400 \text{ kg m}^{-3}$.
<code>n_small_hail</code>	Small hail particle count	Hail particles with diameter $\leq 8 \text{ mm}$.
<code>n_large_hail</code>	Large hail particle count	Hail particles with diameter $> 8 \text{ mm}$.
<code>n_splashing</code>	Splash particle count	Low-velocity rain drops identified as splash artefacts.
<code>n_margin_fallers</code>	Margin fallers particle count	Rain drops with fall velocity far above expected terminal velocity.

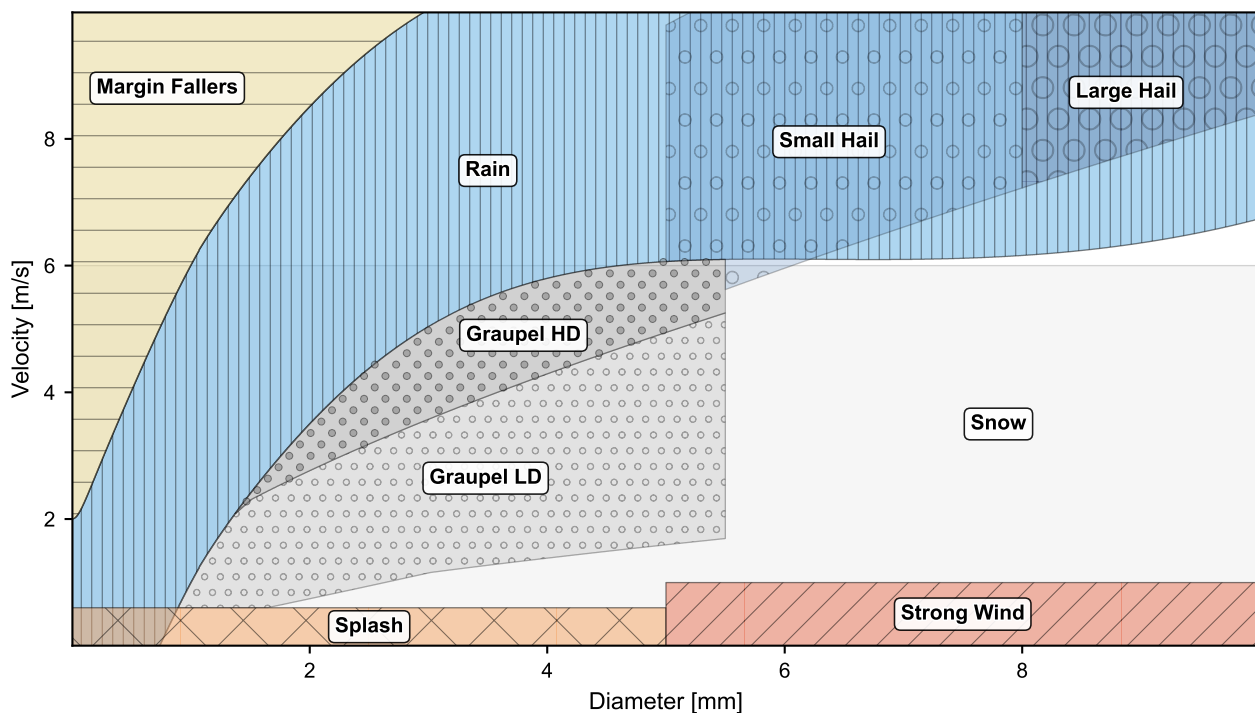


Figure 4. Schematic illustration of particle size-velocity spectrum partitioning derived from theoretical fall velocity-particle size relationships (see Appendix B). The hydrometeors masks are automatically adjusted according to the station altitude.

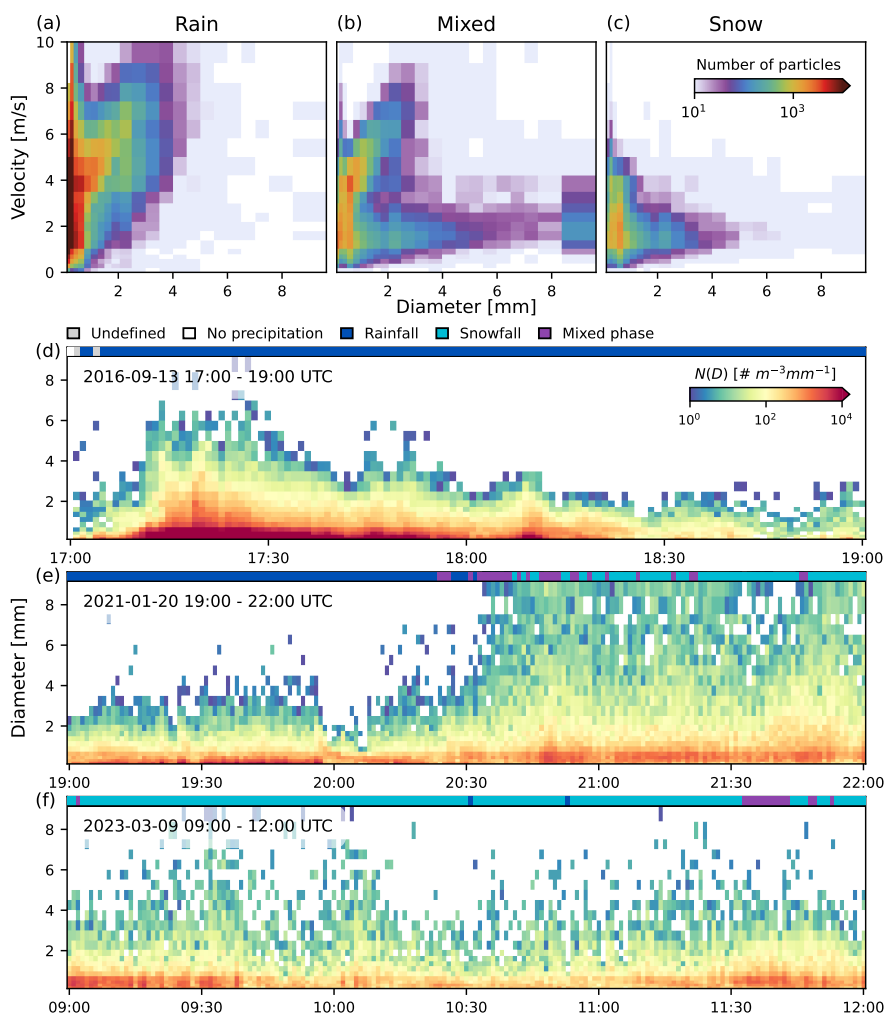


Figure 5. Particle size distributions for liquid, mixed and solid precipitation during three selected events observed by a Thies LPM disdrometer installed at the Whitworth Meteorological Observatory, University of Manchester, United Kingdom. (a-c) Time-accumulated raw diameter-velocity particle number spectra $n(D, V)$ for events predominantly characterized by (a) rain, (b) mixed-phase precipitation, and (c) snow. Colors indicate the total number of detected particles per diameter-velocity bin during the event. (d-f) Temporal evolution of the raw particle number concentration $N(D)$ for the same events. The colored bar at the top of each panel indicates the precipitation type inferred by the HC module. The disdrodb functions `plot_spectrum` and `plot_dsd_quicklook` allow easy reproduction of these figures with every DISDRODB product.



6 DISDRODB L2 product

In the L2 processing chains, `disdrodb` allows users to retrieve integral parameters and polarimetric radar variables from empirical (L2E) or modelled (L2M) particle size distributions. For rainfall, the relevant physical relationships are sufficiently well constrained that its microphysical and bulk properties can be reliably estimated. Raindrops can be reasonably approximated as spheroids of nearly constant density and known size-dependent axis ratio, with fall velocity primarily governed by their equivolume spherical drop diameter. This enables the derivation of drop size distribution (DSD) parameters from the particle sizes measured by disdrometers, as well as the simulation of polarimetric radar observables through T-matrix scattering models under the spheroidal particle assumption.

In contrast, the characterization of snow particles is far more uncertain. Snowflakes exhibit substantial variability in shape, density, and fall behavior, depending on their growth habit (e.g., dendritic, columnar, or aggregate structures) and degree of riming (Locatelli and Hobbs, 1974; Mitchell et al., 1990; Mitchell, 1996; Barthazy and Schefold, 2006; Brandes et al., 2008; Kikuchi et al., 2013; Grazioli et al., 2022; Vázquez-Martín et al., 2021a, b). Converting the horizontally projected particle size measured by disdrometers, which is itself uncertain due to internal air pockets and the different optical properties of ice relative to liquid water, into physically meaningful quantities such as maximum dimension, bulk density, mass, or fall velocity requires strong, case-dependent assumptions (Battaglia et al., 2010). Estimating radar polarimetric signatures of snow and mixed-phase precipitation is equally challenging, as they depend on particle orientation, aspect ratio, internal structure, degree of riming or melting and the air-ice mixture within the scattering volume (Liu, 2008; Hong, 2007; Leinonen et al., 2012; Liao and Meneghini, 2013; Kneifel et al., 2018, 2020; Ori et al., 2021).

Because of these fundamental uncertainties, the current L2 processing chains in `disdrodb` focus on rainfall, for which particle microphysics and electromagnetic scattering properties are relatively well constrained. However, the software has been designed to facilitate future extensions, toward solid and mixed-phase precipitation quantification, once robust parameterizations and suitable validation datasets become available.

6.1 DISDRODB L2E product

The DISDRODB L2E (empirical) processing chain computes drop size distribution (DSD) integral parameters and simulates polarimetric radar observables using T-matrix scattering calculations. The following paragraphs describe the general workflow, while Appendix C and E detail the computation of DSD bulk (integrated) quantities (see Table 3) and the simulation of polarimetric variables, respectively (see Table 6).

The chain takes as input an L1 dataset containing the raw particle number spectrum and first selects time steps classified as liquid precipitation, based on the `precipitation_type` variable when available. Then, it filters the two-dimensional spectrum to retain only physically consistent raindrop bins, applying user-defined limits on diameter and fall velocity. By default, drops smaller than 0.25 mm or larger than 10 mm are excluded. Although the smallest bins contribute negligibly to rainfall rate and mass-weighted moments, they can introduce significant noise in lower-order moments such as the total drop number concentration (N_t) (see Eq. C3).



545 When the full diameter-velocity particle number spectrum $n(D, V)$ is available (i.e., for optical disdrometers other than ODM470), the algorithm filters the spectrum based on the theoretical terminal fall velocity of raindrops, combined with user-defined filtering criteria. Only particles whose measured velocities lie within a specified percentage or absolute tolerance around the expected terminal velocity are retained. This velocity-based filtering step removes spurious detections such as splashing or margin fallers and enforces physical consistency between particle size and velocity. Typical thresholds used in the literature
550 range between $V - 3 \text{ m s}^{-1}$ and $V + 4 \text{ m s}^{-1}$, or between 25-75 % below and above the theoretical fall velocity (Raupach and Berne, 2015; Friedrich et al., 2013; Jaffrain and Berne, 2011; Tokay et al., 2001). These thresholds must consider sensor uncertainty and the natural occurrence of drops falling at sub- or super-terminal velocities due to microphysical processes or turbulence (Montero-Martínez et al., 2009; Larsen et al., 2014; Montero-Martínez and García-García, 2016). Under strong
555 horizontal winds, changes in the orientation of large raindrops modify the aerodynamic drag acting on them, thereby altering their terminal fall speed. Preliminary analyses of DISDRODB stations also show that instruments mounted on roofs report, on average, lower fall velocities than expected and broader velocity distributions, likely caused by turbulence and vertical wind. To avoid inadvertently removing valid particles and underestimating parameters such as rain rate, thresholds must therefore be chosen with care.

For optical disdrometers that report the full diameter-velocity particle number spectrum $n(D, V)$, the drop number concentration $N(D)$ is computed in two ways: (1) using the measured fall velocity and (2) using the theoretical terminal fall
560 velocity estimated from the specified drop fall-velocity model. For impact disdrometers and ODM470, which record only the one-dimensional spectrum $n(D)$, $N(D)$ is estimated solely from the theoretical terminal fall velocity.

From $N(D)$, the L2E processing chain derives a comprehensive set of DSD bulk (integrated) quantities, drop-size and bin statistics, and polarimetric radar variables simulated through T-matrix scattering (see Sect. 6.3). When $n(D, V)$ is available,
565 additional quantities such as kinetic energy variables and rainfall rate are directly computed from the filtered spectrum $n(D, V)$ using the instrument-measured fall velocity. This allows for direct comparison between quantities derived from $N(D)$ and those calculated from the measured spectrum. The processing chain is fully customizable, and optional thresholds can be applied to exclude time steps with insufficient data quality – such as those containing too few drops, too few populated bins, or rain rates below a configurable minimum (see Fig. 3).

570 All variables generated by the L2E processing chain are summarized in Table 3; the simulated radar polarimetric variables are presented separately in Table 6. Together, these variables provide the foundation for a comprehensive analysis of statistical relationships among DSD bulk quantities and radar observables, supporting the development and evaluation of radar retrieval algorithms and microphysical parametrization schemes. Figure 6 illustrates the relationships among key DSD parameters, while Figure 7 presents the power-law dependencies between rainfall rate and simulated radar variables. These types of diagnostic
575 figures are automatically generated by `disdrodb` as part of the station summary product.

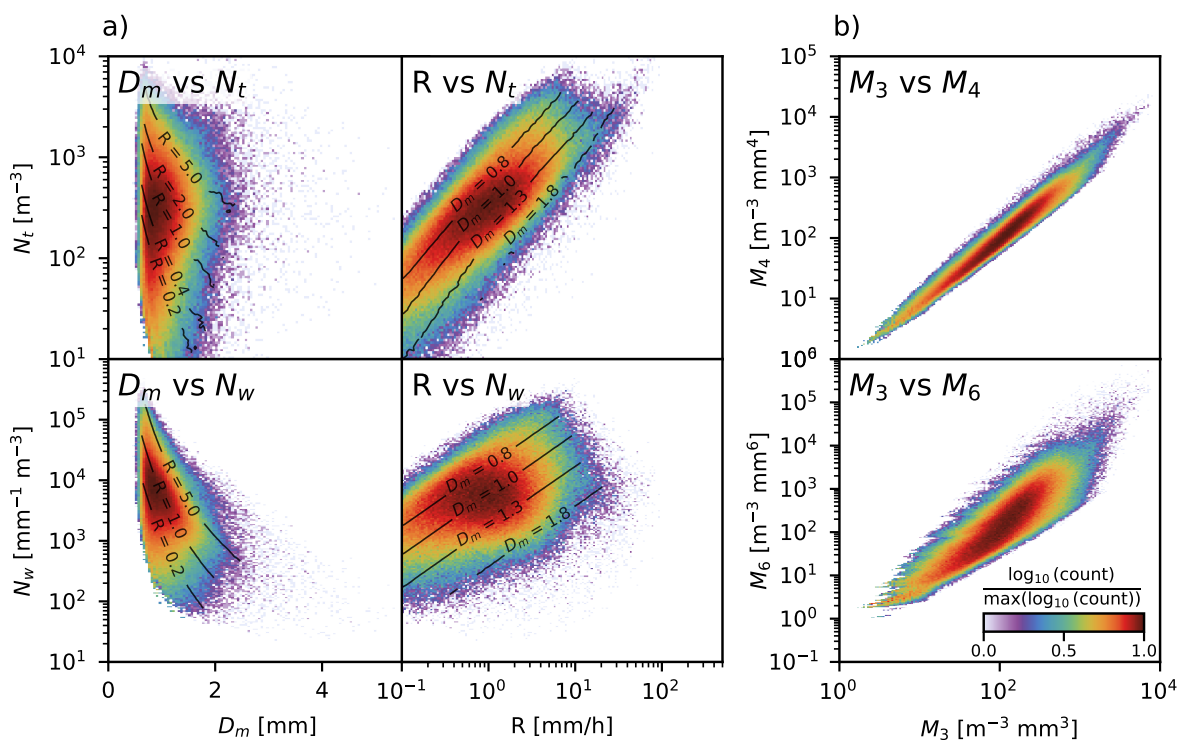


Figure 6. Two-dimensional histograms illustrating the relationships among DSD bulk quantities derived from 15 years of measurements collected by a Thies LPM disdrometer installed at the Whitworth Meteorological Observatory, Manchester University, United Kingdom. Colors represent the normalized logarithmic frequency of occurrence. a) Relationships among D_m , N_t , N_w and R . Black contour lines indicate median iso- R values in the left column and median iso- D_m values in the right column. A decreasing trend of N_w with increasing D_m is observed, while R generally increases with both D_m and N_t . No clear relationship is evident between D_m and N_t , nor between N_w and R . (b) Relationships between the third moment M_3 and higher-order moments M_4 (top) and M_6 (bottom), commonly used in double-moment DSD normalization approaches (see Appendix D). Similar diagnostic plots exploring additional DSD bulk relationships are automatically generated by `disdrodb` as part of the station summary figures.

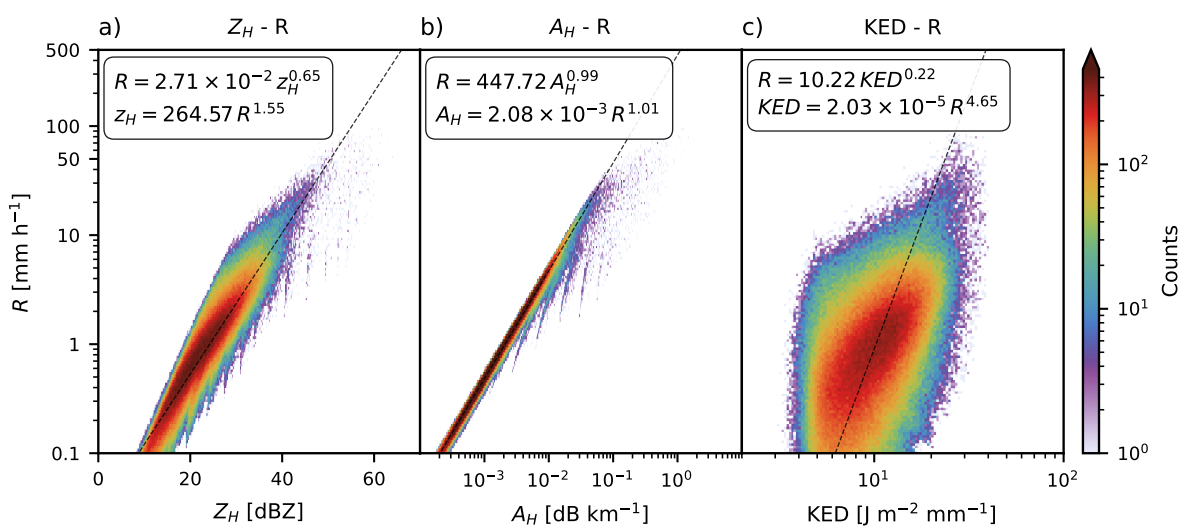


Figure 7. Two-dimensional histograms illustrating power-law relationships between rainfall rate R and selected radar and microphysical variables derived from 15 years of disdrometer measurements at Whitworth Meteorological Observatory. Colors indicate the frequency of occurrence (counts), while black dashed lines represent the fitted power-law relationships shown in each panel. Power-law relationships are fitted by default using the robust RANSAC algorithm (Fischler and Bolles, 1981) applied to the median values within each bin; weighted nonlinear least squares is also available as an alternative. Inverse power-law relationships are obtained by algebraic inversion of the fitted models. (a) C-band horizontal reflectivity factor $Z_{H,C}$ versus R . The z_H in the power-law expressions denotes reflectivity in linear units, and the regression is performed on z_H . (b) C-band horizontal specific attenuation $A_{H,C}$ versus R (c) Kinetic energy density (KED) versus R . Similar diagnostic plots, including additional radar variables at multiple frequency bands and kinetic energy relationships, are automatically generated by `disdrodb` as part of the station summary figures.



Table 3. Summary of DSD spectral (size-resolved) and bulk (integrated) quantities included in the current version of DISDRODB L2E and L2M products, with units, and equation references. The set of variables can be extended by users through modification of the open-source `disdrodb` software.

Name	Description	Units	Equation
<i>Spectral (size-resolved) quantities</i>			
$N(D)$	Drop number concentration spectrum	$\text{m}^{-3} \text{mm}^{-1}$	Eq. (C1)
$m(D)$	Drop mass concentration spectrum	$\text{g m}^{-3} \text{mm}^{-1}$	Eq. (C4)
<i>Bulk (integrated) quantities</i>			
M_n	n -th moment of the DSD	$\text{mm}^n \text{m}^{-3}$	Eq. (C2)
N_t	Total drop number concentration	m^{-3}	Eq. (C3)
LWC	Liquid water content	g m^{-3}	Eq. (C5)
Z	Rayleigh radar reflectivity factor	dBZ	Eq. (C6)
R	Rain rate from $N(D)$	mm h^{-1}	Eq. (C7)
P	Rain accumulation	mm	Eq. (C8)
TKE	Total kinetic energy	J m^{-2}	Eq. (C9)
KEF	Kinetic energy flux	$\text{J m}^{-2} \text{h}^{-1}$	Eq. (C10)
KED	Kinetic energy per rainfall depth	$\text{J m}^{-2} \text{mm}^{-1}$	Eq. (C11)
D_{50}	Median volume diameter	mm	Eq. (C12)
D_m	Mass-weighted mean diameter	mm	Eq. (C13)
σ_m	Std. deviation of mass spectrum	mm	Eq. (C14)
N_w	Normalized Gamma intercept parameter	$\text{mm}^{-1} \text{m}^{-3}$	Eq. (D7)



6.2 DISDRODB L2M products

The DISDRODB L2M (modelling) processing chain allows users to fit parametric DSD models on the observed empirical DSD. It then computes integral DSD parameters and polarimetric radar variables from the modelled distribution. The following paragraphs describe the general workflow and applications of L2M products. Appendix D provides the mathematical definition
580 of the parametric DSD models.

The L2M chain takes as input an L2E dataset containing the observed drop number concentration $N(D)$. For each timestep, the software estimates the parameters of the selected statistical models. The software implements six widely used parametric DSD models: lognormal, exponential, gamma, normalized gamma, generalized gamma, and normalized generalized gamma. Table 4 summarizes these models and their parameters.

585 Several fitting methods are available, from brute-force grid search (GS) to unconstrained or constrained maximum likelihood (ML) and the method of moments (MOM). The models to be fitted are defined in the DISDRODB product configuration files, and users can adjust the optimization settings, as well as specify optional thresholds restricting the timesteps on which to fit the statistical models. For microphysical DSD studies, we recommend estimating the model parameters by minimizing errors in $N(D)$. For the development or validation of radar and satellite retrievals, the fitting procedure should take care to also minimize
590 errors in integral parameters such as LWC, R or Z . The GS routine provides the flexibility to minimize multiple objectives through a weighted loss function and custom variables transformations.

An evaluation of fitting procedures (not shown here) indicates that the method of moments produces inaccurate parameters even when the observed DSD follows the assumed parametric model functional form. Maximum-likelihood estimators may also converge to biased parameters because of local minima in the loss function. Therefore, although slightly more computationally
595 demanding, we recommend estimating model parameters using a grid search that minimizes the sum of squared errors of $N(D)$ as the primary objective, optionally complemented by the mean absolute or squared error of a bulk DSD quantity such as LWC or Z .

Once the model parameters are estimated, integral DSD parameters and polarimetric radar variables are computed from the modelled drop number concentration $N_{\text{MODEL}}(D; \Theta)$. A set of goodness-of-fit (GOF) statistics is computed to assess
600 the accuracy of each fitted model; the metrics are summarized in Table 5. Users may also compute additional error metrics, for example by comparing rain rate or radar variables derived from the L2E product with those obtained from the modelled $N_{\text{MODEL}}(D; \Theta)$ in the L2M product.

Among the GOF metrics, the Kullback-Leibler divergence (KLDiv) is commonly used to quantify the similarity between parametric DSD models and observations and to identify the statistical model that best fits the observed distributions (Adirosi
605 et al., 2016; Cugerone and Michele, 2015; Gatidis et al., 2020). Figure 8a evaluates the adequacy of the DSD parametric models implemented in `disdrodb` in representing observed DSDs at 1 minute temporal resolution. Models with a larger number of free parameters (see Table 4) provide increased structural flexibility and are thus better suited to capture the shape variability of the observed DSDs, but they also increase the risk of overfitting.



610 However, for real applications, the number of free parameters $N_{\text{MODEL}}(D; \Theta)$ is constrained by the amount of inde-
pendent information available. Dual-frequency and polarimetric radar DSD retrieval algorithms therefore typically adopt a
615 $N_{\text{MODEL}}(D; \Theta)$ with two free parameters (Zhang et al., 2001; Liao et al., 2014; Gatidis et al., 2022; Lee et al., 2023; Ladino-
Rincon et al., 2025).

The double-normalization framework (Lee et al., 2004), combined with long-term DSD observations, enables the identifica-
tion and fitting of a parametric model, assumed to be invariant in space and time, that expresses the DSD as a function of only
615 two moments (see Appendix D3). These moments and their corresponding general characteristic diameter (D_c ; Eq. (D8)) and
intercept (N_c ; Eq. (D9)) can then be retrieved from the radar observables either through empirical relationships or machine
learning algorithms, and subsequently used to reconstruct the DSD (Raupach and Berne, 2017; Raupach et al., 2019; Shin
et al., 2024). Figure 9 illustrates the observed double-moment normalized DSDs, corresponding fitted normalized parametric
models, and the relationships between the D_c and N_c parameters and radar reflectivities at Ku and Ka bands.

Table 4. Summary of DSD parametric models implemented in `disdrodb`.

DSD Model	Parameters	Equation	References
Lognormal	$N(D; N_t, \mu, \sigma)$	Eq. (D1)	Feingold and Levin (1986); Maitra and Gibbins (1999)
Generalized Gamma	$N(D; N_t, \Lambda, \mu, c)$	Eq. (D2)	Maur (2001); Lee et al. (2004)
Gamma	$N(D; N_0, \Lambda, \mu)$	Eq. (D3)	Ulbrich (1983)
Exponential	$N(D; N_0, \Lambda)$	Eq. (D4)	Marshall and Palmer (1948)
LWC-Normalized Gamma	$N(D; N_w, D_m, \mu)$	Eq. (D5)	Testud et al. (2001)
Nt-Normalized Gamma	$N(D; N_t, D_m, \mu)$	Eq. (D6)	Tokay and Bashor (2010)
Normalized Generalized Gamma	$N(D; N_c, D_c, \mu, c, i, j)$	Eq. (D10)	Lee et al. (2004)



Table 5. Goodness-of-fit metrics computed between observed and L2M predicted DSDs. For a diameter bin D_i with width ΔD_i , the probability mass is defined as $p(D_i) = \frac{N(D_i)\Delta D_i}{N_t}$. The cumulative distribution function is defined as $F(D_i) = \sum_{i \leq n} p(D_i)$.

Name	Formula	Description
R^2	$\text{corr}(N_{\text{obs}}(D), N_{\text{pred}}(D))^2$	Squared Pearson correlation coefficient
MAE	$\frac{1}{n} \sum_{i=1}^n N_{\text{obs}}(D_i) - N_{\text{pred}}(D_i) $	Mean absolute error
MaxAE	$\max_i N_{\text{obs}}(D_i) - N_{\text{pred}}(D_i) $	Maximum absolute error
RelMaxAE	$\frac{\max_i N_{\text{obs}}(D_i) - N_{\text{pred}}(D_i) }{\max_i N_{\text{obs}}(D_i)}$	Relative maximum absolute error
PeakDiff	$\max [N_{\text{obs}}(D)] - \max [N_{\text{pred}}(D)]$	Difference at the distribution peak
RelPeakDiff	$\frac{\max [N_{\text{obs}}(D)] - \max [N_{\text{pred}}(D)]}{\max [N_{\text{obs}}(D)]}$	Relative difference at the distribution peak
DmodeDiff	$D_{\text{mode,obs}} - D_{\text{mode,pred}}$	Difference between mode diameters
NtDiff	$\sum_i N_{\text{pred}}(D_i) \Delta D_i - \sum_i N_{\text{obs}}(D_i) \Delta D_i$	Difference in total number concentration
KLDiv	$\sum_i p_{\text{obs}}(D_i) \log \left(\frac{p_{\text{obs}}(D_i)}{p_{\text{pred}}(D_i)} \right)$	Kullback–Leibler divergence between DSDs
WD	$\sum_i F_{\text{obs}}(D_i) - F_{\text{pred}}(D_i) \Delta D_i$	Wasserstein (Earth Mover’s) distance between DSDs
KS	$\max_i F_{\text{obs}}(D_i) - F_{\text{pred}}(D_i) $	Kolmogorov–Smirnov statistic

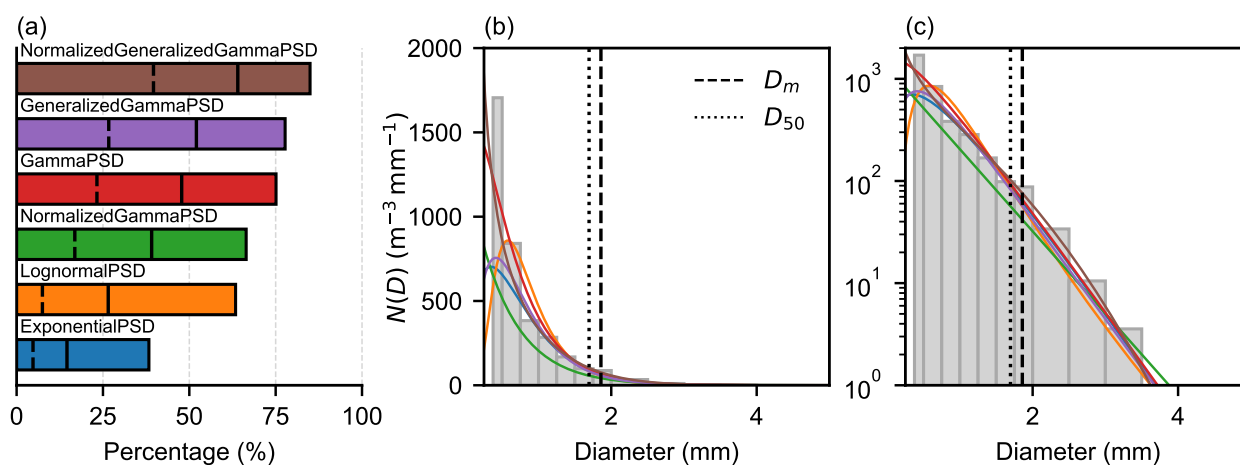


Figure 8. Illustration of the adequacy of DSD parametric models in reproducing DSDs observed during 15 years of disdrometer measurements at the Whitworth Meteorological Observatory. (a) Percentage of total observations well fitted by each DSD parametric model. Model parameters are estimated using a grid-search procedure minimizing the sum of squared errors (SSE) of $\log_{10}(N(D))$ together with the absolute error in Z . Model performance is evaluated using the Kullback-Leibler divergence (KLDiv); vertical markers indicate the percentage of cases with KLDiv below 0.025, 0.05, and 0.1. (b-c) Example of an observed DSD at a given time step fitted with the various parametric models, shown on (b) linear and (c) logarithmic y -axis scales. Vertical lines indicate the mass-weighted mean diameter (D_m , dashed) and the median volume diameter (D_{50} , dotted). Drops with diameters larger than D_{50} contribute half of the liquid water content within the sampled air volume.

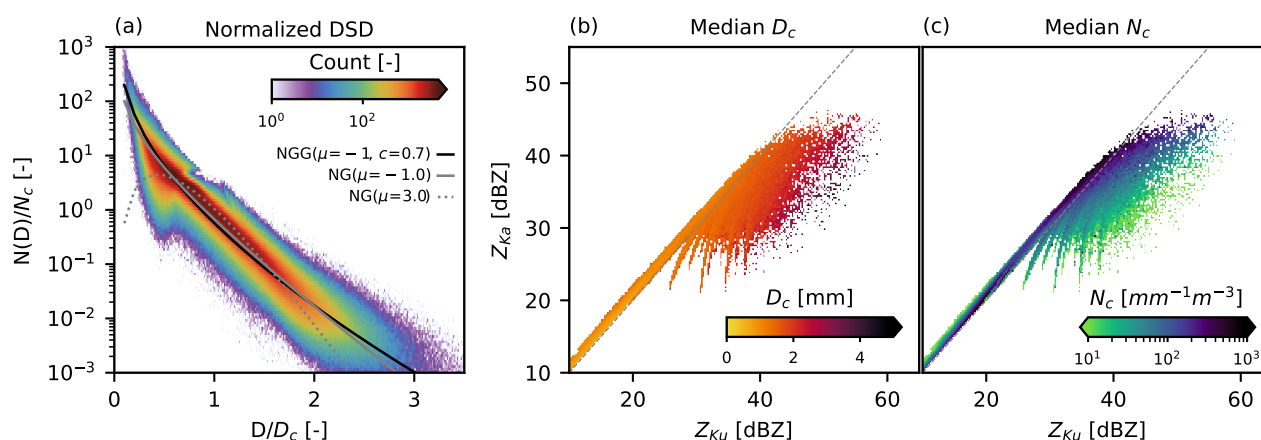


Figure 9. Double-moment normalization analysis and radar relationships derived from 15 years of disdrometer measurements at Whitworth Meteorological Observatory. (a) Observed double-moment normalized DSDs expressed as $N(D)/N_c$ versus D/D_c , using moments $i = 3$ and $j = 4$. Colors indicate the frequency of occurrence (counts). The solid gray and black curves show fitted normalized gamma (NG) and normalized generalized gamma (NGG) models, while the gray dashed line shows the NG parametric model (with $\mu = 3$) currently adopted in GPM DPR retrievals. (b) Relationship between Ku-band reflectivity Z_{Ku} and Ka-band reflectivity Z_{Ka} , with color shading indicating the observed median general characteristic diameter D_c . D_c grows monotonically with increasing reflectivities. (c) Relationship between Ku-band reflectivity Z_{Ku} and Ka-band reflectivity Z_{Ka} , with color shading indicating the observed median general characteristic intercept parameter N_c . Retrieval of N_c becomes particularly challenging for $Z_{Ku} < 30$ dBZ, where large variation in N_c produces only small changes in Z_{Ka} . This region is associated with negative dual-frequency ratio (DFR) values and corresponds to the area above the 1:1 dashed gray line.



620 **6.3 Radar simulations with T-matrix**

Table 6. List of the T-matrix configuration parameters and the radar variables calculated for both DISDRODB L2E and L2M products.

Name	Units	Description	Equation
Configuration parameters			
frequency	GHz	Radar operating frequency	
diameter_min	mm	Minimum drop diameter used to discretize the DSD	
diameter_max	mm	Maximum drop diameter used to discretize the DSD	
num_points		Number of diameter bins used to discretize the DSD	
canting_angle_std	deg	Std. deviation of the canting-angle Gaussian distribution	
axis_ratio_model		Axis-ratio model for hydrometeor shape	
permittivity_model		Permittivity model for refractive index computations	
water_temperature	°C	Water temperature for permittivity model	
elevation_angle	deg	Radar elevation angle (90° for vertical pointing)	
Polarimetric radar variables			
DBZH	dBZ	Reflectivity factor (H-pol)	(E2)
DBZV	dBZ	Reflectivity factor (V-pol)	(E3)
ZDR	dB	Differential reflectivity	(E5)
RHOHV		Copolar correlation coefficient	(E6)
LDRH	dB	Linear depolarization ratio (H-pol)	(E8)
LDRV	dB	Linear depolarization ratio (V-pol)	(E8)
KDP	deg km ⁻¹	Specific differential phase	(E9)
DELTAHV	deg	Backscatter differential phase	(E7)
AH	dB km ⁻¹	Specific attenuation (H-pol)	(E10)
AV	dB km ⁻¹	Specific attenuation (V-pol)	(E11)
ADP	dB km ⁻¹	Specific differential attenuation	(E12)

Rainfall polarimetric radar variables in DISDRODB are simulated using electromagnetic scattering calculations based on the T-matrix method, which numerically solves Maxwell’s equations for scattering by non-spherical raindrops (Mishchenko et al., 1996). The simulations can be based either on the empirical drop number concentration available in the L2E products or on the parametric DSD models estimated in the L2M products. The `disdrodb` wrapper around `PyTMatrix` (Leinonen, 2014) enables vectorized and parallelized computations, provides flexible configuration of the radar settings and microphysical assumptions, and manages caching of the corresponding scatterer objects to avoid redundant T-matrix simulations. It also allows users to easily explore the sensitivity of the simulated radar variables to different parameter choices (Fig E2). Table 6 summa-



630 rizes the user-configurable parameters and the simulated radar variables, while Appendix E provides additional mathematical details on the T-matrix method and the definitions of the simulated radar quantities.

635 Radar variables are computed in two steps. First, the scattering amplitude matrices obtained from T-matrix calculations are evaluated in backward-scattering geometry, which corresponds to the radar-receiving direction and is required to compute horizontal and vertical polarization reflectivities (DBZH and DBZV), as well as polarimetric variables such as differential reflectivity (ZDR), linear depolarization ratios (LDR), backscatter differential phase (DELTAHV) and the co-polar correlation coefficients (RHOHV). Second, the same scattering quantities are evaluated in forward-scattering geometry, which governs how the radar signal propagates through the medium and is therefore used to compute the propagation-related variables such as the specific differential phase (KDP), specific attenuation at horizontal and vertical polarizations (AH and AV), and the differential attenuation (ADP).

640 The radar frequency and elevation angle determine the scattering regime and the viewing geometry used in the T-matrix calculations. The minimum and maximum drop diameter (`diameter_min` `diameter_max`), along with the number of diameter bins (`num_points`), control the numerical discretization of the DSD and particles sizes used in the T-matrix calculations. The chosen axis-ratio model specifies how drop oblateness increases with diameter, while the canting-angle Gaussian distribution sets the spread of drop orientations around the vertical; this orientation variability directly affects polarimetric variables such as ZDR, LDR, and RHOHV by modulating the effective asymmetry and depolarization of the scattering (Fig. E2b). The water permittivity model and water temperature, together with the radar frequency, determine the complex refractive index of water and the corresponding radar dielectric factor (Fig. E2c). `disdrodb` includes the formulations of Liebe et al. (1991), Ellison (2007) and Turner et al. (2016). These dielectric properties, which are significantly affected by the temperature of the hydrometeors, primarily influence the magnitude of scattering and absorption and therefore directly affect reflectivity and attenuation-related variables (DBZH, DBZV, ZDR, AH, AV, ADP) as well as phase-based quantities such as KDP and PHIDP.

650 The modular design of `disdrodb` further allows the integration of alternative electromagnetic scattering models (e.g. Mie theory, or scattering databases based on Discrete Dipole Approximation (DDA) or Rayleigh-Gans approximations), enabling radar-variable simulations for a broader range of hydrometeor types. The simulation of Doppler spectra is not currently implemented but may be incorporated in future developments. Within the current implementation, the `disdrodb.pytmatrix` wrapper allows users to easily explore how simulation settings influence radar observables and assess their sensitivity to different parameters. As an example of the impact and sensitivity of simulation settings on radar observables, Figure E2 illustrates the impact of water temperature, canting angle spread, and radar viewing geometry on DBZH and ZDR at C band.

7 Conclusions

660 This article presents DISDRODB and the open-source Python package `disdrodb`, a community framework designed to improve the accessibility, standardization, and reproducibility of disdrometer data analysis. The work addresses three persistent limitations in disdrometer-based research: the scarcity of easily usable public datasets, the heterogeneity of raw data formats



and instrument-specific outputs, and the lack of transparent, maintainable processing workflows that can be consistently applied across stations and sensor types.

DISDRODB combines a centralized metadata archive with a decentralized data-sharing model, allowing institutions to retain control and authorship of their raw data while making datasets globally discoverable and straightforward to access and download through a common interface. This architecture lowers the barrier to contribution, respects institutional data-governance constraints, and provides a scalable foundation for long-term community growth.

The `disdrodb` software implements a modular three-level processing chain that converts heterogeneous raw disdrometer measurements into harmonized, analysis-ready products. The L0 processing chain standardizes raw records into `netCDF4` files. The L1 processing chain performs temporal resampling, quality control, and hydrometeor/precipitation-type classification based on raw size–velocity spectra. In contrast to proprietary firmware-based algorithms, the hydrometeor-classification approach implemented in `disdrodb` is transparent, altitude-aware, and reproducible; it can be applied consistently across stations and sensor types, and can be inspected, tested, and improved by the community. The L2 processing chains derive PSD integral parameters, fit parametric PSD models, and simulate radar variables through T-matrix scattering calculations, which substantially expands the value of disdrometer observations for radar and remote-sensing applications. Summary figures and tables can be automatically generated after L2 processing to support rapid exploratory analysis and station-level problem identification.

By providing a transparent and reproducible workflow from raw data to derived products, the software removes much of the time researchers currently spend on data wrangling, format harmonization, and re-implementing instrument-specific processing steps, allowing them to focus on scientific analysis and on identifying methodological improvements. The software also supports flexible execution modes (single-process, parallel, and distributed), enabling efficient processing of large numbers of stations and long time series, on both small computing environments and large clusters. Finally, its modular architecture facilitates future extensions, including ingestion of new sensors, processing methods, quality-control procedures, and derived products contributed by the community.

At the same time, DISDRODB does not remove the intrinsic limitations of disdrometer measurements. Instrument-specific biases, wind effects, sampling uncertainty, proprietary undisclosed on-board particle filtering, and uncertainties in the characterization of frozen and mixed-phase hydrometeors remain important challenges. However, DISDRODB provides a common framework to document, compare, and analyze them systematically across sensors and sites. This is an essential step toward improved disdrometer intercomparison, uncertainty characterization, and evidence-based instrument development.

The current L2 processing chains focus on rainfall, where particle microphysics and electromagnetic scattering assumptions are comparatively well constrained. Future developments could target improved treatment of frozen and mixed-phase precipitation, further refinement and validation of the hydrometeor-classification module against independent observations, and expansion of derived products and radar retrieval-oriented tools. The software design also supports the integration of additional sensors, processing methods, and scattering models as the field evolves.

We look forward to the participation of new institutions in the DISDRODB initiative, both through the contribution of new disdrometer stations and through community-driven development of the open-source software. The progressive consolidation



of a public, global, and homogeneous database of disdrometer measurements will advance our understanding of rainfall characteristics and variability across climates and regions, and will foster new applications in precipitation microphysics, remote sensing, and related fields.

700 *Code and data availability.* The open-source Python package `disdrodb` is available at <https://github.com/ltelab/disdrodb> and can be installed via both `pip` and `conda`. Archived versions of the software are hosted on Zenodo at <https://doi.org/10.5281/zenodo.7680581> (Ghiggi et al., 2026). The DISDRODB metadata archive is maintained at <https://github.com/ltelab/disdrodb-metadata>. Comprehensive documentation, including the API reference and tutorials, is available at <https://disdrodb.readthedocs.io/en/latest/>. The code used to generate the figures presented in this manuscript is available at <https://github.com/ghiggi/disdrodb-amt>. All data used in this study can be accessed through the DISDRODB Decentralized Data Archive.



705 Appendix A: Drop axis ratio models

The deformation of falling raindrops from a perfect sphere into an oblate shape under aerodynamic forces is commonly characterized by the axis ratio $a_r = \frac{B}{A}$ where A and B denote the major (horizontal) and minor (vertical) axes (Szakáll et al., 2010; Beard et al., 2010). The drop size is expressed through the equivolumetric spherical diameter D (also commonly denoted as D_{eq}), defined as the diameter of a sphere having the same volume as the oblate spheroid. The spheroid volume is defined as

$$710 \quad V = \frac{4}{3}\pi \left(\frac{A}{2}\right)^2 \left(\frac{B}{2}\right) = \frac{4}{3}\pi \left(\frac{D}{2}\right)^3.$$

From this relationship it follows that $D = A a_r^{1/3} = B a_r^{-2/3}$. Values of $a_r = 1$ correspond to spherical drops, $a_r < 1$ to oblate drops, and $a_r > 1$ to prolate drops. This parameterization enables the use of an equivalent oblate spheroid in radar scattering simulations, where drop nonsphericity strongly influences electromagnetic scattering and wave propagation, particularly the differential reflectivity (ZDR) and the specific differential phase (KDP).

715

Table A1 summarizes the axis-ratio parameterizations implemented in `disdrodb`, and Fig.A1 illustrates drop axis-ratio values as a function of the equivolumetric spherical diameter D . For PARSIVEL and PARSIVEL2 disdrometers, which report D after assuming the PARSIVEL axis-ratio model $a_{r,P}$ (Battaglia et al., 2010), the horizontal drop semiaxis A can be reconstructed as $A = \frac{D}{a_{r,P}(D)^{1/3}}$. Given the measured horizontal drop size A and an assumed axis ratio model, the corresponding equivolumetric spherical diameter D is obtained by solving $D = \arg \min_{D' > 0} |A a_r(D')^{1/3} - D'|$.

720

Sensitivity analyses indicate that using any of the available axis-ratio models results in relative rainfall-rate differences of less than 2%. However, the choice of axis-ratio model can have a pronounced effect on polarimetric radar variables such as differential reflectivity (see Fig. E2b).

Because the internal processing algorithms of most disdrometers included in `disdrodb` are not fully documented — with the partial exception of PARSIVEL sensors, `disdrodb` currently assumes that the measured and reported particle size correspond to the equivolumetric spherical drop diameter D , rather than the horizontal particle size A . If this assumption is violated, all bulk DSD quantities and simulated radar variables tend to be systematically overestimated. This arises from a size overestimation for larger drops (since $A > D$) caused by their increasing departure from sphericity (see Fig.A1). A bias analysis showed that the resulting overestimation leads to a positive bias in rainfall rate that grows with intensity, exceeding 15 % for rates above 50 mm h⁻¹.

730

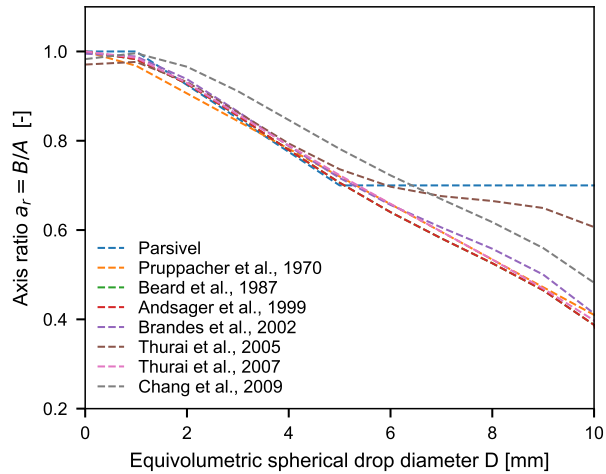


Figure A1. Comparison of drop axis ratio as function of drop diameter for parametrizations implemented in `disdrodb`.

Table A1. Summary of axis–ratio relationships for raindrops. Equivolumetric spherical drop diameter D is in mm.

Name	Formula	Reference
Pruppacher1970	$a_r = 1.03 - 0.062 D$	Pruppacher and Pitter (1971)
Beard1987	$a_r = 1.0048 + 5.7 \times 10^{-4} D - 2.628 \times 10^{-2} D^2 + 3.682 \times 10^{-3} D^3 - 1.677 \times 10^{-4} D^4$	Beard and Chuang (1987)
Andsager1999	$a_r = \begin{cases} 1.012 - 0.0144D - 0.0103D^2 & 1.1 \leq D < 4.4 \\ a_{r, \text{Beard1987}} & \text{otherwise} \end{cases}$	Andsager et al. (1999)
Brandes2002	$a_r = 0.9951 + 0.0251 D - 0.03644 D^2 + 0.005303 D^3 - 0.0002492 D^4$	Brandes et al. (2002)
Thurai2005	$a_r = 0.9707 + 0.0426 D - 0.0429 D^2 + 0.0065 D^3 - 0.0003 D^4$	Thurai and Bringi (2005)
Thurai2007	$a_r = \begin{cases} 1.0 & D < 0.7 \\ 1.173 - 0.5165 D + 0.4698 D^2 - 0.1317 D^3 - 0.0085 D^4 & 0.7 \leq D < 1.5 \\ 1.065 - 0.0625 D - 0.00399 D^2 + 7.66 \times 10^{-4} D^3 - 4.095 \times 10^{-5} D^4 & D \geq 1.5 \end{cases}$	Thurai et al. (2007)
Chang2009	$a_r = 0.98287 + 4.2514 \times 10^{-2} D - 3.3439 \times 10^{-2} D^2 + 4.3402 \times 10^{-3} D^3 - 1.9223 \times 10^{-4} D^4$	Chang et al. (2009)
PARSIVEL	$a_r = \begin{cases} 1.0, & D \leq 1 \text{ mm}, \\ 1.075 - 0.075 D, & 1 < D < 5 \text{ mm}, \\ 0.7, & D \geq 5 \text{ mm}, \end{cases}$	Battaglia et al. (2010)



Appendix B: Terminal fall velocity models

The terminal fall velocity is defined as the velocity that a particle can attain when falling through still air when the sum of the drag force and the buoyancy force is equal to the downward force of gravity. In this appendix we provide a description of rainfall, graupel and hail fall velocity models implemented in the `disdrodb` software. The modular structure of the software also allows new models to be incorporated readily as improved or revised parameterizations become available.

Table B1. Summary of fall-velocity models for rain, graupel, and hail implemented in `disdrodb`. Diameter D in mm; for rain, D denotes the equivolume diameter, whereas for graupel and hail, D refers to the maximum particle size.

Name	Formula	Reference
Rain		
Atlas1973	$V(D) = 9.65 - 10.3e^{-0.6D}$	Atlas et al. (1973)
Beard1976	See Appendix B1.1	Beard (1976)
Uplinger1981	$V(D) = 4.874De^{-0.195D}$	Uplinger (1981)
Lhermitte1988	$V(D) = 9.25 - 9.25e^{-0.068D^2 - 0.488D}$	Lhermitte (1988)
Brandes2002	$V(D) = -0.1021 + 4.932D - 0.9551D^2 + 0.07934D^3 - 0.002362D^4$	Brandes et al. (2002)
VanDijk2002	$V(D) = -0.254 + 5.03D - 0.912D^2 + 0.0561D^3$	van Dijk et al. (2002)
Graupel		
Locatelli1974Lump	$V(D) = 1.3D^{0.66}$	Locatelli and Hobbs (1974)
Locatelli1974Conical	$V(D) = 1.20D^{0.65}$	Locatelli and Hobbs (1974)
Locatelli1974Hexagonal	$V(D) = 1.10D^{0.57}$	Locatelli and Hobbs (1974)
Heymsfield2014	$V(D) = 4.88(0.1D)^{0.84}$	Heymsfield et al. (2014)
Lee2015	$V(D) = 1.10D^{0.28}$	Lee et al. (2015)
Heymsfield2018	$V(D) = 7.59(0.1D)^{0.89}$	Heymsfield et al. (2018, 2020)
Hail		
Laurie1960	$V(D) = 13.95(0.1D)^{0.51}$	Laurie (1960)
Knight1983LD	$V(D) = 8.445(0.1D)^{0.553}$	Knight (1983)
Knight1983HD	$V(D) = 10.58(0.1D)^{0.267}$	Knight (1983)
Heymsfield2014	$V(D) = 12.28(0.1D)^{0.57}$	Heymsfield et al. (2014)
Heymsfield2018	$V(D) = 8.39(0.1D)^{0.67}$	Heymsfield et al. (2018, 2020)
Fehlmann2020	$V(D) = 3.74D^{0.5}$	Fehlmann et al. (2020)

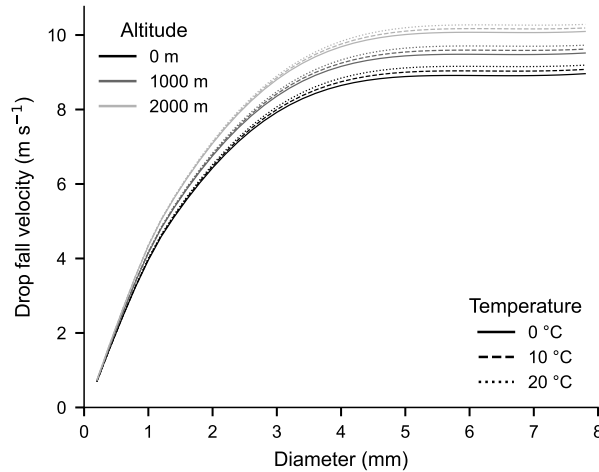


Figure B1. Rain drop fall velocity as function of drop diameter, altitude and temperature estimated using the Beard terminal fall velocity model.

B1 Raindrop terminal fall velocity

Raindrop fall velocities can be estimated using empirical relationships derived from field and laboratory measurements. Table B1 summarizes the relationships included in disdrodb, while Figure B1 illustrates the dependence of rain drop terminal fall velocity on drop diameter and air density. Terminal velocity increases primarily with drop diameter, but tends to level off at diameters near 5 mm. For a given diameter, it increases with decreasing air density, and is therefore greater at higher altitudes and under warmer atmospheric conditions.

To account for changes in air density with altitude, disdrodb applies the correction proposed by Beard (1985):

$$v_h(D) = v_0(D) \left(\frac{\rho_0}{\rho_h} \right)^{(0.375+0.025D)}$$

where D is the diameter of the drop (mm), and ρ_0 and ρ_h are the air densities at sea level and height h , respectively. ρ_0 is set to 1.225 kg m^{-3} assuming an International Standard Atmosphere. The air density ρ_h is computed following Brutsaert (1982):

$$\rho_h = \frac{p}{R_d T} \left(1 - 0.378 \frac{e}{p} \right)$$

where T is the air temperature (K), p the air pressure (Pa), e the actual vapor pressure (Pa), and R_d the gas constant for dry air with a default value of $287.04 \text{ J kg}^{-1} \text{ K}^{-1}$. The actual vapor pressure is calculated as $e = \text{RH} \times e_{\text{sat}}(T)$ where RH is the relative humidity (0-1) and $e_{\text{sat}}(T)$ is the saturation vapor pressure (in Pascals) at temperature T , obtained using the formulation of Flatau et al. (1992).



B1.1 Beard terminal fall velocity model

The Beard (1976) model provides a physically based description of raindrop terminal velocity by accounting for the effects of drop shape, drag, and air properties across a wide range of drop sizes. The terminal velocity is expressed in terms of the Reynolds number by rearranging its definition

$$755 \quad V(D) = \frac{\eta_a \text{Re}(D)}{\rho_a D} \quad (\text{B1})$$

where η_a is the dynamic viscosity of air ($\text{kg m}^{-1} \text{s}^{-1}$), ρ_a is the air density (kg m^{-3}), and $\text{Re}(D)$ is the Reynolds number of the drop.

The Reynolds number is defined piecewise, with separate formulations for small and large drops:

$$760 \quad \text{Re}(D) = \begin{cases} \text{Re}_{\text{small}}(D), & D < 1.07 \text{ mm} \\ \text{Re}_{\text{large}}(D), & D \geq 1.07 \text{ mm} \end{cases}$$

For small drops ($D < 1.07 \text{ mm}$), the Davies number is computed as $\text{Da} = \frac{4\rho_w(\rho_w - \rho_a)gD^3}{3\eta_a^2}$, where ρ_w is the water density (kg m^{-3}) and g the gravitational acceleration (m s^{-2}). The corresponding Reynolds number is obtained from an exponential of a sixth-order polynomial with $x = \ln(\text{Da})$:

$$\text{Re}_{\text{small}}(D) = \exp\left(\sum_{i=0}^6 b_i x^i\right)$$

765 For larger drops ($D \geq 1.07 \text{ mm}$), the Bond number $\text{Bo} = \frac{4(\rho_w - \rho_a)gD^2}{3\sigma}$ and the property number $\text{P} = \frac{\sigma^3 \rho_a^2}{\eta_a^4(\rho_w - \rho_a)g}$ are first computed. The surface tension of pure water σ (N m^{-1}) is derived following Pruppacher and Klett (1978) parametrization:

$$\sigma(T) = 0.0761 - 0.000155T \quad \text{with } T \text{ in } ^\circ\text{C}.$$

With $x = \ln(\text{Bo}) + \frac{\ln(\text{P})}{6}$, the Reynolds number for large drops is then estimated as an exponential of a fifth-order polynomial:

$$\text{Re}_{\text{large}}(D) = \exp\left(\frac{\ln(\text{P})}{6} + \sum_{i=0}^5 c_i x^i\right)$$

770 The dynamic viscosity of air, required in the above expressions is computed following Beard (1976) as:

$$\eta_a(T) = \begin{cases} \frac{1.721 + 0.00487T}{10^5}, & T > 0, \\ \frac{1.718 + 0.0049T - 1.2T^2/10^5}{10^5}, & T \leq 0, \end{cases} \quad \text{with } T \text{ in } ^\circ\text{C}.$$

The coefficients used in the above polynomial expressions are listed in Table B2.



Table B2. Polynomial coefficients for the Reynolds number parameterizations of Beard (1976). Coefficients b_i apply to small drops ($D < 1.07$ mm) and c_i to large drops ($D \geq 1.07$ mm).

Order	b_i (small drops)	c_i (large drops)
0	-3.18657	-5.00015
1	0.992696	5.23778
2	-0.00153193	-2.04914
3	-0.000987059	0.475294
4	-0.000578878	-0.0542819
5	0.0000855176	0.00238449
6	-0.00000327815	—

B2 Graupel fall velocity models

775 Graupel fall velocities can be estimated using empirical relationships derived from field and laboratory measurements. Table B1 summarizes the graupel parametrizations included in disdrodb. To account for the decrease of air density with altitude, disdrodb applies the correction proposed by Heymsfield et al., 2014:

$$V_h(D) = V_0(D) \left(\frac{101325}{p} \right)^{0.545} \quad (\text{B2})$$

where D is the particle's maximum diameter (mm), and p_0 and p_h are the air pressures at sea level and at height h , respectively. p_0 is set to 101325 Pa, consistent with the International Standard Atmosphere.

780

disdrodb also includes the graupel fall velocity model described in Heymsfield and Wright (2014), which provides empirical relationships for estimating the particle Reynolds number from its size (D), its bulk density (ρ_b), air density (ρ_a), and air dynamic viscosity (η_a), thereby enabling computation of the terminal fall velocity (see Eq. (B1)). The Reynolds number is defined piecewise for two regimes:

$$785 \quad Re = \begin{cases} 0.106 X^{0.693}, & X < 6.77 \times 10^4 \\ 0.55 X^{0.545}, & X \geq 6.77 \times 10^4 \end{cases}$$

with the Best number X defined as $X = \frac{4}{3} D^3 \rho_b g \rho_a / \eta_a^2$.

B3 Hail fall velocity models

Hail fall velocities are parametrized with the equations summarized in Table B1. The same correction factor as for graupel particles (see Eq. (B2)) is applied to account for the air density decrease with altitude.



790 Appendix C: DSD integral parameters

The drop size distribution (DSD) is fully described by the number drop concentration $N(D)$, which specifies the number of drops per unit volume and per unit diameter interval. In practice, disdrometers estimate $N(D)$ from the observed drop count $n(D)$ in each diameter bin. This conversion requires knowledge of the drop fall velocity $v(D)$ (in m s^{-1}), the instrument's sampling area A (in m^2), the diameter bin width ΔD (in mm), and the sampling interval Δt (in s):

$$795 \quad N(D) = \frac{n(D)}{v(D)A\Delta D\Delta t} \quad [\text{m}^{-3}\text{mm}^{-1}] \quad (\text{C1})$$

For optical extinction-based disdrometers that remove margin fallers (such as the PARSIVEL and PARSIVEL2), the sampling area must be adapted to account for dropout at the beam edges. This effective area is defined as the region in which a drop is fully detected, and therefore counted, using $A(D) = L(W - D)$, where L and W denote the sensor length and width respectively. Neglecting this correction (or incorrectly using $W - D/2$ instead of $W - D$), leads to an underestimation of $N(D)$

800 and derived bulk quantities, including rainfall rate.

For disdrometers measuring fall velocity directly, $N(D)$ can be computed using either theoretical terminal velocities or the measured fall velocities. The DISDRODB L2E product provides both $N(D)$ definitions, stored along the `velocity_method` dimension.

805 Bulk DSD parameters are obtained from the moments of $N(D)$. In the following equations, D is assumed to be in meters. The n -th moment M_n of the DSD is defined as:

$$M_n = \int_0^{\infty} N(D) \left(\frac{D}{1000} \right)^n dD \quad [\text{mm}^n \text{m}^{-3}] \quad (\text{C2})$$

The n -th moment M_n weights each diameter by D^n , emphasizing different physical properties: the zeroth moment corresponds to drop concentration, the third to mass, and the sixth to radar reflectivity (in the Rayleigh scattering regime). Integrating $N(D)$

810 over all diameters yields the total drop number concentration N_t , underscoring that $N(D)$ is not a probability distribution as its integral is not equal to one:

$$N_t = \int_0^{\infty} N(D) dD = M_0 \quad [\text{m}^{-3}] \quad (\text{C3})$$

The volume and mass of a spherical drop scale with D^3 , allowing the drop mass distribution $m(D)$ to be expressed directly in

815 terms of $N(D)$:

$$V_{drop}(D) = \frac{4}{3}\pi \left(\frac{D}{2} \right)^3 = \frac{\pi}{6} D^3 \quad [\text{m}^3]$$

$$M_{drop}(D) = \rho_w V_{drop} = \frac{\pi\rho_w}{6} D^3 \quad [\text{g}]$$



$$820 \quad m(D) = N(D)M_{drop}(D) = \frac{\pi\rho_w}{6}N(D)D^3 \quad [\text{g m}^{-3} \text{ mm}^{-1}] \quad (\text{C4})$$

with ρ_w , the drop water density, typically taken as $\rho_w = 10^6 \text{ g m}^{-3}$.

Integrating $m(D)$ over all diameters yields the liquid water content (LWC), which represents the mass of liquid water per unit volume of air:

$$\text{LWC} = \int_0^\infty m(D) dD = \frac{\pi\rho_w}{6} \int_0^\infty N(D) D^3 dD = \frac{\pi\rho_w}{6 \cdot 10^9} M_3 \quad [\text{g m}^{-3}] \quad (\text{C5})$$

825 Under Rayleigh scattering conditions, when particles size is much smaller than the radar wavelength λ , the radar reflectivity z reduces to the sixth moment of the DSD. The corresponding logarithmic reflectivity Z (commonly referred to as reflectivity factor) is the standard variable reported by weather radars:

$$z = \frac{\lambda^4}{\pi^5 |K_w|^2} \int_0^\infty N(D) \sigma_b(D) dD \approx \int_0^\infty N(D) \left(\frac{D}{1000} \right)^6 dD = M_6 \quad [\text{mm}^6 \text{ m}^{-3}]$$

$$830 \quad Z = 10 \log_{10}(z) \quad [\text{dBZ}] \quad (\text{C6})$$

The definitions of the backscattering cross-section $\sigma_b(D)$ and the squared dielectric factor $|K_w|^2$ are given in Eq. (E1) and (E4) of Appendix E respectively.

Rainfall rate can be derived either from the measured drop counts $n(D)$ or from the estimated number concentration $N(D)$:

$$835 \quad R_m = \frac{\pi}{6} (3600 \times 1000) \sum_i n(D_i) \frac{D_i^3}{A \Delta t} \quad [\text{mm h}^{-1}]$$

$$R = \frac{\pi}{6} (3600 \times 1000) \int N(D) v(D) D^3 dD \quad [\text{mm h}^{-1}] \quad (\text{C7})$$

where the factor 3600×1000 converts the rain rate from m s^{-1} to mm h^{-1} . Note that the formulation based on $n(D)$ does not rely on assumptions about fall velocity. The corresponding rain accumulation P over the measurement interval Δt is given by:

$$840 \quad P = \frac{R \Delta t}{3600} \quad [\text{mm}] \quad (\text{C8})$$

Rainfall kinetic energy descriptors can also be derived using either $n(D)$ or $N(D)$. When measured velocities are available, they can be used directly in the $n(D)$ formulation; otherwise, a terminal fall velocity parameterization is necessary. The kinetic energy of a single raindrop is defined as:

$$\text{KE}_{drop}(D) = \frac{1}{2} M_{drop}(D) v^2 = \frac{\pi\rho_w}{12} D^3 v^2.$$

845 The total kinetic energy (TKE) accumulated over the sampling period Δt can be obtained with:

$$\text{TKE} = \sum_i \frac{n(D_i) \text{KE}_{drop}(D_i)}{A} = \int_0^\infty N(D) \text{KE}_{drop}(D) v(D) \Delta t dD = \frac{\pi\rho_w}{12} \int_0^\infty N(D) D^3 v(D)^3 \Delta t dD \quad [\text{J m}^{-2}] \quad (\text{C9})$$



The kinetic energy flux (KEF) represents the rate at which kinetic energy is delivered to the surface. It is obtained by normalising TKE by the sampling interval and converting to hourly units:

$$\text{KEF} = \frac{\text{TKE}}{\Delta t} 3600 \quad [\text{J m}^{-2} \text{h}^{-1}] \quad (\text{C10})$$

850 Finally the kinetic energy per rainfall depth (*KED*) normalises the energy flux by the corresponding rain rate *R*:

$$\text{KED} = \frac{\text{KEF}}{R} \quad [\text{J m}^{-2} \text{mm}^{-1}] \quad (\text{C11})$$

These three variables are widely used to characterise rainfall erosivity (Petan et al., 2010; Angulo-Martínez et al., 2016; Tilg et al., 2020; Serio et al., 2019; Johannsen et al., 2020).

855 Beyond integrated quantities, several parameters describe the breadth or shape of the DSD. The median volume diameter, D_{50} (also commonly denoted D_0), is defined as the diameter at which half the LWC is contained in smaller drops:

$$\frac{\pi}{6} \rho_w \int_0^{D_{50}} N(D) D^3 dD = \int_0^{D_{50}} m(D) dD = \frac{1}{2} \text{LWC}. \quad (\text{C12})$$

More generally, the percentile volume diameter D_p partitions the LWC into a fraction $p/100$ below and above that diameter:

$$\frac{\pi}{6} \rho_w \int_0^{D_p} N(D) D^3 dD = \int_0^{D_p} m(D) dD = \frac{p}{100} \text{LWC}.$$

860 Although conceptually intuitive, these percentile diameters require solving implicit integral equations. For computational efficiency and easier theoretical calculations, the mass-weighted mean diameter (D_m) is often used as an approximate explicit surrogate for D_{50} . D_m is defined as the first moment of the mass distribution $m(D)$ normalized by the total mass LWC.

$$D_m = \mathbb{E} \left[\frac{m(D)}{\text{LWC}} \right] = \frac{\mathbb{E}[m(D)]}{\text{LWC}} = \frac{\int_0^\infty m(D) D dD}{\int_0^\infty m(D) dD} = \frac{\int_0^\infty N(D) D^4 dD}{\int_0^\infty N(D) D^3 dD} = M_4/M_3 \quad (\text{C13})$$

The width of the mass spectrum is characterized by the variance of $\frac{m(D)}{\text{LWC}}$, which quantifies the spread of mass around D_m :

$$\sigma_m^2 = \text{Var} \left[\frac{m(D)}{\text{LWC}} \right] = \int_0^\infty \left(D - \mathbb{E} \left[\frac{m(D)}{\text{LWC}} \right] \right)^2 \frac{m(D)}{\text{LWC}} dD = \frac{\int_0^\infty (D - D_m)^2 m(D) dD}{\text{LWC}}$$

$$\begin{aligned} &= \frac{\int_0^\infty (D - D_m)^2 N(D) D^3 dD}{\int_0^\infty N(D) D^3 dD} = \frac{M_3 M_5 - M_4^2}{M_3^2}. \end{aligned} \quad (\text{C14})$$

The mass spectrum standard deviation σ_m , together with D_m , are frequently used to characterise the shape of the DSD (Ulbrich, 1983; Smith et al., 2019; Williams et al., 2014; Zhang, 2015). Additional shape parameters can be obtained by fitting parametric DSD models, as described in Appendix D.



Appendix D: DSD Parametric Models

870 DSD parametric models aim to represent the functional shape of the drop size distribution $N(D)$ using analytical expressions. In general, $N(D)$ can be written as $N(D) = N_t \cdot \text{pdf}(D; \theta)$, where N_t controls the overall scaling while the parameters θ determine the shape of the DSD through a chosen probability distribution function (pdf). The following subsections describe the models implemented in `disdrodb`.

D1 Unnormalized DSD models

875 The Lognormal DSD model (Feingold and Levin, 1986; Maitra and Gibbins, 1999) is defined as

$$N(D; N_t, \mu, \sigma) = \frac{N_t}{\sqrt{2\pi} \sigma D} \exp\left[-\frac{(\ln D - \mu)^2}{2\sigma^2}\right] \quad (\text{D1})$$

The Generalized Gamma DSD model (Stacy, 1962; Maur, 2001; Lee et al., 2004) is given by:

$$N(D; N_t, \Lambda, \mu, c) = N_t \frac{c \Lambda}{\Gamma(\mu + 1)} (\Lambda D)^{c(\mu+1)-1} \exp[-(\Lambda D)^c] \quad \text{with } \mu > -1, c > 0, \Lambda > 0. \quad (\text{D2})$$

Setting $c = 1$ yields the classical three-parameter Gamma DSD model (Ulbrich, 1983):

880
$$N(D; N_0, \Lambda, \mu) = N_t \frac{\Lambda^{\mu+1}}{\Gamma(\mu+1)} D^\mu e^{-\Lambda D} = N_0 D^\mu e^{-\Lambda D}, \quad \text{with } N_0 = \frac{N_t \Lambda^{\mu+1}}{\Gamma(\mu+1)} \quad (\text{D3})$$

Parameters N_0 (with units $\text{mm}^{-(\mu+1)} \text{m}^{-3}$), Λ (mm^{-1}), and μ (dimensionless) are commonly referred to as the scale, slope, and shape parameters, respectively. However, the classical formulation of the Gamma DSD has the drawback that the units of N_0 depend on the value of μ and Λ , which can introduce interpretational ambiguities and potentially lead to spurious correlations. For this reason, an alternative parameterization of the Gamma DSD (e.g., based on N_t) is adopted in `disdrodb`,
885 and N_0 is calculated a posteriori. Constrained Gamma models, in which μ and Λ are linked through an empirical μ - Λ relation, reduce the number of free parameters from three to two (Zhang et al., 2001, 2003; Cao and Zhang, 2009; Williams et al., 2014; Gatidis et al., 2022, 2024).

Further setting $c = 1$ and $\mu = 0$ gives the two-parameter Exponential DSD model (Marshall and Palmer 1948)

$$N(D; N_0, \Lambda) = N_t \Lambda e^{-\Lambda D} = N_0 e^{-\Lambda D}, \quad \text{with } N_0 = N_t \Lambda \quad \text{and units } [\text{mm}^{-1} \text{m}^{-3}] \quad (\text{D4})$$

890 where N_0 has units ($\text{mm}^{-1} \text{m}^{-3}$) and Λ (mm^{-1}).

D2 Normalized DSD models

In these traditional unnormalized DSD formulations, model parameters are not independent and do not correspond directly to physical quantities. For example, in the Gamma DSD model, the parameters μ and N_0 are strongly correlated, leading to physical inconsistencies and unstable parameters estimates. To address these issues, Willis (1984); Testud et al. (2001); Illingworth and Blackman (2002) introduced Normalized Gamma (NG) DSD models. These formulations replace the scale (N_0) and
895 slope (Λ) with physically meaningful bulk quantities such as D_m and either LWC or N_t . In normalized DSD formulations, the



intrinsic shape of the distribution is determined solely by the shape parameter μ , while the remaining free parameters relate to measurable physical quantities:

$$N(D; N_w, D_{50}, \mu) = N_w f(\mu) \left(\frac{D}{D_{50}} \right)^\mu \exp\left(-(\mu + 3.67) \frac{D}{D_{50}}\right), f(\mu) = \frac{\Gamma(4)}{3.67^4} \frac{(\mu + 3.67)^{\mu+4}}{\Gamma(\mu + 4)}$$

$$N(D; N_w, D_m, \mu) = N_w f_1(\mu) \left(\frac{D}{D_m} \right)^\mu \exp\left(-(\mu + 4) \frac{D}{D_m}\right), f_1(\mu) = \frac{\Gamma(4)}{4^4} \frac{(\mu + 4)^{\mu+4}}{\Gamma(\mu + 4)}. \quad (D5)$$

$$N(D; N_t, D_m, \mu) = \frac{N_t}{D_m} f_2(\mu) \left(\frac{D}{D_m} \right)^\mu \exp\left(-(\mu + 4) \frac{D}{D_m}\right), f_2(\mu) = \frac{(\mu + 4)^{\mu+1}}{\Gamma(\mu + 1)} \quad (D6)$$

We note here that slight variations of these formulations have been proposed by Gorgucci et al. (2002) by replacing D_m with D_{50} , using the approximate relationship between the two characteristic diameters (Ulbrich, 1983):

$$D_m = \frac{\mu + 4}{\mu + 3.67} D_{50}.$$

The normalized intercept parameter N_w depends on LWC and D_m :

$$N_w = \frac{4^4}{\pi \rho_w} \frac{\text{LWC}}{D_m^4} = \frac{4^4}{6} M_3^5 / M_4^4 \quad \text{with units} \quad [\text{mm}^{-1} \text{m}^{-3}] \quad (D7)$$

For $\mu = 0$, N_w equals the intercept parameter N_0 of the traditional Exponential DSD model.

910 D3 Double moment normalization

Seeking a more flexible analytical form capable of representing diverse intrinsic DSD shapes, Lee et al. (2004) introduced the double-moment normalization approach. In this formulation $N(D) = N_c \cdot \text{pdf}(\frac{D}{D_c}; \theta)$ where D_c refers to the general characteristic diameter size and N_c to the general characteristic intercept. These quantities can be defined using two arbitrary moments, M_i and M_j , of the DSD:

$$D_c = M_i^{\frac{1}{j-i}} M_j^{\frac{-1}{j-i}}, = \left(\frac{M_j}{M_i} \right)^{\frac{1}{j-i}} \quad \text{with units} \quad [\text{mm}] \quad (D8)$$

$$N_c = M_i^{\frac{j+1}{j-i}} M_j^{\frac{i+1}{i-j}} \quad \text{with units} \quad [\text{mm}^{-1} \text{m}^{-3}] \quad (D9)$$

The double-moment normalization approach does not prescribe any specific pdf to represent the intrinsic DSD shape. When a Generalized Gamma pdf is adopted, the resulting Normalized Generalized Gamma (NGG) DSD model becomes:

$$N(D; N_c, D_c, \mu, c, i, j) = N_c c \Gamma_i^{\frac{j+c(\mu+1)}{i-j}} \Gamma_j^{\frac{-i-c(\mu+1)}{i-j}} \left(\frac{D}{D_c} \right)^{c(\mu+1)-1} \exp\left[-\left(\frac{\Gamma_i}{\Gamma_j}\right)^{\frac{c}{i-j}} \left(\frac{D}{D_c}\right)^c\right] \quad (D10)$$

where $\Gamma_i = \Gamma(\mu + 1 + \frac{i}{c})$ and $\Gamma_j = \Gamma(\mu + 1 + \frac{j}{c})$; with N_c and D_c depending on the chosen moments M_i and M_j of the DSD. Setting $c = 1$, $i = 3$, $j = 4$ in the NGG model, yields an expression essentially equivalent to the NG model described in Eq. D5. The NGG DSD model is often constrained to two free parameters, by selecting i , j , c and μ that best represent the normalized DSD shape. The remaining two free parameters N_c and D_c depend solely on the chosen moments M_i and M_j . Figure 9a illustrates the shape of NG and NGG models fitted to observed double normalized DSD data with $i = 3$ and $j = 4$.

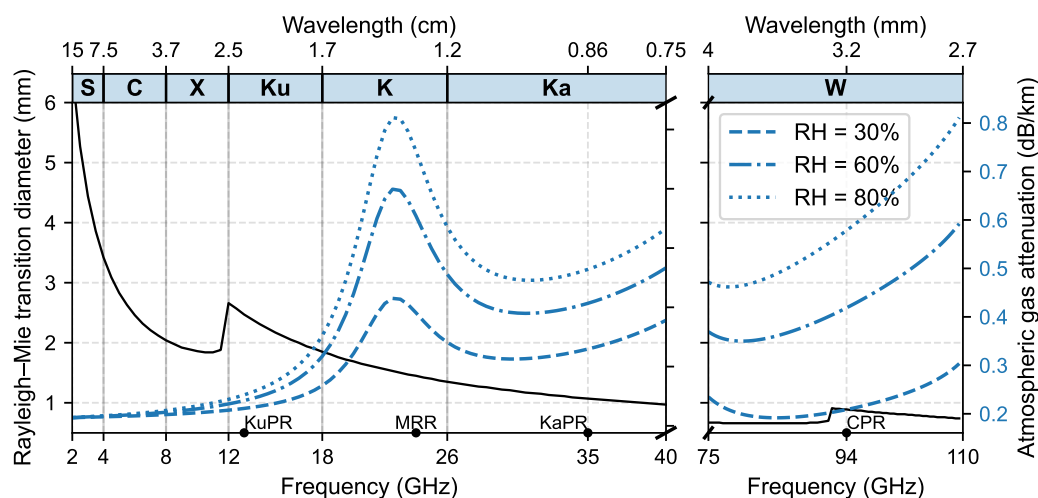


Figure E1. Frequency dependence of the Rayleigh-Mie transition diameter and atmospheric gas attenuation (oxygen and water vapour) across microwave radar bands. The bottom x-axis shows frequency (GHz) and the top axes show the corresponding wavelengths (cm and mm), with S, C, X, Ku, K, Ka, and W bands indicated. The operating frequencies of TRMM and GPM KuPR, MRR, GPM KaPR, and CloudSat and EarthCare CPR radars are annotated. The black solid curve (left y-axis) represents the drop diameter at which scattering transitions from the Rayleigh to the Mie regime. The transition is defined as the diameter at which the pyTmatrix-simulated normalized radar backscattering cross section $\frac{\sigma_b^h(D)}{\pi(D/2)^2}$ deviates by more than 10% from the Rayleigh approximation. The blue dashed, dash-dotted, and dotted curves (right y-axis) show atmospheric gas attenuation (dB km^{-1}) for relative humidity (RH) levels of 30%, 60%, and 80%, respectively. Gaseous attenuation increases with both frequency and humidity, exhibits a pronounced peak near the 22-24 GHz water vapor absorption band, and becomes very strong in the oxygen absorption K region within the V band (40-75 GHz; not shown). Strong gaseous attenuation also occurs at W band frequencies.

Appendix E: Simulation of radar variables

The T-matrix method (Mishchenko et al., 1996; Mishchenko and Travis, 1998; Mishchenko, 2000; Mishchenko et al., 2000) is a high-performance numerical approach for computing electromagnetic scattering by nonspherical particles. It provides accurate results across a broad range of particle sizes and shapes, also in the resonance (Mie) regime, where particle dimensions are comparable to the radar wavelength and scattering involves internal resonances, diffraction, and higher-order multipole interactions. The method has been widely applied at precipitation-radar frequencies (S, C, X, Ku, K and Ka bands) (Ryzhkov et al., 2011; Kalina et al., 2014; Raupach and Berne, 2017; Wolfensberger and Berne, 2018; Teng et al., 2018; van Leth et al., 2020) and also at higher microwave and millimeter-wave bands (Aydin and Lure, 1991; Ekelund et al., 2020; Tsikoudi et al., 2025; Myagkov et al., 2025). Figure E1 illustrates radar frequencies, wavelengths and the transition occurrence from Rayleigh to Mie scattering regime as function of drop diameter.



Raindrops are modeled as oblate spheroids that fall with a preferred orientation, represented by a Gaussian canting-angle distribution centered at zero degree. The standard deviation of this distribution determines the spread of the drop symmetry axis around the vertical, and has been reported to increase in the presence of turbulence and strong winds (Huang et al., 2008; Bolek and Testik, 2022; Zheng et al., 2024).

940

For a given frequency, scattering geometry (radar viewing angle), particle complex refractive index, size, and orientation distribution, the T-matrix method enables the computation of the complex 2x2 scattering amplitude matrix \mathbf{S} for each particle orientation within the specified orientation distribution. \mathbf{S} is defined as

$$\mathbf{S} = \begin{bmatrix} s_{HH} & s_{HV} \\ s_{VH} & s_{VV} \end{bmatrix}$$

945 whose elements are complex quantities with units millimeters (Bringi and Chandrasekar, 2001; Doviak and Zrnić, 1993). The labels H and V refer to horizontal and vertical linear polarizations, respectively. When two polarization subscripts are used, the first letter denotes the transmitted polarization and the second the received polarization. The \mathbf{S} matrix relates the incident and scattered (or reflected) electric fields through:

$$\begin{bmatrix} E_H^{sca} \\ E_V^{sca} \end{bmatrix} = \frac{e^{-ik_0 r}}{r} \mathbf{S} \begin{bmatrix} E_H^{inc} \\ E_V^{inc} \end{bmatrix}$$

950 with $k_0 = \frac{2\pi}{\lambda}$ the angular wavenumber in free-space (rad m^{-1}), and r the distance (in meters) between the scatterer and the observation point in the far field. The amplitude matrix \mathbf{S} can be written in the forward-scattering alignment (FSA) convention, equivalent to the Jones matrix (Jones, 1941), or in the back-scattering alignment (BSA) convention used in monostatic radar. In this appendix, superscripts f and b indicate forward and backward-scattering amplitude coefficients, respectively. Single-particle scattering quantities follow directly from the amplitude-matrix coefficients. The backscattering cross sections
 955 for horizontal and vertical polarization (σ_H^b and σ_V^b , with units mm^2) describe the amount of power reradiated back toward the radar by an individual particle:

$$\begin{bmatrix} \sigma_H^b \\ \sigma_V^b \end{bmatrix} = 4\pi \begin{bmatrix} |s_{HH}^b|^2 \\ |s_{VV}^b|^2 \end{bmatrix} = 4\pi \begin{bmatrix} s_{HH}^b (s_{HH}^b)^* \\ s_{VV}^b (s_{VV}^b)^* \end{bmatrix} \quad (\text{E1})$$

Similarly, the extinction cross section (σ^{ext} , with units mm^2), which quantifies the total removal of energy from the incident wave by scattering and absorption, is obtained from the forward-scattering amplitude coefficients.

960

$$\begin{bmatrix} \sigma_H^{ext} \\ \sigma_V^{ext} \end{bmatrix} = \frac{4\pi}{k_0} \begin{bmatrix} \text{Im}(s_{HH}^f) \\ \text{Im}(s_{VV}^f) \end{bmatrix} = 2\lambda \begin{bmatrix} \text{Im}(s_{HH}^f) \\ \text{Im}(s_{VV}^f) \end{bmatrix},$$

When particles of a given size have random orientations, their scattering properties must be averaged over the orientation distribution. For a single particle orientation, scattering is described by the complex amplitude scattering matrix \mathbf{S} . Because its



elements contain phase information that varies with orientation, the amplitudes themselves cannot be averaged directly: contributions from different orientations may partially cancel even when all particles scatter significant power. Radar observables are instead related to scattered power and polarization, which depend on quadratic products of the scattering amplitudes and their complex conjugates (e.g., $s_{HH}s_{HH}^*$, $s_{VV}s_{VV}^*$, or $s_{HH}s_{VV}^*$). Unlike the complex amplitudes themselves, these quantities remain directly related to the average intensity and polarization of the scattered wave after averaging over the orientation distribution, and are conveniently represented by the Mueller matrix \mathbf{Z} , which relates the incident and scattered Stokes vectors \mathbf{I} as:

$$\mathbf{I}_{\text{sca}} = \frac{1}{r^2} \mathbf{Z} \mathbf{I}_{\text{inc}}$$

In disdrodb, the scattering amplitude matrix \mathbf{S} and Mueller matrix \mathbf{Z} are first computed for each particle orientation and then averaged over the prescribed orientation distribution. The resulting orientation-averaged matrices are precomputed for all particle diameters (defined by the *diameter_min*, *diameter_max* and *num_points* options) and cached to disk so that they can be efficiently reused when computing the radar variables. Radar observables that depend on back-scattered power are derived from the orientation-averaged Mueller matrix \mathbf{Z} . In contrast, forward-scattering quantities are computed from the orientation-averaged amplitude matrix \mathbf{S} , since they depend directly on the complex forward-scattering amplitudes rather than on power-based quantities.

For simplicity, the formulas used in the next section to derive backward-scattering radar variables are written assuming fixed particle orientation. Under this assumption, the expressions can be written directly in terms of the scattering amplitude coefficients, avoiding the the more involved quadratic combinations that arise in the full Mueller-matrix formulation. Interested readers are referred to Mishchenko et al. (2000), Bringi and Chandrasekar (2001) and Ekelund et al. (2020) for more details.

E1 Backward scattering radar variables

The variables a radar would observe at the receiver are derived from the computed backscattering amplitude coefficients evaluated at the monostatic angle $\theta_s = 180^\circ$.

E1.1 Reflectivity

Radar reflectivity represents the backscattered power from the PSD within the sampling volume. The reflectivity factor in linear units (z , expressed in $\text{mm}^6 \text{m}^{-3}$) or in decibels (Z , in dBZ) at horizontal and vertical polarization are given by:

$$z_H = \frac{\lambda^4}{\pi^5 |K_w|^2} \int_{D_{\min}}^{D_{\max}} \sigma_H^b(D) N(D) dD \quad \text{and} \quad Z_H = 10 \log_{10}(z_H) \quad (\text{E2})$$

$$z_V = \frac{\lambda^4}{\pi^5 |K_w|^2} \int_{D_{\min}}^{D_{\max}} \sigma_V^b(D) N(D) dD \quad \text{and} \quad Z_V = 10 \log_{10}(z_V) \quad (\text{E3})$$

with the radar wavelength λ in mm. The squared dielectric factor $|K_w|^2$ of the hydrometeors is defined as

$$|K_w|^2 = \left| \frac{m_w^2 - 1}{m_w^2 + 2} \right|^2 = \left| \frac{\epsilon_w - 1}{\epsilon_w + 2} \right|^2 \quad (\text{E4})$$

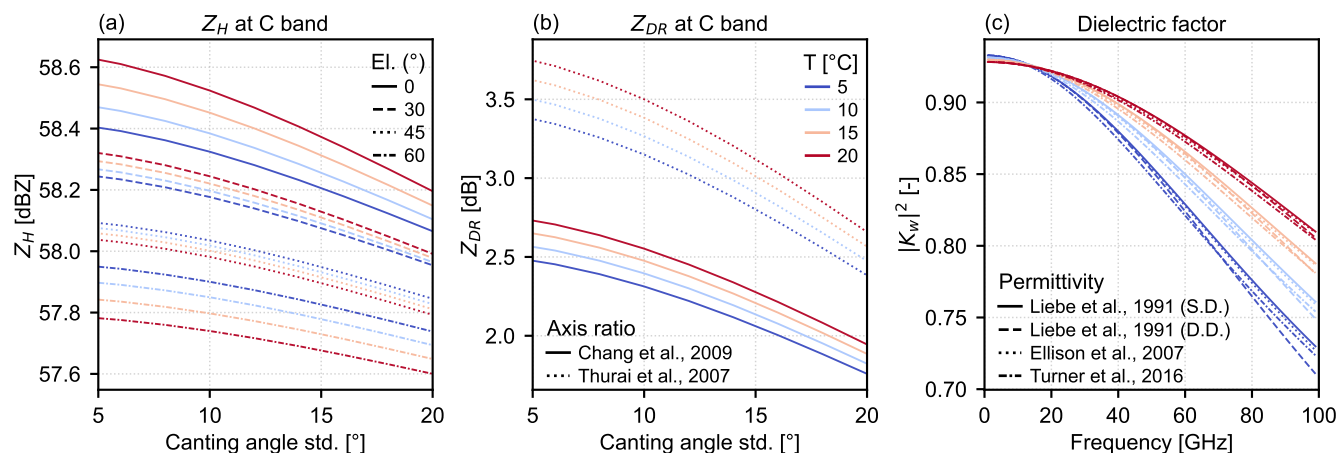


Figure E2. Sensitivity of polarimetric radar variables to particle orientation variability, drop water temperature, and radar scanning geometry, and variability of the dielectric factor with frequency and temperature. The DSD shown in Fig. 8b–c is used for this sensitivity experiment. (a) Simulated horizontal reflectivity Z_H at C band as a function of the standard deviation of a Gaussian canting angle distribution (zero mean), for drop temperatures of 5–20 °C and radar elevation angles of 0°, 30°, 45°, and 60°. Z_H slightly decreases with increasing canting angle spread and elevation angle. In the Rayleigh regime (e.g., S band), the effect of drop temperature on Z is negligible. In the Mie regime (e.g., C band for large drops and X band), temperature-dependent changes in the complex dielectric constant modify the drop backscattering cross section and thus Z , potentially producing nonlinear or non-monotonic behavior. (b) Corresponding differential reflectivity Z_{DR} at C band and 0° elevation as a function of canting angle spread for temperatures of 5–20 °C, using axis-ratio models from Chang et al. (2009) and Thurai et al. (2007). Z_{DR} decreases with increasing canting angle variability because greater orientation randomness reduces the difference between horizontally and vertically polarized backscatter. Z_{DR} also decreases with increasing radar elevation angle (not shown) as the viewing geometry becomes less sensitive to the horizontal oblateness of raindrops. (c) Magnitude of the dielectric factor $|K_w|^2$ for liquid water as a function of frequency (0–100 GHz) and temperature, computed using permittivity models from Liebe et al. (1991); Single- and Double-Debye, Ellison (2007), and Turner et al. (2016).

where m_w and ϵ_w are, respectively, the complex refractive index and relative permittivity of water relative to air, computed from any of the following models implemented in disdrodb: the single-Debye model (Liebe et al., 1991), the double-Debye model (Liebe et al., 1991), the Ellison model (Ellison, 2007), and the Turner-Kneifel-Cadeddu (TKC) model for supercooled liquid water (Turner et al., 2016). Figure E2c illustrates how $|K_w|^2$ varies as a function of frequency and water temperature.

995 While Z_H is mainly influenced by the drop size distribution (DSD), it decreases slightly with increasing radar elevation angle as the beam becomes more aligned with the symmetry axis of oblate hydrometeors, reducing their horizontally projected cross-section. Increasing canting angle spread (e.g., in turbulent conditions) can also slightly reduce Z_H because more random particle orientations decrease the effective horizontally projected area contributing to horizontally polarized backscatter (see Fig. E2a).



1000 E1.2 Differential reflectivity

Differential reflectivity (Z_{DR}) quantifies the difference in polarized H and V reflectivities and provides information about particle shape and orientation:

$$Z_{DR} = 10 \log_{10} \left(\frac{z_H}{z_V} \right) = Z_H - Z_V \text{ [dB]} \quad (\text{E5})$$

In rainfall, large Z_{DR} values indicate the presence of increasingly large and oblate raindrops, which backscatter more power at horizontal than at vertical polarization. Z_{DR} depends also strongly on the orientation of raindrops. When particles are well aligned (i.e., the canting angle distribution has a small spread), the pronounced contrast between horizontal and vertical reflectivity produces high Z_{DR} . In turbulent environments, where particle orientations become more random, the horizontal and vertical backscatter become more similar, leading to lower Z_{DR} (see also Figure E2b).

E1.3 Copolar cross-correlation coefficient

1010 The copolar cross-correlation coefficient ρ_{HV} represents the correlation between all backscattered echoes at H and V polarizations (Bringi and Chandrasekar, 2001):

$$\rho_{HV} = \frac{\left| \int_{D_{\min}}^{D_{\max}} s_{HH}^b(D) (s_{VV}^b(D))^* N(D) dD \right|}{\sqrt{\int_{D_{\min}}^{D_{\max}} |s_{HH}^b|^2 N(D) dD \int_{D_{\min}}^{D_{\max}} |s_{VV}^b|^2 N(D) dD}} \quad [-] \quad (\text{E6})$$

where * denotes the complex conjugate operator.

ρ_{HV} is highly sensitive to inhomogeneities in the hydrometeor population. It is typically high (> 0.95) in stratiform rain and in ice clouds with relatively uniform particle populations, but decreases in convective precipitation, mixed-phase regions, and areas dominated by aggregates (Matrosov et al., 2007). ρ_{HV} decreases with increasing Z_{DR} and σ_m (Thurai et al., 2008).

E1.4 Backscatter differential phase

The backscatter differential phase δ_{HV} , similarly to ρ_{HV} , is derived from the complex cross-covariance between the horizontally and vertically polarized backscattered fields. While ρ_{HV} quantifies the magnitude of the normalized correlation, δ_{HV} represents the phase of the same cross-covariance.

$$\delta_{HV} = \frac{180}{\pi} \arg \left[\int_{D_{\min}}^{D_{\max}} s_{HH}^b(D) (s_{VV}^b(D))^* N(D) dD \right] \text{ [deg]} \quad (\text{E7})$$

The differential phase shift occurs when nonspherical hydrometeors are large enough relative to the radar wavelength such that scattering is in the Mie regime (Trömel et al., 2013).



E1.5 Linear depolarization ratio

1025 The linear depolarization ratio LDR measures the power returned in the cross-polar channel relative to the copolar channel, providing insight into deviations from spherical symmetry and fluctuations in particle orientation:

$$\text{LDR} = 10 \log_{10} \left(\frac{\int_{D_{\min}}^{D_{\max}} |s_{\text{VH}}^b(D)|^2 N(D) dD}{\int_{D_{\min}}^{D_{\max}} |s_{\text{HH}}^b(D)|^2 N(D) dD} \right) = 10 \log_{10} \left(\frac{\int_{D_{\min}}^{D_{\max}} \sigma_{\text{VH}}^b(D) N(D) dD}{\int_{D_{\min}}^{D_{\max}} \sigma_{\text{HH}}^b(D) N(D) dD} \right) \quad [\text{dB}] \quad (\text{E8})$$

E2 Forward scattering radar variables

Propagation-related quantities are derived from the forward-scattering amplitude coefficients evaluated at the forward direction

1030 $\theta_s = 0^\circ$.

E2.1 Specific propagation differential phase

The specific propagation differential phase K_{DP} is the rate of change in phase between horizontal and vertical transmitted pulses, caused primarily by oriented, non-spherical hydrometeors:

$$K_{\text{DP}} = \frac{180}{\pi} 10^{-3} \lambda \int_{D_{\min}}^{D_{\max}} \text{Re}[s_{\text{HH}}^f(D) - s_{\text{VV}}^f(D)] N(D) dD \quad [\text{deg km}^{-1}] \quad (\text{E9})$$

1035 with the factor 10^{-3} used to convert $\text{mm}^2 \text{m}^{-3}$ to km^{-1} . K_{DP} is highly valuable for rainfall estimation because it is immune to radar calibration errors and partial beam blockage, and has a nearly linear relationship with the rain rate and specific attenuation in moderate to heavy rainfall. Similarly to Z_{DR} , K_{DP} also decreases with increasing canting angle spread because greater orientation randomness reduces the anisotropy of forward scattering between horizontally and vertically polarized waves.

E2.2 Specific attenuation

1040 Specific attenuation quantifies the rate at which the radar signal is weakened by extinction (scattering and absorption) as it propagates through the hydrometeor population:

$$A_{\text{H}} = 4.343 10^{-3} \int_{D_{\min}}^{D_{\max}} \sigma_{\text{H}}^{\text{ext}} N(D) dD \quad [\text{dB km}^{-1}] \quad (\text{E10})$$

$$A_{\text{V}} = 4.343 10^{-3} \int_{D_{\min}}^{D_{\max}} \sigma_{\text{V}}^{\text{ext}} N(D) dD \quad [\text{dB km}^{-1}] \quad (\text{E11})$$

1045 The factor 4.343 ($10 \log_{10}(e)$) arises from converting the natural logarithm form of extinction in the Beer-Lambert law to the decibel scale (Bringi and Chandrasekar, 2001).



E2.3 Differential attenuation

Differential attenuation quantifies the difference in specific attenuation between horizontal and vertical polarizations:

$$A_{DP} = A_H - A_V \text{ [dB km}^{-1}\text{]} \quad (\text{E12})$$

1050 In rainfall, A_{DP} increases with drop size and oblateness, as larger raindrops attenuate the horizontally polarized wave more strongly than the vertically polarized one.

Author contributions. GG and AB designed the project. GG developed the DISDRODB infrastructure and software. KC contributed significantly to the implementation of the DISDRODB L0 processing chain. CW, SPB, and RL contributed substantially to software testing and validation. ABR contributed to adapting the `pytmatrix` package to ensure compatibility with recent Python versions. GG prepared the
1055 manuscript with contributions from AB and CW. All authors have read and agreed to the published version of the paper.

Competing interests. At least one of the (co-)authors is a member of the editorial board of Atmospheric Measurement Techniques. The authors have no other competing interests to declare.

Acknowledgements. The authors thank all institutions that contributed disdrometer data to the DISDRODB archive. They also thank the many colleagues whose helpful discussions were fundamental to the conceptualization of the software, the development of the processing chains,
1060 and the design of the DISDRODB infrastructure. Their experience, perspectives, and insights were instrumental in shaping DISDRODB into its current form. The development of `disdrodb` has been supported by the ETH Domain Open Research Data (ORD) Contribute Grant 22938 and by EPFL internal funding.



References

- Abel, S. J. and Boutle, I. A.: An improved representation of the raindrop size distribution for single-moment microphysics schemes, *Quarterly Journal of the Royal Meteorological Society*, 138, 2151–2162, <https://doi.org/10.1002/qj.1949>, 2012.
- Adirosi, E., Volpi, E., Lombardo, F., and Baldini, L.: Raindrop size distribution: Fitting performance of common theoretical models, *Advances in Water Resources*, 96, 290–305, <https://doi.org/10.1016/j.advwatres.2016.07.010>, 2016.
- Adirosi, E., Porcù, F., Montopoli, M., Baldini, L., Bracci, A., Capozzi, V., Annella, C., Budillon, G., Bucchignani, E., Zollo, A. L., Cazzuli, O., Camisani, G., Bechini, R., Cremonini, R., Antonini, A., Ortolani, A., Melani, S., Valisa, P., and Scapin, S.: Database of the Italian disdrometer network, *Earth System Science Data*, 15, 2417–2429, <https://doi.org/10.5194/essd-15-2417-2023>, 2023.
- Andsager, K., Beard, K. V., and Laird, N. F.: Laboratory Measurements of Axis Ratios for Large Raindrops, *Journal of the Atmospheric Sciences*, 56, 2673–2683, [https://doi.org/10.1175/1520-0469\(1999\)056<2673:LMOARF>2.0.CO;2](https://doi.org/10.1175/1520-0469(1999)056<2673:LMOARF>2.0.CO;2), 1999.
- Angulo-Martínez, M., Beguería, S., and Kyselý, J.: Use of disdrometer data to evaluate the relationship of rainfall kinetic energy and intensity (KE-I), *Science of The Total Environment*, 568, 83–94, <https://doi.org/10.1016/j.scitotenv.2016.05.223>, 2016.
- Atlas, D., Srivastava, R. C., and Sekhon, R. S.: Doppler radar characteristics of precipitation at vertical incidence, *Reviews of Geophysics*, 11, 1–35, <https://doi.org/10.1029/RG011i001p00001>, 1973.
- Aydin, K. and Lure, Y.-M.: Millimeter wave scattering and propagation in rain: a computational study at 94 and 140 GHz for oblate spheroidal and spherical raindrops, *IEEE Transactions on Geoscience and Remote Sensing*, 29, 593–601, <https://doi.org/10.1109/36.135821>, 1991.
- Baire, Q., Dobre, M., Piette, A.-S., Lanza, L., Cauteruccio, A., Chinchella, E., Merlone, A., Kjeldsen, H., Nielsen, J., Østergaard, P. F., Parrondo, M., and Izquierdo, C. G.: Calibration Uncertainty of Non-Catching Precipitation Gauges, *Sensors*, 22, 6413, <https://doi.org/10.3390/s22176413>, 2022.
- Baldocchi, D., Falge, E., Gu, L., Olson, R., Hollinger, D., Running, S., Anthoni, P., Bernhofer, C., Davis, K., Evans, R., Fuentes, J., Goldstein, A., Katul, G., Law, B., Lee, X., Malhi, Y., Meyers, T., Munger, W., Oechel, W., Paw, K. T., Pilegaard, K., Schmid, H. P., Valentini, R., Verma, S., Vesala, T., Wilson, K., and Wofsy, S.: FLUXNET: A New Tool to Study the Temporal and Spatial Variability of Ecosystem-Scale Carbon Dioxide, Water Vapor, and Energy Flux Densities, *Bulletin of the American Meteorological Society*, 82, 2415–2434, [https://doi.org/10.1175/1520-0477\(2001\)082<2415:FANTTS>2.3.CO;2](https://doi.org/10.1175/1520-0477(2001)082<2415:FANTTS>2.3.CO;2), 2001.
- Barthazy, E. and Schefold, R.: Fall velocity of snowflakes of different riming degree and crystal types, *Atmospheric Research*, 82, 391–398, <https://doi.org/10.1016/j.atmosres.2005.12.009>, 2006.
- Barthazy, E., Göke, S., Schefold, R., and Högl, D.: An Optical Array Instrument for Shape and Fall Velocity Measurements of Hydrometeors, *Journal of Atmospheric and Oceanic Technology*, 21, 1400–1416, [https://doi.org/10.1175/1520-0426\(2004\)021<1400:AOAIFS>2.0.CO;2](https://doi.org/10.1175/1520-0426(2004)021<1400:AOAIFS>2.0.CO;2), 2004.
- Battaglia, A., Rustemeier, E., Tokay, A., Blahak, U., and Simmer, C.: PARSIVEL Snow Observations: A Critical Assessment, *Journal of Atmospheric and Oceanic Technology*, 27, 333–344, <https://doi.org/10.1175/2009JTECHA1332.1>, 2010.
- Beard, K. V.: Terminal Velocity and Shape of Cloud and Precipitation Drops Aloft, *Journal of the Atmospheric Sciences*, 33, 851–864, [https://doi.org/10.1175/1520-0469\(1976\)033<0851:TVASOC>2.0.CO;2](https://doi.org/10.1175/1520-0469(1976)033<0851:TVASOC>2.0.CO;2), 1976.
- Beard, K. V.: Simple Altitude Adjustments to Raindrop Velocities for Doppler Radar Analysis, *Journal of Atmospheric and Oceanic Technology*, 2, 468–471, [https://doi.org/10.1175/1520-0426\(1985\)002<0468:SAATRV>2.0.CO;2](https://doi.org/10.1175/1520-0426(1985)002<0468:SAATRV>2.0.CO;2), 1985.
- Beard, K. V. and Chuang, C.: A New Model for the Equilibrium Shape of Raindrops, *Journal of the Atmospheric Sciences*, 44, 1509–1524, [https://doi.org/10.1175/1520-0469\(1987\)044<1509:ANMFTE>2.0.CO;2](https://doi.org/10.1175/1520-0469(1987)044<1509:ANMFTE>2.0.CO;2), 1987.



- 1100 Beard, K. V., Bringi, V., and Thurai, M.: A new understanding of raindrop shape, *Atmospheric Research*, 97, 396–415, <https://doi.org/10.1016/j.atmosres.2010.02.001>, 2010.
- Bech, J. I., Johansen, N. F.-J., Madsen, M. B., Ásta Hannesdóttir, and Hasager, C. B.: Experimental study on the effect of drop size in rain erosion test and on lifetime prediction of wind turbine blades, *Renewable Energy*, 197, 776–789, <https://doi.org/10.1016/j.renene.2022.06.127>, 2022.
- 1105 Bennartz, R. and Petty, G. W.: The Sensitivity of Microwave Remote Sensing Observations of Precipitation to Ice Particle Size Distributions, *Journal of Applied Meteorology*, 40, 345–364, [https://doi.org/10.1175/1520-0450\(2001\)040<0345:TSOMRS>2.0.CO;2](https://doi.org/10.1175/1520-0450(2001)040<0345:TSOMRS>2.0.CO;2), 2001.
- Berghuijs, W. R., Woods, R. A., and Hrachowitz, M.: A precipitation shift from snow towards rain leads to a decrease in streamflow, *Nature Climate Change*, 4, 583–586, <https://doi.org/10.1038/nclimate2246>, 2014.
- Berghuijs, W. R., Woods, R. A., Hutton, C. J., and Sivapalan, M.: Dominant flood generating mechanisms across the United States, *Geophysical Research Letters*, 43, 4382–4390, <https://doi.org/10.1002/2016GL068070>, 2016.
- 1110 Berghuijs, W. R., Harrigan, S., Molnar, P., Slater, L. J., and Kirchner, J. W.: The Relative Importance of Different Flood-Generating Mechanisms Across Europe, *Water Resources Research*, 55, 4582–4593, <https://doi.org/10.1029/2019WR024841>, 2019.
- Blahak, U., Tracksdorf, P., and Antonoglou, N.: Deutscher Wetterdienst (DWD) / Disdrometer data of the Thies Laser Niederschlags Messer (LNM) since 2019 of about 150 German meteorological SYNOP stations [Data set], Zenodo, <https://doi.org/https://doi.org/10.5281/zenodo.15855617>, 2025.
- 1115 Blöschl, G.: Flood generation: process patterns from the raindrop to the ocean, *Hydrology and Earth System Sciences*, 26, 2469–2480, <https://doi.org/10.5194/hess-26-2469-2022>, 2022.
- Bolek, A. and Testik, F. Y.: Rainfall Microphysics Influenced by Strong Wind during a Tornadoic Storm, *Journal of Hydrometeorology*, 23, 733–746, <https://doi.org/10.1175/JHM-D-21-0004.1>, 2022.
- 1120 Bradley, S. G., Stow, C. D., and Lynch-Blosse, C. A.: Measurements of Rainfall Properties Using Long Optical Path Imaging, *Journal of Atmospheric and Oceanic Technology*, 17, 761–772, [https://doi.org/10.1175/1520-0426\(2000\)017<0761:MORPUL>2.0.CO;2](https://doi.org/10.1175/1520-0426(2000)017<0761:MORPUL>2.0.CO;2), 2000.
- Brandes, E. A., Zhang, G., and Vivekanandan, J.: Experiments in Rainfall Estimation with a Polarimetric Radar in a Subtropical Environment, *Journal of Applied Meteorology*, 41, 674–685, [https://doi.org/10.1175/1520-0450\(2002\)041<0674:EIREWA>2.0.CO;2](https://doi.org/10.1175/1520-0450(2002)041<0674:EIREWA>2.0.CO;2), 2002.
- Brandes, E. A., Ikeda, K., Thompson, G., and Schönhuber, M.: Aggregate terminal velocity/temperature relations, *Journal of Applied Meteorology and Climatology*, 47, 2729–2736, <https://doi.org/10.1175/2008JAMC1869.1>, 2008.
- 1125 Bringi, V. N. and Chandrasekar, V.: *Polarimetric Doppler Weather Radar*, Cambridge University Press, ISBN 9780521623841, <https://doi.org/10.1017/CBO9780511541094>, 2001.
- Brutsaert, W.: *Evaporation into the Atmosphere*, Springer Netherlands, ISBN 978-90-481-8365-4, <https://doi.org/10.1007/978-94-017-1497-6>, 1982.
- 1130 Cao, Q. and Zhang, G.: Errors in Estimating Raindrop Size Distribution Parameters Employing Disdrometer and Simulated Raindrop Spectra, *Journal of Applied Meteorology and Climatology*, 48, 406–425, <https://doi.org/10.1175/2008JAMC2026.1>, 2009.
- Capozzi, V., Annella, C., Montopoli, M., Adirosi, E., Fusco, G., and Budillon, G.: Influence of Wind-Induced Effects on Laser Disdrometer Measurements: Analysis and Compensation Strategies, *Remote Sensing*, 13, 3028, <https://doi.org/10.3390/rs13153028>, 2021.
- Cauteruccio, A., Chinchella, E., and Lanza, L. G.: The Overall Collection Efficiency of Catching-Type Precipitation Gauges in Windy
1135 Conditions, *Water Resources Research*, 60, <https://doi.org/10.1029/2023WR035098>, 2024.



- CEN: CEN/TC 318 Hydrometry — Measurement of precipitation intensity — Metrological requirements and test methods for non-catching type rain gauges. EN 18097:2025, Tech. rep., European Committee for Standardization, <https://standards.iteh.ai/catalog/standards/cen/fdd883d7-63d2-4b79-8aaa-1dd159b10cd1/en-18097-2025>, 2025.
- 1140 Chang, W.-Y., Wang, T.-C. C., and Lin, P.-L.: Characteristics of the Raindrop Size Distribution and Drop Shape Relation in Typhoon Systems in the Western Pacific from the 2D Video Disdrometer and NCU C-Band Polarimetric Radar, *Journal of Atmospheric and Oceanic Technology*, 26, 1973–1993, <https://doi.org/10.1175/2009JTECHA1236.1>, 2009.
- Chen, J.-Y., Trömel, S., Ryzhkov, A., and Simmer, C.: Assessing the benefits of specific attenuation for quantitative precipitation estimation with a C-band radar network, *Journal of Hydrometeorology*, 22, 2617–2631, <https://doi.org/10.1175/JHM-D-20-0299.1>, 2021.
- 1145 Chinchella, E., Cauteruccio, A., and Lanza, L. G.: Quantifying the Wind-Induced Bias of Rainfall Measurements for the Thies CLIMA Optical Disdrometer, *Water Resources Research*, 60, <https://doi.org/10.1029/2024WR037366>, 2024.
- Chinchella, E., Cauteruccio, A., and Lanza, L. G.: Impact of Wind on Rainfall Measurements Obtained from the OTT Parsivel2 Disdrometer, *Sensors*, 25, 6440, <https://doi.org/10.3390/s25206440>, 2025.
- Choler, P., Bayle, A., Fort, N., and Gascoïn, S.: Waning snowfields have transformed into hotspots of greening within the alpine zone, *Nature Climate Change*, 15, 80–85, <https://doi.org/10.1038/s41558-024-02177-x>, 2025.
- 1150 Chwala, C. and Kunstmann, H.: Commercial microwave link networks for rainfall observation: Assessment of the current status and future challenges, <https://doi.org/10.1002/WAT2.1337>, 2019.
- Cugerone, K. and Michele, C. D.: Johnson $\langle SB \rangle$ as general functional form for raindrop size distribution, *Water Resources Research*, 51, 6276–6289, <https://doi.org/10.1002/2014WR016484>, 2015.
- Dawson, D. T., Mansell, E. R., and Kumjian, M. R.: Does wind shear cause hydrometeor size sorting?, *Journal of the Atmospheric Sciences*, 1155 72, 340–348, <https://doi.org/10.1175/JAS-D-14-0084.1>, 2015.
- Deng, M., Giangrande, S. E., Jensen, M. P., Johnson, K., Williams, C. R., Comstock, J. M., Feng, Y.-C., Matthews, A., Lindenmaier, I. A., Wendler, T. G., Rocque, M., Zhou, A., Zhu, Z., Luke, E., and Wang, D.: Wet-radome attenuation in ARM cloud radars and its utilization in radar calibration using disdrometer measurements, *Atmospheric Measurement Techniques*, 18, 1641–1657, <https://doi.org/10.5194/amt-18-1641-2025>, 2025.
- 1160 Dolan, B., Fuchs, B., Rutledge, S. A., Barnes, E. A., and Thompson, E. J.: Primary Modes of Global Drop Size Distributions, *Journal of the Atmospheric Sciences*, 75, 1453–1476, <https://doi.org/10.1175/JAS-D-17-0242.1>, 2018.
- Dolan, B., Saleeby, S. M., Rutledge, S. A., van den Heever, S. C., and Valkenburg, K. V.: A Statistical Framework for Evaluating Rain Microphysics in Model Simulations and Disdrometer Observations, *Journal of Geophysical Research: Atmospheres*, 128, <https://doi.org/10.1029/2023JD038902>, 2023.
- 1165 Doviak, R. J. and Zrnić, D. S.: *Doppler Radar and Weather Observations*, Elsevier, ISBN 9780122214226, <https://doi.org/10.1016/C2009-0-22358-0>, 1993.
- Duncan, D. I., Eriksson, P., Pfreundschuh, S., Klepp, C., and Jones, D. C.: On the distinctiveness of observed oceanic raindrop distributions, *Atmospheric Chemistry and Physics*, 19, 6969–6984, <https://doi.org/10.5194/acp-19-6969-2019>, 2019.
- Dunn, R. E., Fowler, H. J., Green, A. C., and Lewis, E.: Tipping-bucket rain gauges: a review of the undercatch phenomenon, and methods for its reduction and correction, <https://doi.org/10.1002/wea.7736>, 2025.
- 1170 Eaton, B., Gregory, J., Drach, B., Taylor, K., Hankin, S., Blower, J., Caron, J., Signell, R., Bentley, P., Rappa, G., Höck, H., Pamment, A., Juckes, M., Raspaud, M., Horne, R., Whiteaker, T., Blodgett, D., Zender, C., Lee, D., Hassell, D., Snow, A. D., Kölling, T., Al-



- lured, D., Jelenak, A., Soerensen, A. M., Gaultier, L., and Herlédan, S.: NetCDF Climate and Forecast (CF) Metadata Conventions, <https://doi.org/10.5281/zenodo.14274886>, 2024.
- 1175 Ekelund, R., Eriksson, P., and Kahnert, M.: Microwave single-scattering properties of non-spheroidal raindrops, *Atmospheric Measurement Techniques*, 13, 6933–6944, <https://doi.org/10.5194/amt-13-6933-2020>, 2020.
- Ellis, R. A., Sandford, A. P., Jones, G. E., Richards, J., Petzing, J., and Coupland, J. M.: New laser technology to determine present weather parameters, in: *Measurement Science and Technology*, vol. 17, pp. 1715–1722, Institute of Physics Publishing, ISSN 13616501, <https://doi.org/10.1088/0957-0233/17/7/009>, 2006.
- 1180 Ellison, W. J.: Permittivity of Pure Water, at Standard Atmospheric Pressure, over the Frequency Range –25THz and the Temperature Range –100°C, *Journal of Physical and Chemical Reference Data*, 36, 1–18, <https://doi.org/10.1063/1.2360986>, 2007.
- Eriksson, P., Ekelund, R., Mendrok, J., Brath, M., Lemke, O., and Buehler, S. A.: A general database of hydrometeor single scattering properties at microwave and sub-millimetre wavelengths, *Earth System Science Data*, 10, 1301–1326, <https://doi.org/10.5194/essd-10-1301-2018>, 2018.
- 1185 ESIP: Attribute Convention for Data Discovery 1-3, https://wiki.esipfed.org/Attribute_Convention_for_Data_Discovery_1-3, 2015.
- Fehlmann, M., Rohrer, M., von Lerber, A., and Stoffel, M.: Automated precipitation monitoring with the Thies disdrometer: biases and ways for improvement, *Atmospheric Measurement Techniques*, 13, 4683–4698, <https://doi.org/10.5194/amt-13-4683-2020>, 2020.
- Feingold, G. and Levin, Z.: The Lognormal Fit to Raindrop Spectra from Frontal Convective Clouds in Israel, *Journal of Climate and Applied Meteorology*, 25, 1346–1363, [https://doi.org/10.1175/1520-0450\(1986\)025<1346:TLFTRS>2.0.CO;2](https://doi.org/10.1175/1520-0450(1986)025<1346:TLFTRS>2.0.CO;2), 1986.
- 1190 Fielding, M. D. and Janisková, M.: Direct 4D-Var assimilation of space-borne cloud radar reflectivity and lidar backscatter. Part I: Observation operator and implementation, *Quarterly Journal of the Royal Meteorological Society*, 146, 3877–3899, <https://doi.org/10.1002/qj.3878>, 2020.
- Filipovic, N.: AQUAS - A quality control tool at GeoSphere Austria, in: *EGU General Assembly*, <https://doi.org/10.5194/egusphere-egu25-17837>, 2025.
- 1195 Fischler, M. A. and Bolles, R. C.: Random sample consensus: a paradigm for model fitting with applications to image analysis and automated cartography, *Communications of the ACM*, 24, 381–395, <https://doi.org/10.1145/358669.358692>, 1981.
- Flatau, P. J., Walko, R. L., and Cotton, W. R.: Polynomial Fits to Saturation Vapor Pressure, *Journal of Applied Meteorology*, 31, 1507–1513, [https://doi.org/10.1175/1520-0450\(1992\)031<1507:PFTSVP>2.0.CO;2](https://doi.org/10.1175/1520-0450(1992)031<1507:PFTSVP>2.0.CO;2), 1992.
- Flynn, M., Choullarton, T., Gallagher, M., and Allan, J.: Disdrometer data at Whitworth Meteorological Observatory and Manchester Air Quality Supersite (2010–2025), *Zenodo*, <https://doi.org/https://doi.org/10.5281/zenodo.18619392>, 2026.
- 1200 Foundation, A. S.: ApacheParquet, <https://parquet.apache.org>, 2026.
- Frech, M., Hagen, M., and Mammen, T.: Monitoring the Absolute Calibration of a Polarimetric Weather Radar, *Journal of Atmospheric and Oceanic Technology*, 34, 599–615, <https://doi.org/10.1175/JTECH-D-16-0076.1>, 2017.
- Friedrich, K., Higgins, S., Masters, F. J., and Lopez, C. R.: Articulating and Stationary PARSIVEL Disdrometer Measurements in Conditions with Strong Winds and Heavy Rainfall, *Journal of Atmospheric and Oceanic Technology*, 30, 2063–2080, <https://doi.org/10.1175/JTECH-D-12-00254.1>, 2013.
- Garrett, T. J., Fallgatter, C., Shkurko, K., and Howlett, D.: Fall speed measurement and high-resolution multi-angle photography of hydrometeors in free fall, *Atmospheric Measurement Techniques*, 5, 2625–2633, <https://doi.org/10.5194/amt-5-2625-2012>, 2012.



- 1210 Gatidis, C., Schleiss, M., Unal, C., and Russchenberg, H.: A Critical Evaluation of the Adequacy of the Gamma Model for Representing Raindrop Size Distributions, *Journal of Atmospheric and Oceanic Technology*, 37, 1765–1779, <https://doi.org/10.1175/JTECH-D-19-0106.1>, 2020.
- Gatidis, C., Schleiss, M., and Unal, C.: Sensitivity analysis of DSD retrievals from polarimetric radar in stratiform rain based on the μ - Λ relationship, *Atmospheric Measurement Techniques*, 15, 4951–4969, <https://doi.org/10.5194/amt-15-4951-2022>, 2022.
- 1215 Gatidis, C., Schleiss, M., and Unal, C.: A new power-law model for $\langle i \rangle \mu$ – Λ relationships in convective and stratiform rainfall, *Atmospheric Measurement Techniques*, 17, 235–245, <https://doi.org/10.5194/amt-17-235-2024>, 2024.
- Gatlin, P. N., Thurai, M., Bringi, V. N., Petersen, W., Wolff, D., Tokay, A., Carey, L., and Wingo, M.: Searching for Large Raindrops: A Global Summary of Two-Dimensional Video Disdrometer Observations, *Journal of Applied Meteorology and Climatology*, 54, 1069–1089, <https://doi.org/10.1175/JAMC-D-14-0089.1>, 2015.
- Ghiggi, G., Candolfi, K., Pham-Ba, S., Longchamp, R., and Weil, C.: Itelab/disdrodb, <https://doi.org/10.5281/zenodo.7680581>, 2026.
- 1220 Giannetti, F., Reggiannini, R., Moretti, M., Adirosi, E., Baldini, L., Facheris, L., Antonini, A., Melani, S., Bacci, G., Petrolino, A., and Vaccaro, A.: Real-Time Rain Rate Evaluation via Satellite Downlink Signal Attenuation Measurement, *Sensors*, 17, 1864, <https://doi.org/10.3390/s17081864>, 2017.
- Gorgucci, E., Chandrasekar, V., Bringi, V. N., and Scarchilli, G.: Estimation of Raindrop Size Distribution Parameters from Polarimetric Radar Measurements, *Journal of the Atmospheric Sciences*, 59, 2373–2384, [https://doi.org/10.1175/1520-0469\(2002\)059<2373:EORSDP>2.0.CO;2](https://doi.org/10.1175/1520-0469(2002)059<2373:EORSDP>2.0.CO;2), 2002.
- 1225 Graf, M., Bareš, V., Messer, H., Nebuloni, R., Fencel, M., Chwala, C., Overeem, A., van de Beek, R., Olsson, J., Ostrometzky, J., Hanna, N., Uijlenhoet, R., Gottschalk, M., and Winterrath, T.: The Opportunistic Precipitation Sensing Network (OpenSense), *Bulletin of the American Meteorological Society*, <https://doi.org/10.1175/BAMS-D-25-0326.1>, 2025.
- Grazioli, J., Ghiggi, G., Billault-Roux, A.-C., and Berne, A.: MASCDB, a database of images, descriptors and microphysical properties of individual snowflakes in free fall, *Scientific Data*, 9, 186, <https://doi.org/10.1038/s41597-022-01269-7>, 2022.
- 1230 Grossklaus, M., Uhlig, K., and Hasse, L.: An Optical Disdrometer for Use in High Wind Speeds, *Journal of Atmospheric and Oceanic Technology*, 15, 1051–1059, [https://doi.org/10.1175/1520-0426\(1998\)015<1051:AODFUI>2.0.CO;2](https://doi.org/10.1175/1520-0426(1998)015<1051:AODFUI>2.0.CO;2), 1998.
- Gultepe, I., Sharman, R., Williams, P. D., Zhou, B., Ellrod, G., Minnis, P., Trier, S., Griffin, S., Yum, S. S., Gharabaghi, B., Feltz, W., Temimi, M., Pu, Z., Storer, L. N., Kneringer, P., Weston, M. J., ya Chuang, H., Thobois, L., Dimri, A. P., Dietz, S. J., França, G. B., Almeida, M. V., and Neto, F. L. A.: A Review of High Impact Weather for Aviation Meteorology, *Pure and Applied Geophysics*, 176, 1869–1921, <https://doi.org/10.1007/s00024-019-02168-6>, 2019.
- 1235 Han, J., Liu, Z., Woods, R., McVicar, T. R., Yang, D., Wang, T., Hou, Y., Guo, Y., Li, C., and Yang, Y.: Streamflow seasonality in a snow-dwindling world, *Nature*, 629, 1075–1081, <https://doi.org/10.1038/s41586-024-07299-y>, 2024.
- Hardin, J. and Guy, N.: PyDSD, <https://doi.org/https://doi.org/oi.org/10.5281/zenodo.9991>, 2014.
- 1240 Harpold, A. A. and Molotch, N. P.: Sensitivity of soil water availability to changing snowmelt timing in the western U.S., *Geophysical Research Letters*, 42, 8011–8020, <https://doi.org/10.1002/2015GL065855>, 2015.
- Harpold, A. A., Kaplan, M. L., Klos, P. Z., Link, T., McNamara, J. P., Rajagopal, S., Schumer, R., and Steele, C. M.: Rain or snow: hydrologic processes, observations, prediction, and research needs, *Hydrology and Earth System Sciences*, 21, 1–22, <https://doi.org/10.5194/hess-21-1-2017>, 2017.



- 1245 Hauser, D., Amayenc, P., Nutten, B., and Waldteufel, P.: A New Optical Instrument for Simultaneous Measurement of Raindrop Diameter and Fall Speed Distributions, *Journal of Atmospheric and Oceanic Technology*, 1, 256–269, [https://doi.org/10.1175/1520-0426\(1984\)001<0256:ANOIFS>2.0.CO;2](https://doi.org/10.1175/1520-0426(1984)001<0256:ANOIFS>2.0.CO;2), 1984.
- Heymsfield, A. and Wright, R.: Graupel and Hail Terminal Velocities: Does a “Supercritical” Reynolds Number Apply?, *Journal of the Atmospheric Sciences*, 71, 3392–3403, <https://doi.org/10.1175/JAS-D-14-0034.1>, 2014.
- 1250 Heymsfield, A., Szakáll, M., Jost, A., Giammanco, I., and Wright, R.: A Comprehensive Observational Study of Graupel and Hail Terminal Velocity, Mass Flux, and Kinetic Energy, *Journal of the Atmospheric Sciences*, 75, 3861–3885, <https://doi.org/10.1175/JAS-D-18-0035.1>, 2018.
- Heymsfield, A., Szakáll, M., Jost, A., Giammanco, I., Wright, R., and Brimelow, J.: A Comprehensive Observational Study of Graupel and Hail Terminal Velocity, Mass Flux, and Kinetic Energy - Corrigendum, *Journal of the Atmospheric Sciences*, 77, 405–412, <https://doi.org/10.1175/JAS-D-19-0185.1>, 2020.
- 1255 Heymsfield, A. J., Giammanco, I. M., and Wright, R.: Terminal velocities and kinetic energies of natural hailstones, *Geophysical Research Letters*, 41, 8666–8672, <https://doi.org/10.1002/2014GL062324>, 2014.
- Hogg, D. C.: Millimeter-Wave Communication through the Atmosphere, *Science*, 159, 39–46, <https://doi.org/10.1126/science.159.3810.39>, 1968.
- 1260 Holben, B., Eck, T., Slutsker, I., Tanré, D., Buis, J., Setzer, A., Vermote, E., Reagan, J., Kaufman, Y., Nakajima, T., Lavenu, F., Jankowiak, I., and Smirnov, A.: AERONET—A Federated Instrument Network and Data Archive for Aerosol Characterization, *Remote Sensing of Environment*, 66, 1–16, [https://doi.org/10.1016/S0034-4257\(98\)00031-5](https://doi.org/10.1016/S0034-4257(98)00031-5), 1998.
- Hong, G.: Radar backscattering properties of nonspherical ice crystals at 94 GHz, *Journal of Geophysical Research: Atmospheres*, 112, <https://doi.org/10.1029/2007JD008839>, 2007.
- 1265 Hoyer, S. and Hamman, J.: xarray: N-D labeled Arrays and Datasets in Python, *Journal of Open Research Software*, 5, 10, <https://doi.org/10.5334/jors.148>, 2017.
- Huang, G.-J., Bringi, V. N., and Thurai, M.: Orientation Angle Distributions of Drops after an 80-m Fall Using a 2D Video Disdrometer, *Journal of Atmospheric and Oceanic Technology*, 25, 1717–1723, <https://doi.org/10.1175/2008JTECHA1075.1>, 2008.
- Humphrey, M. D., Istok, J. D., Lee, J. Y., Hevesi, J. A., and Flint, A. L.: A New Method for Automated Dynamic Calibration of Tipping-Bucket Rain Gauges, *Journal of Atmospheric and Oceanic Technology*, 14, 1513–1519, [https://doi.org/10.1175/1520-0426\(1997\)014<1513:ANMFAD>2.0.CO;2](https://doi.org/10.1175/1520-0426(1997)014<1513:ANMFAD>2.0.CO;2), 1997.
- 1270 Huuskonen, A., Saltikoff, E., and Holleman, I.: The Operational Weather Radar Network in Europe, *Bulletin of the American Meteorological Society*, 95, 897–907, <https://doi.org/10.1175/BAMS-D-12-00216.1>, 2014.
- Ignaccolo, M. and Michele, C. D.: A worldwide data science investigation of rainfall, *Journal of Hydrometeorology*, <https://doi.org/10.1175/JHM-D-21-0211.1>, 2022.
- 1275 Illingworth, A. J. and Blackman, T. M.: The Need to Represent Raindrop Size Spectra as Normalized Gamma Distributions for the Interpretation of Polarization Radar Observations, *Journal of Applied Meteorology*, 41, 286–297, [https://doi.org/10.1175/1520-0450\(2002\)041<0286:TNTRRS>2.0.CO;2](https://doi.org/10.1175/1520-0450(2002)041<0286:TNTRRS>2.0.CO;2), 2002.
- Illingworth, A. J. and Stevens, C. J.: An Optical Disdrometer for the Measurement of Raindrop Size Spectra in Windy Conditions, *Journal of Atmospheric and Oceanic Technology*, 4, 411–421, [https://doi.org/10.1175/1520-0426\(1987\)004<0411:AODFTM>2.0.CO;2](https://doi.org/10.1175/1520-0426(1987)004<0411:AODFTM>2.0.CO;2), 1987.
- 1280 Illingworth, A. J., Hogan, R. J., O’Connor, E., Bouniol, D., Brooks, M. E., Delanoé, J., Donovan, D. P., Eastment, J. D., Gaussiat, N., Goddard, J. W. F., Haefelin, M., Baltink, H. K., Krasnov, O. A., Pelon, J., Piriou, J.-M., Protat, A., Russchenberg, H. W. J., Seifert, A.,



- Tompkins, A. M., van Zadelhoff, G.-J., Vinit, F., Willén, U., Wilson, D. R., and Wrench, C. L.: Cloudnet - Continuous Evaluation of Cloud Profiles in Seven Operational Models Using Ground-Based Observations, *Bulletin of the American Meteorological Society*, 88, 883–898, <https://doi.org/10.1175/BAMS-88-6-883>, 2007.
- 1285
- ITU-R: Recommendation ITU-R P.837-8: Characteristics of precipitation for propagation modelling, Tech. rep., International Telecommunication Union, Radiocommunication Sector (ITU-R), 2025.
- Jaffrain, J. and Berne, A.: Experimental Quantification of the Sampling Uncertainty Associated with Measurements from PARSIVEL Disdrometers, *Journal of Hydrometeorology*, 12, 352–370, <https://doi.org/10.1175/2010JHM1244.1>, 2011.
- 1290 Jaffrain, J., Studzinski, A., and Berne, A.: A network of disdrometers to quantify the small-scale variability of the raindrop size distribution, *Water Resources Research*, 47, <https://doi.org/10.1029/2010WR009872>, 2011.
- Johannsen, L. L., Zambon, N., Strauss, P., Dostal, T., Neumann, M., Zumr, D., Cochrane, T. A., and Klik, A.: Impact of Disdrometer Types on Rainfall Erosivity Estimation, *Water*, 12, 963, <https://doi.org/10.3390/w12040963>, 2020.
- Jones, R. C.: A New Calculus for the Treatment of Optical Systems I Description and Discussion of the Calculus, *Journal of the Optical Society of America*, 31, 488, <https://doi.org/10.1364/JOSA.31.000488>, 1941.
- 1295
- Joss, J. and Waldvogel, A.: Ein Spektrograph für Niederschlagstropfen mit automatischer Auswertung, *pure and applied geophysics*, 68, 240–246, <https://doi.org/10.1007/BF00874898>, 1967.
- Kalina, E. A., Friedrich, K., Ellis, S. M., and Burgess, D. W.: Comparison of Disdrometer and X-Band Mobile Radar Observations in Convective Precipitation, *Monthly Weather Review*, 142, 2414–2435, <https://doi.org/10.1175/MWR-D-14-00039.1>, 2014.
- 1300 Kathiravelu, G., Lucke, T., and Nichols, P.: Rain Drop Measurement Techniques: A Review, *Water*, 8, 29, <https://doi.org/10.3390/w8010029>, 2016.
- Kidd, C., Becker, A., Huffman, G. J., Muller, C. L., Joe, P., Skofronick-Jackson, G., and Kirschbaum, D. B.: So, How Much of the Earth's Surface Is Covered by Rain Gauges?, *Bulletin of the American Meteorological Society*, 98, 69–78, <https://doi.org/10.1175/BAMS-D-14-00283.1>, 2017.
- 1305 Kikuchi, K., Kameda, T., Higuchi, K., and Yamashita, A.: A global classification of snow crystals, ice crystals, and solid precipitation based on observations from middle latitudes to polar regions, *Atmospheric Research*, 132-133, 460–472, <https://doi.org/10.1016/j.atmosres.2013.06.006>, 2013.
- Kim, D.-K. and Song, C.-K.: Characteristics of vertical velocities estimated from drop size and fall velocity spectra of a Parsivel disdrometer, *Atmospheric Measurement Techniques*, 11, 3851–3860, <https://doi.org/10.5194/amt-11-3851-2018>, 2018.
- 1310 King, F., Pettersen, C., Dolan, B., Shates, J., and Posselt, D.: Decoding global precipitation processes and particle evolution using unsupervised learning, *Science Advances*, 11, 162, <https://doi.org/10.1126/sciadv.adu0162>, 2025.
- Klepp, C.: The oceanic shipboard precipitation measurement network for surface validation — OceanRAIN, *Atmospheric Research*, 163, 74–90, <https://doi.org/10.1016/j.atmosres.2014.12.014>, 2015.
- 1315 Klepp, C., Michel, S., Protat, A., Burdanowitz, J., Albern, N., Kähnert, M., Dahl, A., Louf, V., Bakan, S., and Buehler, S. A.: OceanRAIN, a new in-situ shipboard global ocean surface-reference dataset of all water cycle components, *Scientific Data*, 5, 180 122, <https://doi.org/10.1038/sdata.2018.122>, 2018.
- Kneifel, S., Löhnert, U., Battaglia, A., Crewell, S., and Siebler, D.: Snow scattering signals in ground-based passive microwave radiometer measurements, *Journal of Geophysical Research: Atmospheres*, 115, <https://doi.org/10.1029/2010JD013856>, 2010.
- Kneifel, S., Neto, J. D., Ori, D., Moisseev, D., Tyynelä, J., Adams, I. S., Kuo, K.-S., Bennartz, R., Berne, A., Clothiaux, E. E., Eriksson, P., Geer, A. J., Honeyager, R., Leinonen, J., and Westbrook, C. D.: Summer Snowfall Workshop: Scattering Properties of Realistic Frozen
- 1320



- Hydrometeors from Simulations and Observations, as well as Defining a New Standard for Scattering Databases, *Bulletin of the American Meteorological Society*, 99, ES55–ES58, <https://doi.org/10.1175/BAMS-D-17-0208.1>, 2018.
- Kneifel, S., Leinonen, J., Tyynelä, J., Ori, D., and Battaglia, A.: Scattering of Hydrometeors, vol. 67, pp. 249–276, Springer, https://doi.org/10.1007/978-3-030-24568-9_15, 2020.
- 1325 Knight, N. C.: Measurement and Interpretation of Hailstone Density and Terminal Velocity, *Journal of the Atmospheric Sciences*, 40, 1510–1516, [https://doi.org/10.1175/1520-0469\(1983\)040<1510:MAIOHD>2.0.CO;2](https://doi.org/10.1175/1520-0469(1983)040<1510:MAIOHD>2.0.CO;2), 1983.
- Kochendorfer, J., Rasmussen, R., Wolff, M., Baker, B., Hall, M. E., Meyers, T., Landolt, S., Jachcik, A., Isaksen, K., Brækkan, R., and Leeper, R.: The quantification and correction of wind-induced precipitation measurement errors, *Hydrology and Earth System Sciences*, 21, 1973–1989, <https://doi.org/10.5194/hess-21-1973-2017>, 2017.
- 1330 Kotsuki, S., Terasaki, K., Satoh, M., and Miyoshi, T.: Ensemble-Based Data Assimilation of GPM DPR Reflectivity: Cloud Microphysics Parameter Estimation With the Nonhydrostatic Icosahedral Atmospheric Model (NICAM), *Journal of Geophysical Research: Atmospheres*, 128, <https://doi.org/10.1029/2022JD037447>, 2023.
- Kratzert, F., Nearing, G., Addor, N., Erickson, T., Gauch, M., Gilon, O., Gudmundsson, L., Hassidim, A., Klotz, D., Nevo, S., Shalev, G., and Matias, Y.: Caravan - A global community dataset for large-sample hydrology, *Scientific Data*, 10, 61, <https://doi.org/10.1038/s41597-023-01975-w>, 2023.
- 1335 Kumjian, M. R. and Ryzhkov, A. V.: The Impact of Size Sorting on the Polarimetric Radar Variables, *Journal of the Atmospheric Sciences*, 69, 2042–2060, <https://doi.org/10.1175/JAS-D-11-0125.1>, 2012.
- Ladino-Rincon, A., Nesbitt, S. W., Girolamo, L. D., Rauber, R. M., McFarquhar, G. M., and Lawson, R. P.: Droplet Size Distribution Retrieval from Dual-Frequency Precipitation Radar Measurement Using a Deep Neural Network, *Journal of Atmospheric and Oceanic Technology*, 42, 1549–1566, <https://doi.org/10.1175/JTECH-D-25-0004.1>, 2025.
- 1340 Laj, P., Myhre, C. L., Riffault, V., Amiridis, V., Fuchs, H., Eleftheriadis, K., Petäjä, T., Salameh, T., Kivekäs, N., Juurola, E., Saponaro, G., Philippin, S., Cornacchia, C., Arboledas, L. A., Baars, H., Claude, A., Mazière, M. D., Dils, B., Dufresne, M., Evangeliou, N., Favez, O., Fiebig, M., Haeffelin, M., Herrmann, H., Höhler, K., Illmann, N., Kreuter, A., Ludewig, E., Marinou, E., Möhler, O., Mona, L., Murberg, L. E., Nicolae, D., Novelli, A., O’Connor, E., Ohneiser, K., Altieri, R. M. P., Picquet-Varrault, B., van Pinxteren, D., Pospichal, B., Putaud, J.-P., Reimann, S., Siomos, N., Stachlewska, I., Tillmann, R., Voudouri, K. A., Wandinger, U., Wiedensohler, A., Apituley, A., Comerón, A., Gysel-Beer, M., Mihalopoulos, N., Nikolova, N., Pietruczuk, A., Sauvage, S., Sciare, J., Skov, H., Svendby, T., Swietlicki, E., Tonev, D., Vaughan, G., Zdimal, V., Baltensperger, U., Doussin, J.-F., Kulmala, M., Pappalardo, G., Sundet, S. S., and Vana, M.: Aerosol, Clouds and Trace Gases Research Infrastructure (ACTRIS): The European Research Infrastructure Supporting Atmospheric Science, *Bulletin of the American Meteorological Society*, 105, E1098–E1136, <https://doi.org/10.1175/BAMS-D-23-0064.1>, 2024.
- 1345 Lanza, L. G. and Stagi, L.: High resolution performance of catching type rain gauges from the laboratory phase of the WMO Field Intercomparison of Rain Intensity Gauges, *Atmospheric Research*, 94, 555–563, <https://doi.org/10.1016/j.atmosres.2009.04.012>, 2009.
- Lanza, L. G. and Vuerich, E.: The WMO Field Intercomparison of Rain Intensity Gauges, *Atmospheric Research*, 94, 534–543, <https://doi.org/10.1016/j.atmosres.2009.06.012>, 2009.
- Lanza, L. G., Merlone, A., Cauteruccio, A., Chinchella, E., Stagnaro, M., Dobre, M., Izquierdo, M. C. G., Nielsen, J., Kjeldsen, H., Roulet, Y. A., Coppa, G., Musacchio, C., Bordianu, C., and Parrondo, M.: Calibration of non-catching precipitation measurement instruments: A review, *Meteorological Applications*, 28, <https://doi.org/10.1002/met.2002>, 2021.
- 1355 Larsen, M. L., Kostinski, A. B., and Jameson, A. R.: Further evidence for superterminal raindrops, *Geophysical Research Letters*, 41, 6914–6918, <https://doi.org/10.1002/2014GL061397>, 2014.



- Laurie, J. A. P.: Hail and Its Effects on Buildings, Council for Scientific and Industrial Research, 176, 1960.
- 1360 Lee, G., Bringi, V., and Thurai, M.: The Retrieval of Drop Size Distribution Parameters Using a Dual-Polarimetric Radar, Remote Sensing, 15, 1063, <https://doi.org/10.3390/rs15041063>, 2023.
- Lee, G. W., Zawadzki, I., Szyrmer, W., Sempere-Torres, D., and Uijlenhoet, R.: A General Approach to Double-Moment Normalization of Drop Size Distributions, Journal of Applied Meteorology, 43, 264–281, [https://doi.org/10.1175/1520-0450\(2004\)043<0264:AGATDN>2.0.CO;2](https://doi.org/10.1175/1520-0450(2004)043<0264:AGATDN>2.0.CO;2), 2004.
- 1365 Lee, J.-E., Jung, S.-H., Park, H.-M., Kwon, S., Lin, P.-L., and Lee, G.: Classification of precipitation types using fall velocity-diameter relationships from 2D-video disdrometer measurements, Advances in Atmospheric Sciences, 32, 1277–1290, <https://doi.org/10.1007/s00376-015-4234-4>, 2015.
- Leeper, R. D., Palecki, M. A., and Davis, E.: Methods to calculate precipitation from weighing-bucket gauges with redundant depth measurements, Journal of Atmospheric and Oceanic Technology, 32, 1179–1190, <https://doi.org/10.1175/JTECH-D-14-00185.1>, 2015.
- 1370 Leijnse, H. and Uijlenhoet, R.: The effect of reported high-velocity small raindrops on inferred drop size distributions and derived power laws, Atmospheric Chemistry and Physics, 10, 6807–6818, <https://doi.org/10.5194/acp-10-6807-2010>, 2010.
- Leijnse, H., Uijlenhoet, R., and Stricker, J. N.: Rainfall measurement using radio links from cellular communication networks, Water Resources Research, 43, <https://doi.org/10.1029/2006WR005631>, 2007.
- Leinonen, J.: High-level interface to T-matrix scattering calculations: architecture, capabilities and limitations, Optics Express, 22, 1655, <https://doi.org/10.1364/OE.22.001655>, 2014.
- 1375 Leinonen, J., Kneifel, S., Moisseev, D., Tyynelä, J., Tanelli, S., and Nousiainen, T.: Evidence of nonspheroidal behavior in millimeter-wavelength radar observations of snowfall, Journal of Geophysical Research: Atmospheres, 117, <https://doi.org/10.1029/2012JD017680>, 2012.
- Lempio, G. E., Bumke, K., and Macke, A.: Measurement of solid precipitation with an optical disdrometer, Advances in Geosciences, 10, 91–97, <https://doi.org/10.5194/adgeo-10-91-2007>, 2007.
- 1380 Levia, D. F., Hudson, S. A., Llorens, P., and Nanko, K.: Throughfall drop size distributions: a review and prospectus for future research, WIREs Water, 4, <https://doi.org/10.1002/wat2.1225>, 2017.
- Lhermitte, R. M.: Observation of rain at vertical incidence with a 94 GHz Doppler radar: An insight on Mie scattering, Geophysical Research Letters, 15, 1125–1128, <https://doi.org/10.1029/GL015i010p01125>, 1988.
- 1385 Liao, L. and Meneghini, R.: Examination of Effective Dielectric Constants of Nonspherical Mixed-Phase Hydrometeors, Journal of Applied Meteorology and Climatology, 52, 197–212, <https://doi.org/10.1175/JAMC-D-11-0244.1>, 2013.
- Liao, L., Meneghini, R., and Tokay, A.: Uncertainties of GPM DPR Rain Estimates Caused by DSD Parameterizations, Journal of Applied Meteorology and Climatology, 53, 2524–2537, <https://doi.org/10.1175/JAMC-D-14-0003.1>, 2014.
- Liebe, H. J., Hufford, G. A., and Manabe, T.: A model for the complex permittivity of water at frequencies below 1 THz, International Journal of Infrared and Millimeter Waves, 12, 659–675, <https://doi.org/10.1007/BF01008897>, 1991.
- 1390 Lin, L., Bao, X., Zhang, S., Zhao, B., and Xia, W.: Correction to raindrop size distributions measured by PARSIVEL disdrometers in strong winds, Atmospheric Research, 260, 105 728, <https://doi.org/10.1016/j.atmosres.2021.105728>, 2021.
- Liu, G.: A Database of Microwave Single-Scattering Properties for Nonspherical Ice Particles, Bulletin of the American Meteorological Society, 89, 1563–1570, <https://doi.org/10.1175/2008BAMS2486.1>, 2008.
- 1395 Locatelli, J. D. and Hobbs, P. V.: Fall speeds and masses of solid precipitation particles, Journal of Geophysical Research, 79, 2185–2197, <https://doi.org/10.1029/JC079i015p02185>, 1974.



- Löffler-Mang, M. and Joss, J.: An Optical Disdrometer for Measuring Size and Velocity of Hydrometeors, *Journal of Atmospheric and Oceanic Technology*, 17, 130–139, [https://doi.org/10.1175/1520-0426\(2000\)017<0130:AODFMS>2.0.CO;2](https://doi.org/10.1175/1520-0426(2000)017<0130:AODFMS>2.0.CO;2), 2000.
- Maahn, M., Moisseev, D., Steinke, I., Maherndl, N., and Shupe, M. D.: Introducing the Video In Situ Snowfall Sensor (VISS), *Atmospheric Measurement Techniques*, 17, 899–919, <https://doi.org/10.5194/amt-17-899-2024>, 2024.
- Maitra, A. and Gibbins, C. J.: Modeling of raindrop size distributions from multiwavelength rain attenuation measurements, *Radio Science*, 34, 657–666, <https://doi.org/10.1029/1998RS900045>, 1999.
- Mankin, J. S., Viviroli, D., Singh, D., Hoekstra, A. Y., and Diffenbaugh, N. S.: The potential for snow to supply human water demand in the present and future, *Environmental Research Letters*, 10, 114 016, <https://doi.org/10.1088/1748-9326/10/11/114016>, 2015.
- Marsalek, J.: Calibration of the tipping-bucket raingage, *Journal of Hydrology*, 53, 343–354, [https://doi.org/10.1016/0022-1694\(81\)90010-X](https://doi.org/10.1016/0022-1694(81)90010-X), 1981.
- Marshall, J. S. and Palmer, W. M. K.: THE DISTRIBUTION OF RAINDROPS WITH SIZE, *Journal of Meteorology*, 5, 165–166, [https://doi.org/10.1175/1520-0469\(1948\)005<0165:TDORWS>2.0.CO;2](https://doi.org/10.1175/1520-0469(1948)005<0165:TDORWS>2.0.CO;2), 1948.
- Mather, J. H. and Voyles, J. W.: The Arm Climate Research Facility: A Review of Structure and Capabilities, *Bulletin of the American Meteorological Society*, 94, 377–392, <https://doi.org/10.1175/BAMS-D-11-00218.1>, 2013.
- Matrosov, S. Y., Clark, K. A., and Kingsmill, D. E.: A Polarimetric Radar Approach to Identify Rain, Melting-Layer, and Snow Regions for Applying Corrections to Vertical Profiles of Reflectivity, *Journal of Applied Meteorology and Climatology*, 46, 154–166, <https://doi.org/10.1175/JAM2508.1>, 2007.
- Maur, A. N. A.: Statistical Tools for Drop Size Distributions: Moments and Generalized Gamma, *Journal of the Atmospheric Sciences*, 58, 407–418, [https://doi.org/10.1175/1520-0469\(2001\)058<0407:STFDSD>2.0.CO;2](https://doi.org/10.1175/1520-0469(2001)058<0407:STFDSD>2.0.CO;2), 2001.
- McCabe, G. J., Clark, M. P., and Hay, L. E.: Rain-on-Snow Events in the Western United States, *Bulletin of the American Meteorological Society*, 88, 319–328, <https://doi.org/10.1175/BAMS-88-3-319>, 2007.
- McKinney, W.: Data Structures for Statistical Computing in Python, in: *Proc. of the 9th Python in Science Conf.*, pp. 56–61, <https://doi.org/10.25080/Majora-92bf1922-00a>, 2010.
- Messer, H., Zinevich, A., and Alpert, P.: Environmental Monitoring by Wireless Communication Networks, *Science*, 312, 713–713, <https://doi.org/10.1126/science.1120034>, 2006.
- Mishchenko, M. I.: Calculation of the amplitude matrix for a nonspherical particle in a fixed orientation, *Applied Optics*, 39, 1026, <https://doi.org/10.1364/AO.39.001026>, 2000.
- Mishchenko, M. I. and Travis, L. D.: Capabilities and limitations of a current FORTRAN implementation of the T-matrix method for randomly oriented, rotationally symmetric scatterers, *Journal of Quantitative Spectroscopy and Radiative Transfer*, 60, 309–324, [https://doi.org/10.1016/S0022-4073\(98\)00008-9](https://doi.org/10.1016/S0022-4073(98)00008-9), 1998.
- Mishchenko, M. I., Travis, L. D., and Mackowski, D. W.: T-matrix computations of light scattering by nonspherical particles: A review, *Journal of Quantitative Spectroscopy and Radiative Transfer*, 55, 535–575, [https://doi.org/10.1016/0022-4073\(96\)00002-7](https://doi.org/10.1016/0022-4073(96)00002-7), 1996.
- Mishchenko, M. I., Hovenier, J. W., and Travis, L. D.: *Light scattering by nonspherical particles : theory, measurements, and applications*, Academic Press, ISBN 0124986609, 2000.
- Mitchell, D. L.: Use of Mass- and Area-Dimensional Power Laws for Determining Precipitation Particle Terminal Velocities, *Journal of the Atmospheric Sciences*, 53, 1710–1723, [https://doi.org/10.1175/1520-0469\(1996\)053<1710:UOMAAD>2.0.CO;2](https://doi.org/10.1175/1520-0469(1996)053<1710:UOMAAD>2.0.CO;2), place: Boston MA, USA
Publisher: American Meteorological Society, 1996.



- Mitchell, D. L., Zhang, R., and Pitter, R. L.: Mass-Dimensional Relationships for Ice Particles and the Influence of Riming on Snowfall Rates, *Journal of Applied Meteorology*, 29, 153–163, [https://doi.org/10.1175/1520-0450\(1990\)029<0153:MDRFIP>2.0.CO;2](https://doi.org/10.1175/1520-0450(1990)029<0153:MDRFIP>2.0.CO;2), 1990.
- 1435 Montero-Martínez, G. and García-García, F.: On the behaviour of raindrop fall speed due to wind, *Quarterly Journal of the Royal Meteorological Society*, 142, 2013–2020, <https://doi.org/10.1002/qj.2794>, 2016.
- Montero-Martínez, G., Kostinski, A. B., Shaw, R. A., and García-García, F.: Do all raindrops fall at terminal speed?, *Geophysical Research Letters*, 36, <https://doi.org/10.1029/2008GL037111>, 2009.
- 1440 Morrison, H. and Grabowski, W. W.: Comparison of bulk and bin warm-rain microphysics models using a kinematic framework, *Journal of the Atmospheric Sciences*, 64, 2839–2861, <https://doi.org/10.1175/JAS3980>, 2007.
- Morrison, H., van Lier-Walqui, M., Fridlind, A. M., Grabowski, W. W., Harrington, J. Y., Hoose, C., Korolev, A., Kumjian, M. R., Milbrandt, J. A., Pawlowska, H., Posselt, D. J., Prat, O. P., Reimel, K. J., Shima, S. I., van Dierenhoven, B., and Xue, L.: Confronting the Challenge of Modeling Cloud and Precipitation Microphysics, *Journal of Advances in Modeling Earth Systems*, 12, <https://doi.org/10.1029/2019MS001689>, 2020.
- 1445 Myagkov, A., Nomokonova, T., and Frech, M.: Empirical model for backscattering polarimetric variables in rain at W-band: motivation and implications, *Atmospheric Measurement Techniques*, 18, 1621–1640, <https://doi.org/10.5194/amt-18-1621-2025>, 2025.
- Nebuloni, R., Giannetti, F., Sapienza, F., Lottici, V., Adirosi, E., Roversi, G., Covi, E., Gianoglio, C., Colli, M., and Michele, C. D.: A Review of Technical Aspects and Challenges in Opportunistic Rainfall Estimation Using Satellite and Terrestrial Microwave Links: How wireless infrastructure can be used for rainfall monitoring, *IEEE Geoscience and Remote Sensing Magazine*, 13, 266–296, <https://doi.org/10.1109/MGRS.2025.3573645>, 2025.
- 1450 Newman, A. J., Kucera, P. A., and Bliven, L. F.: Presenting the Snowflake Video Imager (SVI), *Journal of Atmospheric and Oceanic Technology*, 26, 167–179, <https://doi.org/10.1175/2008JTECHA1148.1>, 2009.
- Niquet, L., Tridon, F., Grzegorzczak, P., Causse, A., Bordet, B., Wobrock, W., and Planche, C.: Evaluation of the Representation of Raindrop Self-Collection and Breakup in Two-Moment Bulk Models Using a Multifrequency Radar Retrieval, *Journal of Geophysical Research: Atmospheres*, 129, <https://doi.org/10.1029/2024JD041269>, 2024.
- 1455 Norrman, J., Eriksson, M., and Lindqvist, S.: Relationships between road slipperiness, traffic accident risk and winter road maintenance activity, *Climate Research*, 15, 185–193, <https://doi.org/10.3354/cr015185>, 2000.
- Ori, D., von Terzi, L., Karrer, M., and Kneifel, S.: snowScatt 1.0: consistent model of microphysical and scattering properties of rimed and unrimed snowflakes based on the self-similar Rayleigh–Gans approximation, *Geoscientific Model Development*, 14, 1511–1531, <https://doi.org/10.5194/gmd-14-1511-2021>, 2021.
- 1460 Overeem, A., Leijnse, H., and Uijlenhoet, R.: Country-wide rainfall maps from cellular communication networks, *Proceedings of the National Academy of Sciences*, 110, 2741–2745, <https://doi.org/10.1073/pnas.1217961110>, 2013.
- Pappalardo, G., Amodeo, A., Apituley, A., Comeron, A., Freudenthaler, V., Linné, H., Ansmann, A., Bösenberg, J., D’Amico, G., Mattis, I., Mona, L., Wandinger, U., Amiridis, V., Alados-Arboledas, L., Nicolae, D., and Wiegner, M.: EARLINET: Towards an advanced sustainable European aerosol lidar network, *Atmospheric Measurement Techniques*, 7, 2389–2409, <https://doi.org/10.5194/amt-7-2389-2014>, 2014.
- 1465 Petan, S., Rusjan, S., Vidmar, A., and Mikoš, M.: The rainfall kinetic energy–intensity relationship for rainfall erosivity estimation in the mediterranean part of Slovenia, *Journal of Hydrology*, 391, 314–321, <https://doi.org/10.1016/j.jhydrol.2010.07.031>, 2010.
- 1470 Petan, S., Ghiggi, G., and Brujić, M.: Raindrop size distribution (DSD) dataset, 2018–2025, Slovenia [Data set]., Zenodo, <https://doi.org/https://doi.org/10.5281/zenodo.17257451>, 2025.



- Pickering, B. S., Neely, R. R., and Harrison, D.: The Disdrometer Verification Network (DiVeN): A UK network of laser precipitation instruments, *Atmospheric Measurement Techniques*, 12, 5845–5861, <https://doi.org/10.5194/amt-12-5845-2019>, 2019.
- Pollock, M. D., O'Donnell, G., Quinn, P., Dutton, M., Black, A., Wilkinson, M. E., Colli, M., Stagnaro, M., Lanza, L. G., Lewis, E., Kilsby, C. G., and O'Connell, P. E.: Quantifying and Mitigating Wind-Induced Undercatch in Rainfall Measurements, *Water Resources Research*, 54, 3863–3875, <https://doi.org/10.1029/2017WR022421>, 2018.
- Pruppacher, H. R. and Pitter, R. L.: A Semi-Empirical Determination of the Shape of Cloud and Rain Drops, *Journal of the Atmospheric Sciences*, 28, 86–94, [https://doi.org/10.1175/1520-0469\(1971\)028<0086:ASEDOT>2.0.CO;2](https://doi.org/10.1175/1520-0469(1971)028<0086:ASEDOT>2.0.CO;2), 1971.
- Raupach, T. H. and Berne, A.: Correction of raindrop size distributions measured by Parsivel disdrometers, using a two-dimensional video disdrometer as a reference, *Atmospheric Measurement Techniques*, 8, 343–365, <https://doi.org/10.5194/amt-8-343-2015>, 2015.
- Raupach, T. H. and Berne, A.: Spatial interpolation of experimental raindrop size distribution spectra, *Quarterly Journal of the Royal Meteorological Society*, 142, 125–137, <https://doi.org/10.1002/qj.2801>, 2016a.
- Raupach, T. H. and Berne, A.: Small-Scale Variability of the Raindrop Size Distribution and Its Effect on Areal Rainfall Retrieval, *Journal of Hydrometeorology*, 17, 2077–2104, <https://doi.org/10.1175/JHM-D-15-0214.1>, 2016b.
- Raupach, T. H. and Berne, A.: Retrieval of the raindrop size distribution from polarimetric radar data using double-moment normalisation, *Atmospheric Measurement Techniques*, 10, 2573–2594, <https://doi.org/10.5194/amt-10-2573-2017>, 2017.
- Raupach, T. H., Thurai, M., Bringi, V. N., and Berne, A.: Reconstructing the Drizzle Mode of the Raindrop Size Distribution Using Double-Moment Normalization, *Journal of Applied Meteorology and Climatology*, 58, 145–164, <https://doi.org/10.1175/JAMC-D-18-0156.1>, 2019.
- Rixen, C., Høye, T. T., Macek, P., Aerts, R., Alatalo, J. M., Anderson, J. T., Arnold, P. A., Barrio, I. C., Bjerke, J. W., Björkman, M. P., Blok, D., Blume-Werry, G., Boike, J., Bokhorst, S., Carbonegnani, M., Christiansen, C. T., Convey, P., Cooper, E. J., Cornelissen, J. H. C., Coulson, S. J., Dorrepaal, E., Elberling, B., Elmendorf, S. C., Elphinstone, C., Forte, T. G., Frei, E. R., Geange, S. R., Gehrman, F., Gibson, C., Grogan, P., Halbritter, A. H., Harte, J., Henry, G. H., Inouye, D. W., Irwin, R. E., Jespersen, G., Jónsdóttir, I. S., Jung, J. Y., Klings, D. H., Kudo, G., Lämsä, J., Lee, H., Lembrechts, J. J., Lett, S., Lynn, J. S., Mann, H. M., Mastepanov, M., Morse, J., Myers-Smith, I. H., Olofsson, J., Paavola, R., Petraglia, A., Phoenix, G. K., Semenchuk, P., Siewert, M. B., Slatyer, R., Spasojevic, M. J., Suding, K., Sullivan, P., Thompson, K. L., Väisänen, M., Vandvik, V., Venn, S., Walz, J., Way, R., Welker, J. M., Wipf, S., and Zong, S.: Winters are changing: snow effects on Arctic and alpine tundra ecosystems, *Arctic Science*, 8, 572–608, <https://doi.org/10.1139/as-2020-0058>, 2022.
- Rocklin, M.: Dask: Parallel Computation with Blocked algorithms and Task Scheduling, in: *Proc. of the 14th Python in Science Conf.*, pp. 126–132, <https://doi.org/10.25080/Majora-7b98e3ed-013>, 2015.
- Ross, A., Smith, C. D., and Barr, A.: An improved post-processing technique for automatic precipitation gauge time series, *Atmospheric Measurement Techniques*, 13, 2979–2994, <https://doi.org/10.5194/amt-13-2979-2020>, 2020.
- Ryzhkov, A., Pinsky, M., Pokrovsky, A., and Khain, A.: Polarimetric Radar Observation Operator for a Cloud Model with Spectral Microphysics, *Journal of Applied Meteorology and Climatology*, 50, 873–894, <https://doi.org/10.1175/2010JAMC2363.1>, 2011.
- Saha, R., Testik, F. Y., and Testik, M. C.: Assessment of OTT Pluvio2 rain intensity measurements, *Journal of Atmospheric and Oceanic Technology*, 38, 897–908, <https://doi.org/10.1175/JTECH-D-19-0219.1>, 2021.
- Salles, C., Creutin, J.-D., and Sempere-Torres, D.: The Optical Spectropluviometer Revisited, *Journal of Atmospheric and Oceanic Technology*, 15, 1215–1222, [https://doi.org/10.1175/1520-0426\(1998\)015<1215:TOSR>2.0.CO;2](https://doi.org/10.1175/1520-0426(1998)015<1215:TOSR>2.0.CO;2), 1998.
- Saltikoff, E., Haase, G., Delobbe, L., Gaussiat, N., Martet, M., Idziorek, D., Leijnse, H., Novák, P., Lukach, M., and Stephan, K.: OPERA the Radar Project, *Atmosphere*, 10, 320, <https://doi.org/10.3390/atmos10060320>, 2019.



- 1510 Sauvageot, H. and Lacaux, J.-P.: The Shape of Averaged Drop Size Distributions, *Journal of the Atmospheric Sciences*, 52, 1070–1083, [https://doi.org/10.1175/1520-0469\(1995\)052<1070:TSOADS>2.0.CO;2](https://doi.org/10.1175/1520-0469(1995)052<1070:TSOADS>2.0.CO;2), 1995.
- Schweizer, J., Jamieson, J. B., and Schneebeli, M.: Snow avalanche formation, *Reviews of Geophysics*, 41, <https://doi.org/10.1029/2002RG000123>, 2003.
- Schweizer, J., Bartelt, P., and van Herwijnen, A.: Snow avalanches, pp. 377–416, Elsevier, <https://doi.org/10.1016/B978-0-12-817129-5.00001-9>, 2021.
- 1515 Segovia-Cardozo, D. A., Rodríguez-Sinobas, L., Díez-Herrero, A., Zubelzu, S., and Canales-Ide, F.: Understanding the Mechanical Biases of Tipping-Bucket Rain Gauges: A Semi-Analytical Calibration Approach, *Water*, 13, 2285, <https://doi.org/10.3390/w13162285>, 2021.
- Seifert, A. and Beheng, K. D.: A two-moment cloud microphysics parameterization for mixed-phase clouds. Part 1: Model description, *Meteorology and Atmospheric Physics*, 92, 45–66, <https://doi.org/10.1007/s00703-005-0112-4>, 2006.
- 1520 Serio, M. A., Carollo, F. G., and Ferro, V.: Raindrop size distribution and terminal velocity for rainfall erosivity studies. A review, *Journal of Hydrology*, 576, 210–228, <https://doi.org/10.1016/j.jhydrol.2019.06.040>, 2019.
- Sevruk, B.: Evaporation losses from containers of hellmann precipitation gauges, *Hydrological Sciences Bulletin*, 19, 231–236, <https://doi.org/10.1080/02626667409493902>, 1974.
- Shedekar, V. S., King, K. W., Fausey, N. R., Soboyejo, A. B., Harmel, R. D., and Brown, L. C.: Assessment of measurement errors and dynamic calibration methods for three different tipping bucket rain gauges, *Atmospheric Research*, 178–179, 445–458, <https://doi.org/10.1016/j.atmosres.2016.04.016>, 2016.
- 1525 Shi, J., Liu, X., Liu, L., Liu, L., and Wang, P.: An introduction of the Three-Dimensional Precipitation Particle Imager (3D-PPI), *Atmospheric Measurement Techniques*, 18, 2261–2278, <https://doi.org/10.5194/amt-18-2261-2025>, 2025.
- Shin, K., Kim, K., Song, J. J., and Lee, G.: Polarimetric Retrieval of Raindrop Size Distribution: Double-Moment Normalization Approach and Machine Learning Techniques, *Geophysical Research Letters*, 51, <https://doi.org/10.1029/2023GL106057>, 2024.
- 1530 Smith, P. L., Johnson, R. W., and Kliche, D. V.: On Use of the Standard Deviation of the Mass Distribution as a Parameter in Raindrop Size Distribution Functions, *Journal of Applied Meteorology and Climatology*, 58, 787–796, <https://doi.org/10.1175/JAMC-D-18-0086.1>, 2019.
- Stacy, E. W.: A Generalization of the Gamma Distribution, *The Annals of Mathematical Statistics*, 33, 1187–1192, <https://doi.org/10.1214/aoms/1177704481>, 1962.
- 1535 Steinert, J., Tracksdorf, P., and Heizenreder, D.: Hymec: Surface Precipitation Type Estimation at the German Weather Service, *Weather and Forecasting*, 36, 1611–1627, <https://doi.org/10.1175/WAF-D-20-0232.1>, 2021.
- Stevens, B., Farrell, D., Hirsch, L., Jansen, F., Nuijens, L., Serikov, I., Brüggmann, B., Forde, M., Linne, H., Lonitz, K., and Prospero, J. M.: The Barbados Cloud Observatory: Anchoring Investigations of Clouds and Circulation on the Edge of the ITCZ, *Bulletin of the American Meteorological Society*, 97, 787–801, <https://doi.org/10.1175/BAMS-D-14-00247.1>, 2016.
- 1540 Strangeways, I.: A history of rain gauges, *Weather*, 65, 133–138, <https://doi.org/10.1002/wea.548>, 2010.
- Szakáll, M., Mitra, S. K., Diehl, K., and Borrmann, S.: Shapes and oscillations of falling raindrops — A review, *Atmospheric Research*, 97, 416–425, <https://doi.org/10.1016/j.atmosres.2010.03.024>, 2010.
- Tapiador, F. J., Checa, R., and de Castro, M.: An experiment to measure the spatial variability of rain drop size distribution using sixteen laser disdrometers, *Geophysical Research Letters*, 37, <https://doi.org/10.1029/2010GL044120>, 2010.
- 1545



- Teng, S., Hu, H., Liu, C., Hu, F., Wang, Z., and Yin, Y.: Numerical simulation of raindrop scattering for C-band dual-polarization Doppler weather radar parameters, *Journal of Quantitative Spectroscopy and Radiative Transfer*, 213, 133–142, <https://doi.org/10.1016/j.jqsrt.2018.04.004>, 2018.
- Testik, F. Y. and Bolek, A.: Wind and Turbulence Effects on Raindrop Fall Speed, *Journal of the Atmospheric Sciences*, 80, 1065–1086, <https://doi.org/10.1175/JAS-D-22-0137.1>, 2023.
- 1550 Testik, F. Y. and Pei, B.: Wind Effects on the Shape of Raindrop Size Distribution, *Journal of Hydrometeorology*, 18, 1285–1303, <https://doi.org/10.1175/JHM-D-16-0211.1>, 2017.
- Testik, F. Y. and Rahman, M. K.: High-speed optical disdrometer for rainfall microphysical observations, *Journal of Atmospheric and Oceanic Technology*, 33, 231–243, <https://doi.org/10.1175/JTECH-D-15-0098.1>, 2016.
- 1555 Testud, J., Oury, S., Black, R. A., Amayenc, P., and Dou, X.: The Concept of “Normalized” Distribution to Describe Raindrop Spectra: A Tool for Cloud Physics and Cloud Remote Sensing, *Journal of Applied Meteorology*, 40, 1118–1140, [https://doi.org/10.1175/1520-0450\(2001\)040<1118:TCOND>2.0.CO;2](https://doi.org/10.1175/1520-0450(2001)040<1118:TCOND>2.0.CO;2), 2001.
- Thurai, M. and Bringi, V. N.: Drop Axis Ratios from a 2D Video Disdrometer, *Journal of Atmospheric and Oceanic Technology*, 22, 966–978, <https://doi.org/10.1175/JTECH1767.1>, 2005.
- 1560 Thurai, M., Huang, G. J., Bringi, V. N., Randeu, W. L., and Schönhuber, M.: Drop Shapes, Model Comparisons, and Calculations of Polarimetric Radar Parameters in Rain, *Journal of Atmospheric and Oceanic Technology*, 24, 1019–1032, <https://doi.org/10.1175/JTECH2051.1>, 2007.
- Thurai, M., Hudak, D., and Bringi, V. N.: On the Possible Use of Copolar Correlation Coefficient for Improving the Drop Size Distribution Estimates at C Band, *Journal of Atmospheric and Oceanic Technology*, 25, 1873–1880, <https://doi.org/10.1175/2008JTECHA1077.1>,
- 1565 2008.
- Tilg, A.-M., Vejen, F., Hasager, C. B., and Nielsen, M.: Rainfall Kinetic Energy in Denmark: Relationship with Drop Size, Wind Speed, and Rain Rate, *Journal of Hydrometeorology*, 21, 1621–1637, <https://doi.org/10.1175/JHM-D-19-0251.1>, 2020.
- Tokay, A. and Bashor, P. G.: An Experimental Study of Small-Scale Variability of Raindrop Size Distribution, *Journal of Applied Meteorology and Climatology*, 49, 2348–2365, <https://doi.org/10.1175/2010JAMC2269.1>, 2010.
- 1570 Tokay, A., Kruger, A., and Krajewski, W. F.: Comparison of Drop Size Distribution Measurements by Impact and Optical Disdrometers, *Journal of Applied Meteorology*, 40, 2083–2097, [https://doi.org/10.1175/1520-0450\(2001\)040<2083:CODSDM>2.0.CO;2](https://doi.org/10.1175/1520-0450(2001)040<2083:CODSDM>2.0.CO;2), 2001.
- Tokay, A., Wolff, K. R., Bashor, P., and Dursun, O. K.: On the Measurement Errors of the Joss-Waldvogel Disdrometer, in: *Preprints, 31st Int. Conf. on Radar Meteorology*, Seattle, WA, Amer. Meteor. Soc., 437–440., ISBN 30,97231,676, 2003.
- Tokay, A., Bashor, P. G., and Wolff, K. R.: Error Characteristics of Rainfall Measurements by Collocated Joss–Waldvogel Disdrometers,
- 1575 *Journal of Atmospheric and Oceanic Technology*, 22, 513–527, <https://doi.org/10.1175/JTECH1734.1>, 2005.
- Tokay, A., D’Adderio, L. P., Wolff, D. B., and Petersen, W. A.: A Field Study of Pixel-Scale Variability of Raindrop Size Distribution in the Mid-Atlantic Region, *Journal of Hydrometeorology*, 17, 1855–1868, <https://doi.org/10.1175/JHM-D-15-0159.1>, 2016.
- Tokay, A., D’Adderio, L. P., Porcù, F., Wolff, D. B., and Petersen, W. A.: A Field Study of Footprint-Scale Variability of Raindrop Size Distribution, *Journal of Hydrometeorology*, 18, 3165–3179, <https://doi.org/10.1175/JHM-D-17-0003.1>, 2017.
- 1580 Trujillo, E., Molotch, N. P., Goulden, M. L., Kelly, A. E., and Bales, R. C.: Elevation-dependent influence of snow accumulation on forest greening, *Nature Geoscience*, 5, 705–709, <https://doi.org/10.1038/ngeo1571>, 2012.
- Trömel, S., Kumjian, M. R., Ryzhkov, A. V., Simmer, C., and Diederich, M.: Backscatter Differential Phase—Estimation and Variability, *Journal of Applied Meteorology and Climatology*, 52, 2529–2548, <https://doi.org/10.1175/JAMC-D-13-0124.1>, 2013.



- Tsikoudi, I., Battaglia, A., Unal, C., and Marinou, E.: Simulations of spectral polarimetric variables measured in rain at W-band, *Atmospheric Measurement Techniques*, 18, 4857–4870, <https://doi.org/10.5194/amt-18-4857-2025>, 2025.
- 1585 Turner, D. D., Kneifel, S., and Cadeddu, M. P.: An Improved Liquid Water Absorption Model at Microwave Frequencies for Supercooled Liquid Water Clouds, *Journal of Atmospheric and Oceanic Technology*, 33, 33–44, <https://doi.org/10.1175/JTECH-D-15-0074.1>, 2016.
- Uijlenhoet, R., Steiner, M., and Smith, J. A.: Influence of disdrometer deadtime correction on self-consistent analytical parameterizations for raindrop size distributions, in: *Proceedings of the 2nd European Conference on Radar Meteorology (ERAD 2002)*, pp. 104–112, 2002.
- 1590 Uijlenhoet, R., Steiner, M., and Smith, J. A.: Variability of Raindrop Size Distributions in a Squall Line and Implications for Radar Rainfall Estimation, *Journal of Hydrometeorology*, 4, 43–61, [https://doi.org/10.1175/1525-7541\(2003\)004<0043:VORSDI>2.0.CO;2](https://doi.org/10.1175/1525-7541(2003)004<0043:VORSDI>2.0.CO;2), 2003.
- Uijlenhoet, R., Cohard, J.-M., and Gosset, M.: Path-Average Rainfall Estimation from Optical Extinction Measurements Using a Large-Aperture Scintillometer, *Journal of Hydrometeorology*, 12, 955–972, <https://doi.org/10.1175/2011JHM1350.1>, 2011.
- Uijlenhoet, R., Overeem, A., and Leijnse, H.: Opportunistic remote sensing of rainfall using microwave links from cellular communication networks, *WIREs Water*, 5, <https://doi.org/10.1002/wat2.1289>, 2018.
- 1595 Ulbrich, C. W.: Natural Variations in the Analytical Form of the Raindrop Size Distribution, *Journal of Climate and Applied Meteorology*, 22, 1764–1775, [https://doi.org/10.1175/1520-0450\(1983\)022<1764:NVITAF>2.0.CO;2](https://doi.org/10.1175/1520-0450(1983)022<1764:NVITAF>2.0.CO;2), 1983.
- Ulbrich, C. W. and Atlas, D.: Extinction of Visible and Infrared Radiation in Rain: Comparison of Theory and Experiment, *Journal of Atmospheric and Oceanic Technology*, 2, 331–339, [https://doi.org/10.1175/1520-0426\(1985\)002<0331:EOVAIR>2.0.CO;2](https://doi.org/10.1175/1520-0426(1985)002<0331:EOVAIR>2.0.CO;2), 1985.
- 1600 Unidata: Network Common Data Form (NetCDF), 2025.
- Uplinger, C. W.: A new formula for raindrop terminal velocity, *Preprints, 20th Conf. on Radar Meteorology*, Boston, MA, Amer. Meteor. Soc., pp. 389–391, 1981.
- van Dijk, A., Bruijnzeel, L., and Rosewell, C.: Rainfall intensity–kinetic energy relationships: a critical literature appraisal, *Journal of Hydrology*, 261, 1–23, [https://doi.org/10.1016/S0022-1694\(02\)00020-3](https://doi.org/10.1016/S0022-1694(02)00020-3), 2002.
- 1605 van Leth, T. C., Leijnse, H., Overeem, A., and Uijlenhoet, R.: Estimating raindrop size distributions using microwave link measurements: potential and limitations, *Atmospheric Measurement Techniques*, 13, 1797–1815, <https://doi.org/10.5194/amt-13-1797-2020>, 2020.
- Vázquez-Martín, S., Kuhn, T., and Eliasson, S.: Shape dependence of snow crystal fall speed, *Atmospheric Chemistry and Physics*, 21, 7545–7565, <https://doi.org/10.5194/acp-21-7545-2021>, 2021a.
- Vázquez-Martín, S., Kuhn, T., and Eliasson, S.: Mass of different snow crystal shapes derived from fall speed measurements, *Atmospheric Chemistry and Physics*, 21, 18 669–18 688, <https://doi.org/10.5194/acp-21-18669-2021>, 2021b.
- 1610 Williams, C. R., Bringi, V. N., Carey, L. D., Chandrasekar, V., Gatlin, P. N., Haddad, Z. S., Meneghini, R., Munchak, S. J., Nesbitt, S. W., Petersen, W. A., Tanelli, S., Tokay, A., Wilson, A., and Wolff, D. B.: Describing the Shape of Raindrop Size Distributions Using Uncorrelated Raindrop Mass Spectrum Parameters, *Journal of Applied Meteorology and Climatology*, 53, 1282–1296, <https://doi.org/10.1175/JAMC-D-13-076.1>, 2014.
- 1615 Willis, P. T.: Functional Fits to Some Observed Drop Size Distributions and Parameterization of Rain, *Journal of the Atmospheric Sciences*, 41, 1648–1661, [https://doi.org/10.1175/1520-0469\(1984\)041<1648:FFTSOD>2.0.CO;2](https://doi.org/10.1175/1520-0469(1984)041<1648:FFTSOD>2.0.CO;2), 1984.
- WMO: Guide to meteorological instruments and methods of observation. Volume I – Measurement of Meteorological Variables, World Meteorological Organization, ISBN 9789263100085, 2024.
- Wolfensberger, D. and Berne, A.: From model to radar variables: a new forward polarimetric radar operator for COSMO, *Atmospheric Measurement Techniques*, 11, 3883–3916, <https://doi.org/10.5194/amt-11-3883-2018>, 2018.
- 1620



- Yang, Q., Dai, Q., Han, D., Chen, Y., and Zhang, S.: Sensitivity analysis of raindrop size distribution parameterizations in WRF rainfall simulation, *Atmospheric Research*, 228, 1–13, <https://doi.org/10.1016/j.atmosres.2019.05.019>, 2019.
- Zeng, Y., Blahak, U., and Jerger, D.: An efficient modular volume-scanning radar forward operator for NWP models: description and coupling to the COSMO model, *Quarterly Journal of the Royal Meteorological Society*, 142, 3234–3256, <https://doi.org/10.1002/qj.2904>, 2016.
- 1625 Zhang, G.: Comments on “Describing the Shape of Raindrop Size Distributions Using Uncorrelated Raindrop Mass Spectrum Parameters”, *Journal of Applied Meteorology and Climatology*, 54, 1970–1976, <https://doi.org/10.1175/JAMC-D-14-0210.1>, 2015.
- Zhang, G., Vivekanandan, J., and Brandes, E.: A method for estimating rain rate and drop size distribution from polarimetric radar measurements, *IEEE Transactions on Geoscience and Remote Sensing*, 39, 830–841, <https://doi.org/10.1109/36.917906>, 2001.
- Zhang, G., Vivekanandan, J., Brandes, E. A., Meneghini, R., and Kozu, T.: The Shape–Slope Relation in Observed Gamma Rain-
1630 drop Size Distributions: Statistical Error or Useful Information?, *Journal of Atmospheric and Oceanic Technology*, 20, 1106–1119, [https://doi.org/10.1175/1520-0426\(2003\)020<1106:TSRIOG>2.0.CO;2](https://doi.org/10.1175/1520-0426(2003)020<1106:TSRIOG>2.0.CO;2), 2003.
- Zhang, P., Liu, X., and Pu, K.: Precipitation Monitoring Using Commercial Microwave Links: Current Status, Challenges and Perspectives, *Remote Sensing*, 15, 4821, <https://doi.org/10.3390/rs15194821>, 2023.
- Zheng, H., Zhang, Y., Li, H., Wu, Z., Xie, Y., and Zhang, L.: Raindrop Deformation in Turbulence, *Geophysical Research Letters*, 51,
1635 <https://doi.org/10.1029/2024GL108627>, 2024.